Russian Chemical Reviews **83** (11) 1027 – 1061 (2014) © 2014 Russian Academy of Sciences and Turpion Ltd

DOI 10.1070/RCR4407

The structure and properties of high-entropy alloys and nitride coatings based on them

A D Pogrebnjak,[a] A A Bagdasaryan,[a] I V Yakushchenko,[a] V M Beresnev [b]

[a] *Sumy State University*
ul. Rimskogo-Korsakova 2, 40007 Sumy, Ukraine
[b] *V N Karazin Kharkiv National University*
pl. Svobody 4, 61022 Kharkiv, Ukraine

The results of studies on the regularities of structure formation and properties of high-entropy alloys prepared by different methods are analyzed and generalized. Specific features of the synthesis of nitride coatings based on multicomponent alloys are considered. Main physicomechanical properties of the coatings of different elemental composition deposited in different manner were compared.
The bibliography includes 229 references.

Contents

I. Introduction 1027
II. Theoretical investigations of high-entropy alloys 1028
III. Methods of preparation of high-entropy alloys and coatings based on them 1038
IV. Properties of high-entropy alloys 1043
V. Properties of nitride coatings based on high-entropy alloys 1049
VI. Influence of deposition conditions on the microstructure and properties of nitride coatings based on high-entropy alloys 1054
VII. Applications of high-entropy alloys and nitride coatings based on them 1055
VIII. Conclusion 1056

I. Introduction

Progress in theoretical studies on novel materials and the development of relevant technologies made it possible to prepare metallic alloys containing more than three principal elements. In the last decade, a novel class of metallic compounds called high-entropy alloys was developed.[1, 2] These systems contain at least five principal metals with a content of 5 at.% to 35 at.% each. The main feature of high-entropy alloys is the possibility to form thermodynamically stable, high-strength, single-phase substitutional solid solutions with mainly fcc or bcc lattices.[3] Stabilization of the solid solutions and prevention of the formation of intermetallic phases during crystallization are ensured by high entropy of mixing of the components ($S_{mix} > 1.61R$, where $R = 8.314$ J mol^{-1} K^{-1} is the universal gas constant) in the initial (charge mixture) and molten states. The maximum entropy is attained at equimolar ratio of the constituent elements. Based on the Boltzmann hypothesis, the larger the number of elements used to prepare a solid solution the higher the configurational entropy (ΔS_{conf}). An increase in ΔS_{conf} of the molten and solidified alloy favours the formation of a simple structure in the form of a single-phase disordered substitutional solid solution (one crystal lattice), which is thermodynamically favourable compared to the formation of a multiphase solid solution. Therefore, a tendency to formation of ordered structures becomes much less pronounced owing to minimization of the Gibbs free energy; segregation of elements in the course of solidification also becomes less probable.[4]

Studies on high-entropy alloys revealed the possibility of formation of nanoscale structures and even amorphous phases [3, 5] owing to significant lattice distortion due to the difference between the atomic radii of the substitutional elements. In this case, the diffusion rate decreases and, consequently, so does the growth rate of crystallites.

A D Pogrebnjak Doctor of Physical and Mathematical Sciences, Professor, Head of Department of Nanoelectronics at the SSU.
Telephone: (38-0686) 52 96 47, e-mail: alexp@i.ua
A A Bagdasaryan Post-graduate Student of the same Department.
Telephone: (38-0994) 02 54 93, e-mail: artemsumdu@ukr.net
I V Yakushchenko Post-graduate Student of the same Department.
Telephone: (38-0502) 20 71 14, e-mail: kosist@mail.ru
V M Beresnev Doctor of Technical Sciences, Professor, Head of Department of Materials for Reactor Building at the KNU.
Telephone: (38-228) 26 12 81 (extra 261),
e-mail: beresnev-scpt@yandex.ua
Current research interests of the authors: materials science, surface modification, nanocomposite coatings.

Received 16 May 2013
Uspekhi Khimii **83** (11) 1027 – 1061 (2014); translated by A M Raevskiy

Progress in technology involves the design of novel materials with necessary physicochemical and high mechanical properties or a combination of properties. Recently, there has been increasing interest in nitrides, *i.e.*, nitrogen-containing compounds of metals and nonmetals. Transition metal nitrides exhibit high hardness, oxidative stability and wear resistance and are therefore mainly used as protective materials.[6–8] An example of a widely used nitride is provided by TiN which is rapidly oxidized above 500 °C, thus being of limited use. In the last decade, coatings based on TiN doped with Al, Cr–$Ti_{1-x}Al_xN$ and $Ti_{1-x}Cr_xN$, *i.e.*, systems with improved operating properties, namely, higher oxidative stability and wear resistance have been widely used.[9] Clearly, more versatile properties of protective coatings can be achieved by increasing the number of constituent elements (transition metals) in the nitride systems.[10–17] Both research and practical interests in the novel nitride coatings based on multicomponent alloys are due to their excellent physicochemical properties originating from the influence of strain hardening of solid solutions, lattice distortion and even nanocomposite structure.[18–23]

Variability of the elemental composition of high-entropy alloys and nitrides based on them gives rise to a number of useful properties, *e.g.*, high-temperature strength, superparamagnetism, wear resistance, corrosion resistance, high hardness, plasticity, *etc.*[24–27] This makes it possible to significantly extend the field of application of the compounds in question, namely, they can be used for fabrication of cutting tools, dies, machinery parts, targets for magnetron sputtering, diffusion barriers, *etc.*[3, 28, 29]

A number of recent reviews on the most interesting properties of high-entropy alloys are available.[1, 3, 30–34] Most of them, written by researchers from abroad, concern the thermodynamics of high-entropy alloys, the results of structure simulation and new methods for preparation of multicomponent alloys. A particular position is occupied by the review by Zhang *et al.*,[34] who correctly described the physical principles of the preparation of high-entropy alloys, discussed their microstructure and made a forecast of possible applications. However, Zhang *et al.* did not analyze some published results that could help in describing the physical picture of the processes in hand, probably, because these results did not fit into the context of the review. In addition, it is difficult to understand what is the key difference between high-entropy alloys and multicomponent alloys. Unfortunately, Zhang *et al.*[34] very briefly analyzed nitride and carbide coatings based on multicomponent high-entropy alloys and left the advantages of these systems out of consideration.

In this review, we analyzed the studies that were not included in the above publication. The emphasis is placed on the physical properties, microstructure and possible applications of the nitride coatings based on high-entropy alloys.

An interesting study[35] of physical processes in the multicomponent cast and quenched alloys (cooling rate 10 and 10^6 K s^{-1}, respectively) is methodologically well substantiated. Also, a series of interesting studies reported by Ukrainian and Russian researchers[35–47] were devoted to investigation of the properties of high-entropy alloys; however, the number of such studies is much smaller than the amount of publications reported by researchers from other countries.[48–184]

II. Theoretical investigations of high-entropy alloys

As mentioned above, high-entropy alloys are a new class of metallic compounds containing at least five principal elements whose concentrations vary from 5 at.% to 35 at.%. A feature of these systems consists in preferred formation of disordered solid solutions stabilized by high entropy of mixing. The distinctive features of high-entropy alloys include:[32]

— high entropy of mixing,
— lattice distortion,
— sluggish diffusion,
— so-called cocktail effect.

They are briefly outlined below.

II.1. High entropy of mixing

High-entropy alloys form stable, single-phase substitutional solid solutions. This contradicts the Gibbs phase rule, according to which the number of phases in a given alloy at constant pressure and temperature is

$$P = C + 1 - F$$

where C is the number of constituent elements and F is the maximum number of thermodynamic degrees of freedom in the system. In the case of a five-element system, one may expect a total of six equilibrium phases. However, high-entropy alloys mainly form disordered solid solutions and ordered compounds (intermetallics).

Stabilization of the solid solution and prevention of the formation of intermetallic phases in the course of crystallization is provided by high entropy of mixing in the initial and molten states. Following Boltzmann's hypothesis, the configurational entropy of mixing is given by:

$$\Delta S_{\text{conf}} = -R\left(\frac{1}{n}\ln\frac{1}{n} + \frac{1}{n}\ln\frac{1}{n} + \ldots + \frac{1}{n}\ln\frac{1}{n}\right) = \quad (1)$$

$$= -R\ln\frac{1}{n} = R\ln n$$

where n is the number of elements. The maximum entropy value is achieved at equimolar ratio of the constituent elements.

Thus, the larger the number of elements the higher the configurational entropy of a solid solution being formed (Fig. 1). In turn, intermetallics represent ordered phases and are therefore characterized by low configurational entropy which equals zero for stoichiometric compositions.

II.2. Lattice distortion

A fundamental difference between the design of high-entropy alloys and traditional approaches to preparation of alloys, which involve a solvent and a solute, consists in the formation of disordered solid solutions where atoms of the constituent elements have equal probability to occupy lattice sites. Combining constituent elements (and, consequently, different atomic radii) may lead to severe lattice distortion (Fig. 2), which may significantly influence the structure and properties of the alloys.

A study[49] of the electrical, magnetic and thermophysical properties of the multicomponent high-entropy alloy $Al_xCoCrFeNi$ revealed a considerable increase in its resis-

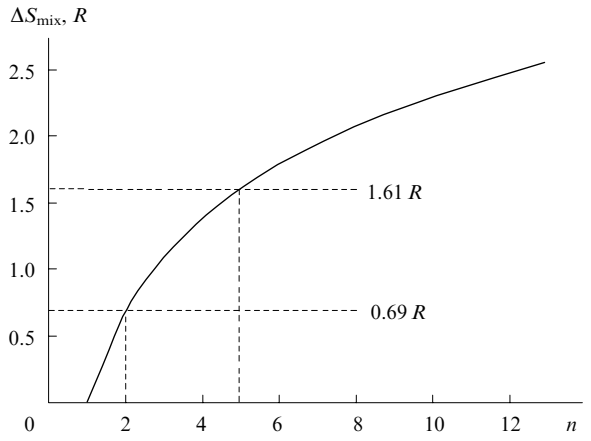


Figure 1. Entropy of mixing of an equimolar alloy plotted *vs.* number of constituent elements.[2]

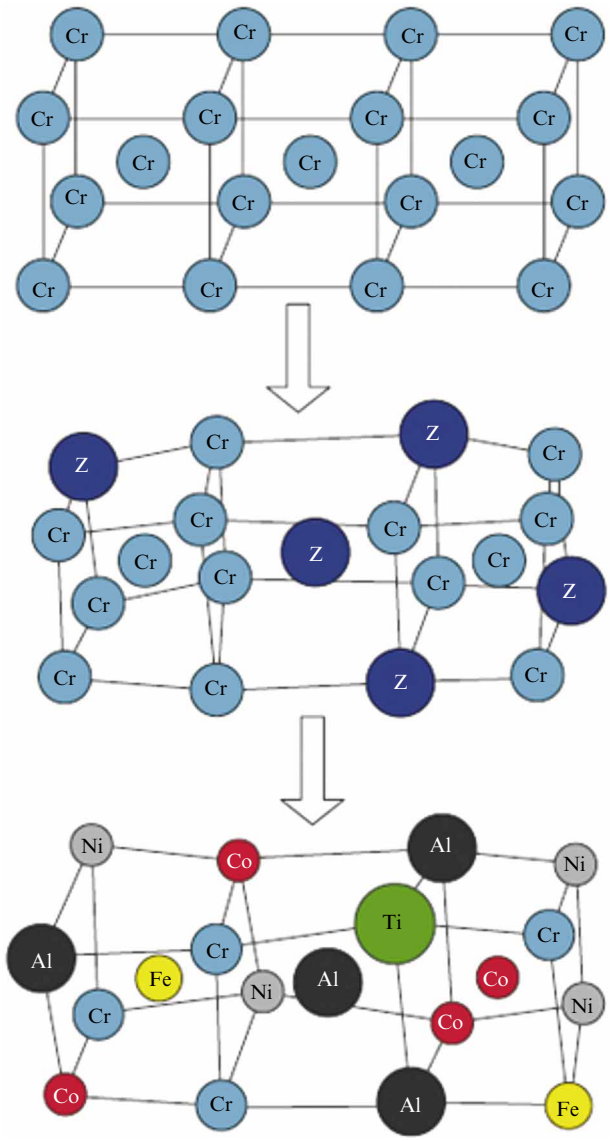


Figure 2. Formation of bcc lattice of the multicomponent alloy $AlCoCrFeNiTi_{0.5}$: a schematic illustration.[48]
'Z' denotes vacancies.

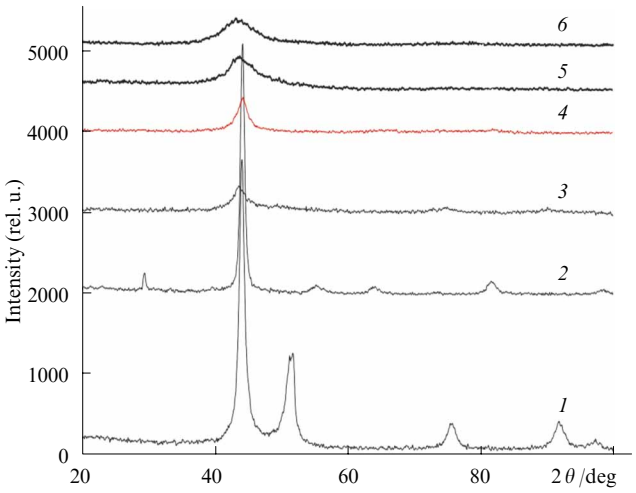


Figure 3. X-ray diffraction patterns of alloys based on $Cu_{0.5}Ni$.[1]
Alloy: $Cu_{0.5}Ni$, fcc phase (*1*); $Cu_{0.5}NiAl$, ordered fcc phase (*2*); $Cu_{0.5}NiAlCo$, fcc phase (*3*); $Cu_{0.5}NiAlCoCr$, bcc phase (*4*); amorphous alloy $Cu_{0.5}NiAlCoFe$ (*5*) and amorphous alloy $Cu_{0.5}NiAlCoFeTi$ (*6*).

tivity with increasing the concentration of aluminium. It was shown that electron transfer in the system under study is governed by defects; high-entropy alloys occupy an intermediate position between amorphous and crystalline alloys with respect to the density of defects. Thus, the electrical and thermal conductivity decreases owing to electron and phonon scattering.

Increasing the number of constituent elements can be accompanied by pronounced structural changes. For instance, well-defined changes from crystalline to amorphous state of alloys based on $Cu_{0.5}Ni$ (Fig. 3) were revealed.[1] Note that an increase in the number of constituent elements leads to broadening of diffraction peaks and a decrease of their intensities. This phenomenon was considered in more detail elsewhere.[50]

Raising the temperature causes the amplitudes of atomic vibrations (so-called thermal effect) to increase and, consequently, the intensities of reflected X-rays to decrease.[185–187] A similar situation is observed in the case of lattice distortion that influences the mutual arrangement of atomic planes (Fig. 4). In this case, amplitudes of diffraction peaks decrease much faster with increasing the number of constituent elements compared to the thermal effect. Lattice distortion caused by different types of the constituent elements leads to a considerable decrease in the degree of crystallinity and X-ray scattering and, eventually, to abnormal decrease in the peak amplitudes.

II.3. Sluggish diffusion

A distinctive feature of high-entropy alloys is equal probability for each atom of a constituent element to occupy a lattice site (see above). Owing to the presence of different types of atoms the potential energy varies from one lattice site to another. Fluctuations of the potential energy of atom–atom bonds significantly influence the diffusion kinetics and the activation energy of diffusion. The first attempt to explain the mechanism of diffusion in the high-entropy system Co–Cr–Fe–Mn–Ni was reported by Yeh and co-workers,[51] who determined the order of ele-

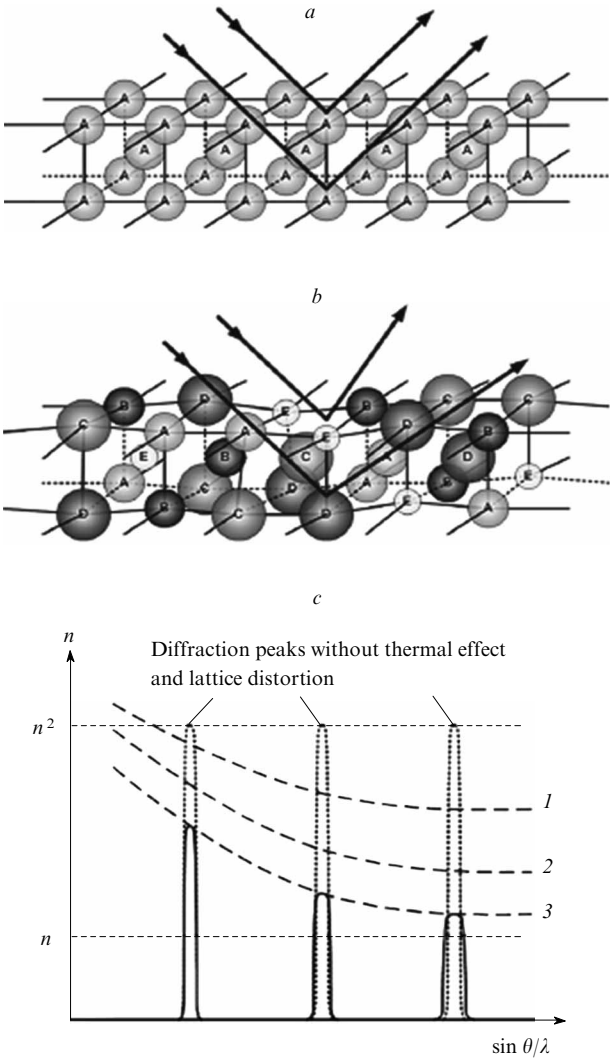


Figure 4. Schematic illustration of lattice distortion on Bragg X-ray diffraction.[50]
(*a*) Perfect lattice; (*b*) distorted lattice with randomly distributed atoms in the lattice sites; (*c*) influence of lattice distortion and thermal effect on the intensity of diffraction peaks: thermal effect (*1*), lattice distortion (*2*) and combined effect (*3*).

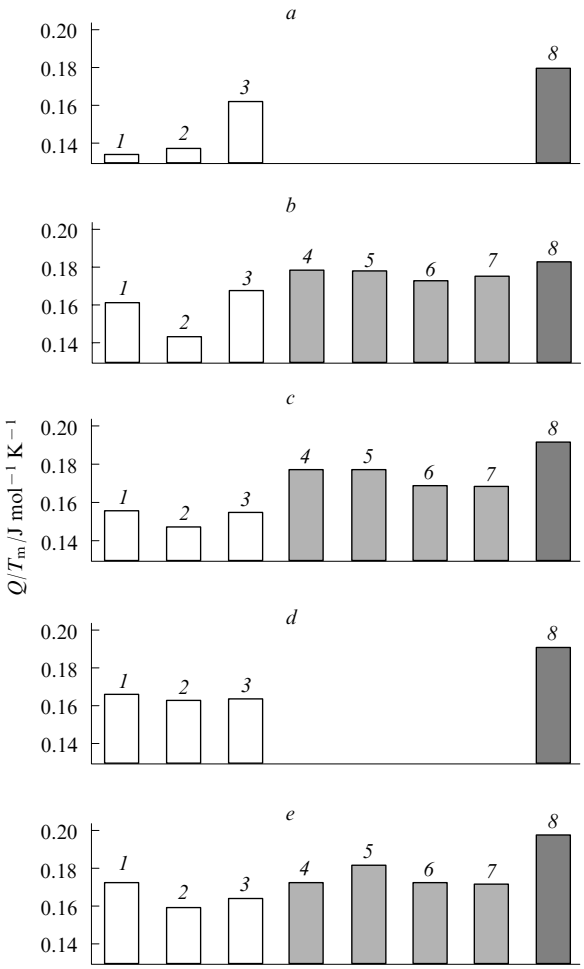


Figure 5. Normalized activation energy of diffusion (Q/T_m) for manganese (*a*), chromium (*b*), iron (*c*), cobalt (*d*) and nickel (*e*) in different matrices.[51]
Matrix: Fe (*1*), Co (*2*), Ni (*3*), Fe – 15Cr – 20Ni (*4*), Fe – 15Cr – 20Ni-Si (*5*), Fe – 15Cr – 45Ni (*6*), Fe – 22Cr – 20Ni (*7*) and Co – Cr – Fe – Mn – Ni (*8*).

ments with respect to the decrease in their diffusion coefficients:

Mn > Cr > Fe > Co > Ni

The results of calculations of the activation energy of diffusion for elements in different matrices are presented in Fig. 5. As can be seen, the normalized activation energies of diffusion of the elements in different matrices are much higher than for pure metals. This is a clear indication of sluggish diffusion in the high-entropy systems. Atoms tend to occupy positions with a minimum free energy. Therefore, the larger the changes in potential energy leading to the higher potential barrier and activation energy of diffusion the more probable the trapping of atoms and, as a consequence, the lower the diffusion coefficients.

The diffusion coefficients of pure metals, stainless steel and high-entropy alloys vary as follows:[52]

high-entropyalloys < stainlesssteel < puremetal

Low diffusion coefficients of atoms in multicomponent systems are responsible for slow grain growth,[53] high-temperature strength[54, 55] and the formation of nanostructures and nanoprecipitates.[3, 5, 56, 57]

II.4. The cocktail effect

It should be noted that the properties of multicomponent alloys originate from those of both the constituent elements and the phases being formed. Usually, high-entropy alloys form single-phase substitutional solid solutions. The formation of other ordered and disordered phases depends on the composition, method of preparation and treatment of the alloy.[5, 58] Thus, both the atoms of particular elements and phases being formed contribute to the properties of high-entropy alloys (so-called cocktail effect). Examples given below illustrate the ability of high-entropy alloys to acquire (improve) various properties.

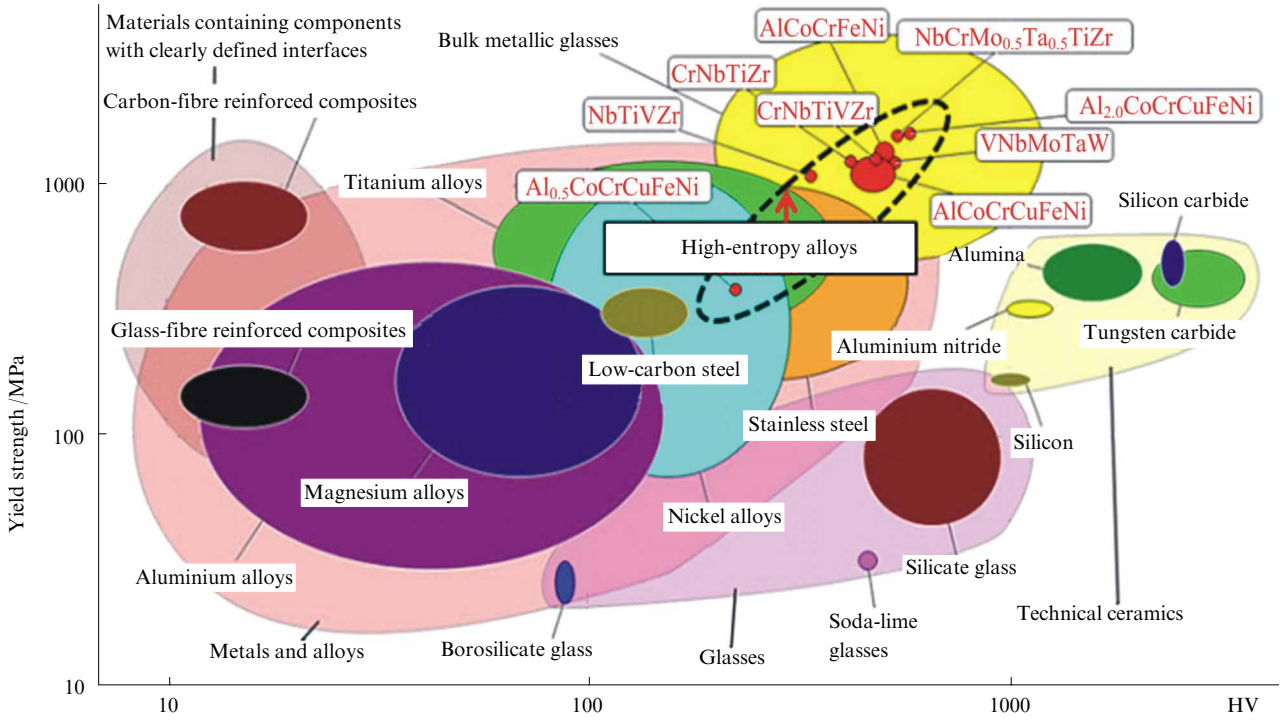


Figure 6. Correlations between the yield strength and Vickers hardness for composites, ceramics, glasses, metallic alloys and high-entropy alloys.[59]

Correlations between the yield strength and Vickers hardness as well as the yield strength and ductility for different types of structural materials are shown in Figs 6 and 7. As can be seen, the strength of high-entropy alloys is higher than those of many metallic alloys. This suggests that multicomponent systems possess the best combinations of the strength and ductility among metallic alloys.

Electrical and magnetic properties of high-entropy alloys were studied in detail.[30 49, 60, 61] In particular, the high-entropy system $FeCoNi(AlSi)_x$ is a soft magnetic

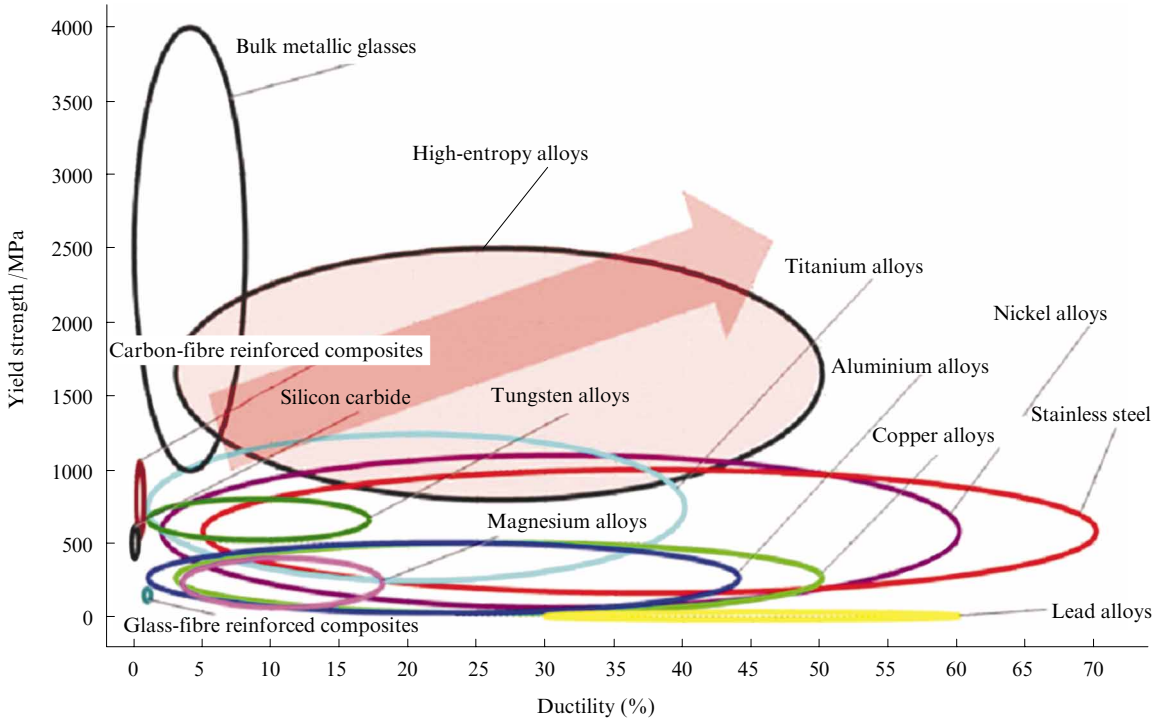


Figure 7. Correlations between the yield strength and ductility (tensile and compressive deformation at room temperature) for composites, ceramics, glasses, metallic alloys and high-entropy alloys.[59]

material with optimum combination of electrical, magnetic and mechanical properties [saturation magnetization is 1.15 T, coercive force (H_c) is 1.400 A m^{-1}, electrical resistivity is 69.5 μΩ cm^{-1}, yield strength is 320 MPa, strain without fracture is 50%].[60]

The electrochemical properties of high-entropy alloys $Cu_{0.5}NiAlCoCrFeSi$ and $Al_xCoCrFeNi$ were studied.[62, 63] Very high corrosion resistance of AlCrFeCuCo was revealed.[64]

II.5. Thermodynamics of high-entropy alloys

Entropy is a function of the state of a system and determines the quality of energy:

$$dS = \frac{dQ}{T}$$

where dQ is the amount of energy absorbed by the system in reversible isothermal process and T is absolute temperature.

According to Boltzmann, a macroscopic system can be described through microscopic states by the following expression:

$$S = k \ln W$$

where k is the Boltzmann constant (1.38×10^{-23} J K^{-1}) and W is the number of equiprobable microscopic states (thermodynamic probability) through which the macroscopic state can be realized.

In thermodynamics, the formation of solid solutions is analyzed from the standpoint of minimum Gibbs free energy [188]

$$G_{l-s} = H_{mix} - TS_{mix}$$

where G_{l-s} is the free energy difference between the liquid alloy and the solidified phase and H_{mix} and S_{mix} are the enthalpy and entropy of mixing, respectively. If the H_{mix} and S_{mix} values are known, one can estimate the Gibbs free energy. If, among all possible phases, the solid solution phase has a minimum Gibbs free energy, the formation of solid solution is most probable.

The configurational entropy of mixing of a disordered solution (assuming no short-range order) is given by

$$\Delta S_{mix} = -R \sum_{i=1}^{n} c_i \ln c_i .$$

This expression is transformed to Eqn (1) in the case of equal molar concentrations (c_i) of all elements.

Thus, the entropy of mixing logarithmically increases with increasing the number of elements (see Fig. 1). Consequently, the free energy decreases and, eventually, the solid solution is stabilized on subsequent heat treatment.[3] Configurational entropy is directly related to the number of types of atomic arrangement in the same lattice sites (the larger this number the higher the entropy). The configurational entropy of mixing makes the largest contribution to the total entropy, but the vibrational, magnetic and electronic contributions should not be ignored. In particular, the vibrational entropy is higher than configurational entropy at moderate temperatures; however, if we consider a phase transition, ΔS_{conf} significantly changes compared to the configurational entropy.[188, 189]

The standard enthalpy of mixing is calculated according to Miedema [190, 191]

$$\Delta H_{mix} = \sum_{i=1, i \neq j}^{n} \Omega_{ij} c_i c_j$$

where $\Omega_{ij} = 4 \Delta_{mix}^{AB}$ is the parameter of the interaction between the ith and jth elements in the solution (Δ_{mix}^{AB} is the enthalpy of mixing of a binary liquid equiatomic alloy AB).[191]

An increase in the configurational entropy of mixing is determined by the probability of formation of a single-phase solid solution by high-entropy alloys.[3] However, a study [65] of the structure of the high-entropy alloy CoCrCuFeNiTi revealed the presence of an fcc phase, Laves phases and even amorphous phases. Three phases were found [66] in the alloy AlCoCrCuNiTi characterized by rather high entropy of mixing. Thus, only high-entropy alloys of particular chemical compositions can form disordered solid solutions,[67, 68] whereas other high-entropy alloys can form solid solutions, be in amorphous state or contain intermetallics.[30, 48, 69] It follows that the entropy of mixing not always dominates and thus ensures the formation of a single-phase structure and moreover influences the microstructure. In this connection, the following questions arise:

— what are the conditions for formation of a solid solution (or amorphous phase) provided a high entropy of mixing?

— is the entropy of mixing a sufficient criterion for the formation of a single-phase solid solution?

— can the Gibbs free energy deviate from its minimum value without subsequent decomposition of the solid solution?

From this standpoint, we will consider publications that are first of all related to the determination of factors responsible for the formation of disordered solid solutions and investigations of processes of atomic arrangement in the lattice sites.

A study [70] of the structure of two high-entropy alloys, AlCoCrCuFe and NiCoCrCuFe, showed that the configurational entropy does not solely govern phase formation. Selected data on the structures of the alloys are presented in Table 1.

As can be seen, all alloys, except NiCoFe, contains at least two phases. It is believed that the formation of copper-rich phases is due to positive enthalpy at a large number of elements (Co, Cr and Fe). Chromium-containing alloys form a σ-phase that can be identified as CoCr or FeCr. An analysis of the entropy of mixing values for all alloys revealed the lowest configurational entropy for NiCoFe, which forms a single-phase solid solution that remains stable even after sintering at 900 °C. Based on the results obtained, it was shown that the entropy of mixing is a

Table 1. Phase evolution in high-entropy alloys after mechanical alloying and sintering at 900 °C.[70]

Alloy	Structure	
	after mechanical alloying	after sintering at 900 °C
AlCoCrCuFe	bcc and copper-rich fcc	ordered bcc (B2), copper-rich fcc, σ-phase
NiCoCrCuFe	fcc and bcc (minor)	two fcc phases, σ-phase
NiCoCrFe	the same	fcc, σ-phase
NiCoCuFe	fcc	two fcc phases
NiCoFe	fcc	fcc

necessary but not sufficient criterion for the formation of a single-phase solid solution. A similar conclusion was also drawn in a study of the high-entropy system AlCrFeCoNiCu.[71]

The authors of another publication[72] studied a nanocrystalline high-entropy alloy AlCrCuFeNiZr prepared by mechanical alloying followed by hot compaction at 600 °C and pointed that the entropy of mixing is a limited criterion for the formation of a single-phase solid solution. For instance, the structure of the mechanically compacted multicomponent alloy represented a bcc matrix containing a small amount of the fcc phase. After hot compaction, the alloy structure was a bcc matrix comprised of alternating solid Ni – Al and Cr – Fe phases separated by a more plastic α-phase. Eventually, it was concluded that in a multicomponent system, the thermodynamic stability of the solid solution is determined by the Gibbs free energy of all competing phases. The authors of that study believe that the attainment of such a state requires a high mutual solubility of the constituent elements.

The use of the entropy of mixing as the key criterion for structure formation in high-entropy systems casts some doubt after thorough comparison of experimental data.[73] To understand what are the factors responsible for structure formation, it was assumed that if a constituent element of the alloy CoCrFeMnNi (Ref. 74) can be replaced by some other element with close electronegativity and atomic radius provided the same total number of the constituent elements, the configurational entropy and, hence, the structural type of the alloy should be the same. The electron micrographs of the annealed samples of the alloys under study are shown in Fig. 8. As can be seen, initially one deals with the single-phase alloy CoCrFeMnNi with a fcc lattice. The formation of large extended grains is first of all due to directed crystallization in the course of casting. The alloys prepared after replacement of Co, Cr, Fe and Ni by Ti, Mo (or V), V and Cu, respectively, were characterized by high configurational entropy. Nevertheless, the single-phase structure was obtained only in the initial multicomponent system (see Fig. 8 *a*). The modified alloys represented mixtures of several solid-solution phases or mixtures of intermediate (σ, μ, χ) phases and Laves phases.

Changes in the Gibbs free energy were analyzed by comparing the energies of binary compounds in the equilibrium state and in a state corresponding to perfect solid solution.[73] A study of the initial alloy CoCrFeMnNi showed that the Gibbs free energy only slightly deviated towards negative values compared to the Gibbs free energy of the perfect solid solution with the fcc structure (see Fig. 3 in Ref. 73). It follows that the thermodynamic properties of the alloy CoCrFeMnNi are close to those of the perfect solid solution whose configurational entropy prevents the formation of ordered structures. The Gibbs free energies of the modified alloys significantly deviate from the Gibbs free energy of the perfect solid solution. These results agree with the results of studies of the microstructures of these alloys, which revealed the formation of ordered intermediate structures and intermetallics (see Figs 4 – 7 in Ref. 73).

The aforesaid suggests that the entropy of mixing is a necessary but insufficient criterion for the formation of a single-phase solid solution because the influence of the enthalpy of mixing and the non-configurational entropy contributions to the Gibbs free energy should also be taken into account. If the constituent elements of a high-entropy alloy are characterized by negative enthalpy of mixing, more complex structures containing intermetallics, phase separation, ordered phases, *etc*. are formed; in this case, high-entropy alloys are also characterized by high configurational entropy. A disordered single-phase solid solution can also form at low entropy of mixing (no need for increasing the number of constituent elements).[75] Because of this the notion 'high-entropy alloy' casts some doubt. A disordered solution whose entropy of mixing fully compensates the influence of both positive and negative enthalpy can form only for particular elemental compositions.[67, 68, 74] Taking into account this fact, the notion 'high-entropy alloy' includes not only the influence of the high entropy of mixing, but also the ability to form disordered solid

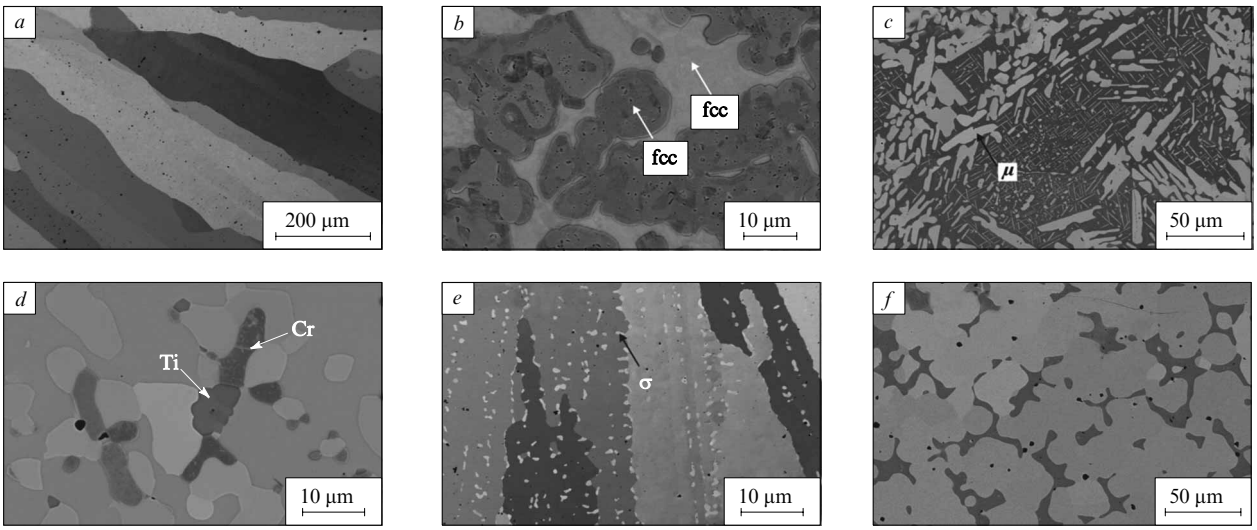


Figure 8. Electron micrographs of the annealed samples of high-entropy systems.[73]
Single-phase structure of CoCrFeMnNi (*a*); CoCrFeMnCu, arrows point to two fcc phases (*b*); CoMoFeMnCu, μ is the intermetallic phase containing 38% – 40% Mo, 20% – 21% Co and 19% Fe (*c*); TiCrFeMnNi (*d*); CoVFeMnNi (*e*) and CoCrVMnNi (*f*).

solutions; it seems appropriate to treat alloys that do not obey this rule as multicomponent ones.

II.6. Phase formation conditions for high-entropy alloys

The rules of formation of solid solutions are inapplicable to high-entropy alloys. A traditional design of alloys assumes the use of one or two principal elements. According to the classical Hume–Rothery rule, the formation of a solid solution requires that the atomic radii and electronegativities of the constituent elements be close.[192] If this rule is violated, the formation of ordered compounds rather than solid solutions is highly probable. In the high-entropy alloys, lattice sites are equally accessible to all atoms of the constituent elements; therefore, all elements can be treated as solution components.

The authors of Ref. 76 analyzed the structure of high-entropy alloys and formulated three principles of formation of solid solutions:

— high entropy of mixing requires that the number of principal elements be at least five;

— the atomic radii of the elements should differ by at most 12%; and

— the enthalpy of mixing should vary between −40 and 10 kJ mol^{-1}.

Further studies of stabilization factors of the formation of solid solutions made it possible to determine more accurate parameters,[48, 77, 78] namely, the coefficients Ω and δ. The parameter Ω takes into account the influence of the entropy and enthalpy of mixing as well as the melting point on the formation of a solid solution

$$\Omega = \frac{T_m \Delta S_{mix}}{|\Delta H_{mix}|}$$

$$T_m = \sum_{i=1}^{n} c_i (T_m)_i$$

where T_m is the average melting point of the n-element alloy and $(T_m)_i$ is the melting point of the ith element.

It should be noted that Ω value is used to assess the ability to form a solid solution. High entropy favours a significant increase in the degree of mixing and a decrease in the Gibbs free energy. In accordance with the Gibbs equation, a decrease in the Gibbs free energy leads to more probable formation of random solid solutions rather than intermetallics. Clearly, the contribution of the entropy of mixing to the formation of such a structure increases at elevated temperatures. The enthalpy of mixing also has a pronounced effect on structure formation. Namely, at negative enthalpy of mixing, one deals with the formation of more complex compounds (intermetallics); at positive enthalpy of mixing, the degree of mixing is lower, which leads to segregation of elements in the alloy. Solid solutions, *i.e.*, systems with random arrangement of atoms in lattice sites, can be formed only at zero enthalpy of mixing.

To describe the influence of the atomic radii differences between the constituent elements, the parameter δ can be written as follows:

$$\delta = \sqrt{\sum_{i=1}^{n} c_i \left(1 - \frac{r_i}{\bar{r}}\right)^2}$$

where r_i and c_i are, respectively, the atomic radius and concentration (at.%) of the ith component and

$$\bar{r} = \sum_{i=1}^{n} c_i r_i$$

is the average atomic radius. Large mismatch between the atomic radii of elements has strong effect on the formation of solid solutions. Severe lattice distortion causes the strain energy and, hence, the Gibbs free energy to increase; this makes the formation of a solid solution less probable.

To better characterize the collective behaviour of the constituent elements in high-entropy systems, it was proposed to use two parameters, the electronegativity difference ($\Delta\chi$) and the valence electron concentration (VEC).[69, 79] The parameter $\Delta\chi$ is defined according to the classical Hume–Rothery rule

$$\Delta\chi = \sqrt{\sum_{i=1}^{n} c_i (\chi_i - \bar{\chi})^2}$$

where χ_i is the Pauling electronegativity of the ith element,

$$\bar{\chi} = \sum_{i=1}^{n} c_i \chi_i$$

The parameter $\Delta\chi$ has almost no effect on the formation of solid solutions or amorphous phase;[69] however, recent studies [75] showed that large $\Delta\chi$ values favour the formation of more complex compounds (*e.g.*, intermetallics).

As mentioned above, high-entropy alloys mainly form single-phase substitutional solid solutions with the fcc or bcc lattices. Attempts to prepare an alloy with the hcp lattice failed.[80] The valence electron concentration can also be used to predict the formation of intermetallics (see, *e.g.*, Refs 193 and 194); this parameter is defined by:

$$\mathrm{VEC} = \sum_{i=1}^{n} c_i (\mathrm{VEC})_i$$

where $(\mathrm{VEC})_i$ is the VEC of the ith element. According to Liu and co-workers,[79] VEC is a physical parameter that governs the probability of formation of solid solution phases with the bcc and fcc lattices. At high VEC values ($\geqslant 8$), the bcc phase is formed; at $6.87 < \mathrm{VEC} < 8$, a fcc + bcc mixed structure is formed; at lower VEC values (6.87), the fcc phase is formed.

Based on analysis of the structures of high-entropy systems, one state that the formation of a solid solution is probable at $\Omega > 1.1$ and $\delta \leqslant 6.6\%$ (Fig. 9).

Studies [81, 82] are of interest because they allow one to understand the sense of the criteria used to predict the structural type of high-entropy alloys. An attempt to predict the formation of fcc or bcc phases in the high-entropy alloys was made using the CALPHAD (CALculation of PHAse Diagrams) method.[81] The results obtained suggest that the CALPHAD approach enables more accurate prediction of the formation of structure with the bcc lattice. Calculations of structures with more close-packed fcc lattice are accompanied by pronounced kinetic effects, which complicates the prediction.

It should be noted that thermodynamic analysis of phase formation in high-entropy alloys made it possible to introduce a number of new parameters, *e.g.*, the mismatch entropy ($\Delta S_\sigma/k$) and the entropy of melting (ΔS_m).[195] The mismatch entropy is a measure of the difference between the

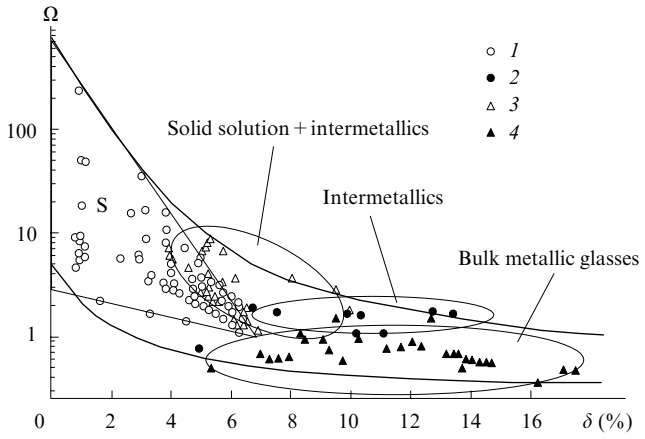


Figure 9. Relationships between the parameters Ω and δ for high-entropy systems.[77]
Solid solution (*1*), intermetallics (*2*), solid solution + intermetallics (*3*) and bulk metallic glasses (*4*).

constituent elements and can be found from the Percus–Yevick integral equation

$$\frac{\Delta S_\sigma}{k} = \frac{3(\zeta^2-1)y_1}{2} + \frac{3(\zeta-1)y_2}{2} - \left[\frac{(\zeta-1)(\zeta-3)}{2} + \ln\zeta\right](1-y_3),$$

$$\zeta = \frac{1}{1-\xi}$$

where ξ is the atomic packing coefficient and the coefficients y_1, y_2, y_3, k can be found from, *e.g.*, Eqns (8), (9), (10) and (11) in Ref. 81.

The entropy of melting is given by

$$\Delta S_m = \sum_{i=1}^{i=n} \Delta S_{m,i}$$

where $\Delta S_{m,i}$ is the entropy of melting of the ith constituent element in the alloy.

The results of studies on correlations between the mismatch entropy and the enthalpies of mixing calculated by the Miedema (ΔH_M) and CALPHAD ($\Delta H_{CALPHAD}$) methods are shown in Fig. 10. The $\Delta S_\sigma/k$ criterion is a topological parameter that describes lattice distortion due to the presence of different types of the constituent atoms. From the data presented in Fig. 10 it follows that the fcc structure is characteristic of the systems having higher ΔH_{mix} and small $\Delta S_\sigma/k$ values; the bcc structure is characteristic of the systems with small ΔH_{mix} values and high $\Delta S_\sigma/k$; the mixture of structures, fcc + bcc, corresponds to intermediate values of both parameters.

The structure of the high-entropy alloys was assessed[82] using the product $\Delta H_h \Delta S$ (ΔH_h is the enthalpy of formation of vacancies), which is believed to characterize the trend to formation of intermetallics. Based on the $\Delta H_h \Delta S$ values for the available high-entropy alloys, single-phase solid solution with either fcc or bcc lattice are tend to form at small values of this parameter; an increase in this parameter is

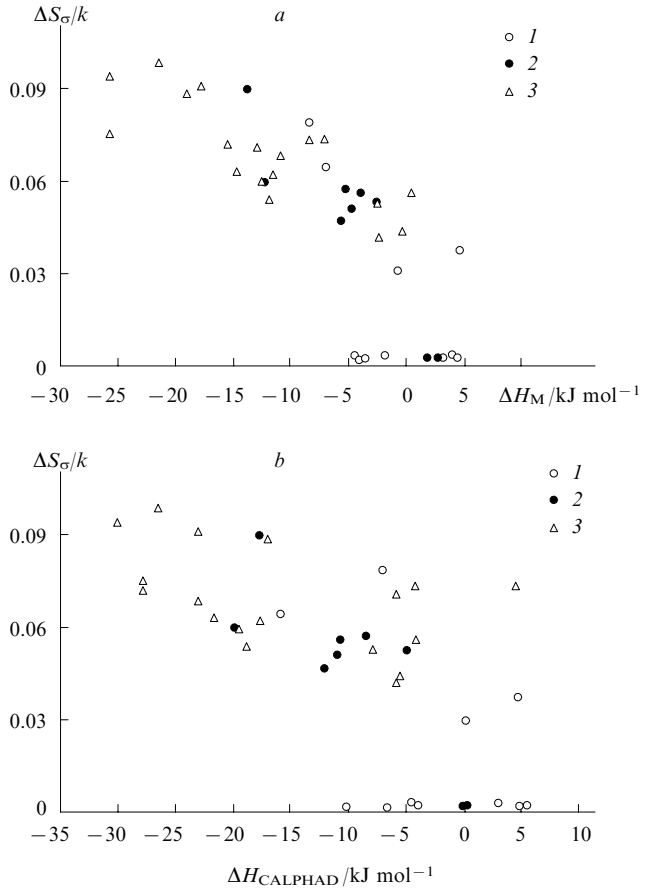


Figure 10. Relationships between the mismatch entropy and the enthalpy of mixing values calculated according to Miedema (*a*) and using the CALPHAD method (*b*) for equiatomic alloys.[81]
Lattice type: fcc (*1*), fcc + bcc (*2*) and bcc (*3*).

followed by the formation of two and more structures and an amorphous phase. It should be noted that manganese-containing alloys do not obey this rule, probably due to intense evaporation in the course of melting.

The formation of a structure with a high degree of crystallinity becomes less probable with increasing the number of the constituent elements; therefore, a question arises as to the influence of the entropy of mixing on the formation of amorphous phase. This issue was studied in most detail by Liu and co-workers,[69,83] who evaluated the parameters ΔH_{mix}, $\Delta\chi$, δ, ΔS_{mix} and VEC for the known high-entropy systems. Based on the data from Ref. 69, it was found that solid solutions are formed at small, either positive or negative, values of the enthalpy of mixing, small atomic radii differences and high entropy of mixing. The amorphous phase is formed at large negative ΔH_{mix} values, large atomic radii differences and small ΔS_{mix} values (Fig. 11). It should be emphasized that the equimolar ratio of the constituent elements is of secondary importance.

The main criteria for amorphous phase formation include the enthalpy of mixing and the atomic radii difference (the larger the value of this parameter the more severe the lattice distortion of the alloy).[69] Above a critical elastic strain the system becomes topologically unstable and a glass transition may occur. Negative enthalpy of mixing favours the formation of short-range clusters. However, if the

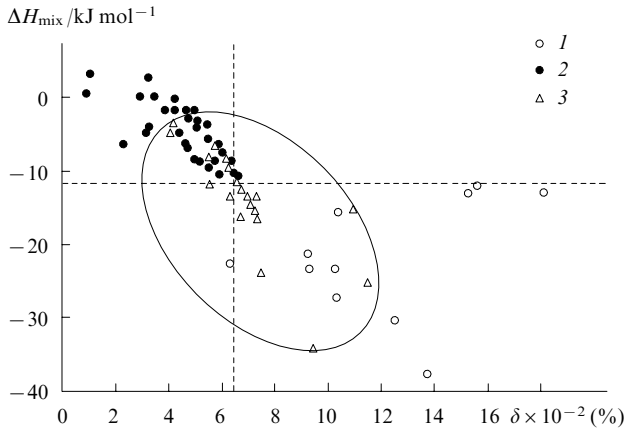


Figure 11. Correlation between ΔH_{mix} and δ values for high-entropy alloys.[83]
Amorphous phase (*1*), solid solution (*2*) and intermetallics (*3*).

atomic radii difference is relatively small in this case, the formation of intermetallics is more probable.

Summing up, the set of parameters including ΔH_{mix}, δ, $\Delta\chi$, ΔS_{mix} and VEC is insufficient to predict the structure of high-entropy alloys. Clearly, one should also use other parameters mentioned above ($\Delta S_\sigma/k$, $\Delta S_{conf}/\Delta S_f$, $\Delta H_h \Delta S$), take into account the role of each constituent element in the formation of a particular structure and study the influence of the enthalpy of mixing in more detail. It is still unclear how the amount of tightly bound pairs of atoms influences the formation of amorphous or intermetallic phase and the critical strain corresponding to glass transition. Also, researchers should pay attention to the destabilizing effect of the enthalpy of mixing on the solid solution if coatings are prepared at relatively low temperatures (several hundreds degrees Celsius).

II.7. Computer simulation of the structure and properties of high-entropy alloys

Computer simulation belongs to the most reliable and efficient tools for thermodynamic description of various systems (binary, ternary, multicomponent alloys, *etc.*). High-priority problems in this field include, in particular, construction of constitutional diagrams, calculations of thermodynamic processes and investigations of the structural and electronic properties of various alloys.

In the aforesaid we considered main thermodynamic prerequisites to formation of high-entropy alloys taking into account experimental data. To date, numerous publications concerning the application of computer simulation in studies of high-entropy alloys are available. An analysis of these results can help in understanding fundamental features of formation (preparation) of high-entropy alloys.

The growth and thermal stability of films based on the high-entropy alloy AlCoCrCuFeNi were studied by molecular dynamics for the temperature range from 300 to 1500 K.[84] Simulation of the deposition of 10 000 atoms on the Si(100) substrate revealed the formation of clusters 25 to 50 Å in size. Simulation of annealing under different temperature conditions predicted coalescence of clusters. When constructing the trajectory of the motion of iron atom, mention was made that raising the temperature leads to higher mobility of atoms and thus even greater atomic displacements. Above 850 K, intra-cluster atomic motions begin and the root-mean-square atomic displacements reach maximum values above 1400 K. A transition from the bcc to fcc structure was also established by variable temperature X-ray diffraction analysis.[84]

The phase diagrams of high-entropy alloys represent graphical interpretation of phase transformations at particular ratios of the constituent elements and upon changes in external conditions. Using a phase diagram, one can determine the necessary composition for the preparation of a desired microstructure. Phase diagrams for binary and ternary alloys can be constructed with ease, but the problem complicates and becomes labour-consuming in the case of multicomponent systems. The CALPHAD method[196, 197] provides a thermodynamic description of a multicomponent system and predicts its equilibrium state.

This approach was used to construct[85] the phase diagrams of CoCrFeMnNi,[73] CoCrFeMnCu,[73] CrNbTiVZr (Ref. 184) and to demonstrate how each constituent element influences the stability of the alloy structure. A more detailed study of the phase diagram of the high-entropy alloy Al_xCoCFeNi is available.[86]

The phase diagram of the alloy Al_xCoCrFeNi is shown in Fig. 12. At $x < 0.75$, the solidified phase has a fcc structure; at $x > 0.75$, a bcc structure is formed. This is in excellent agreement with experimental data.[87–89] Using thermodynamic simulation of nonequilibrium solidification (Scheil model), the structure of the alloy was studied as function of the temperature and concentration of aluminium. The results obtained are presented in Fig. 13. Al low aluminium concentration, mainly the fcc structure is formed (at $x = 0.3$, the fraction of the bcc structure is only 2.3%); at $x > 0.8$, the solidified phase has the bcc structure. According to calculations, the fcc structure can exist even at $x = 2$, but this was not confirmed experimentally. A

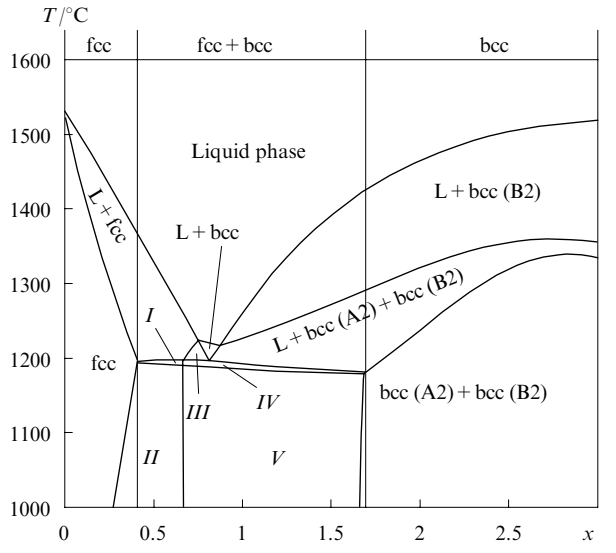


Figure 12. Phase diagram of the high-entropy alloy Al_xCoCrFeNi constructed using the CALPHAD method.[86]
L + fcc + bcc + B2 (*I*), fcc + bcc (B2) (*II*), L + fcc + bcc (A2) (*III*), L + fcc + bcc (A2) + bcc (B2) (*IV*) and fcc + bcc (A2) + bcc (B2) (*V*).

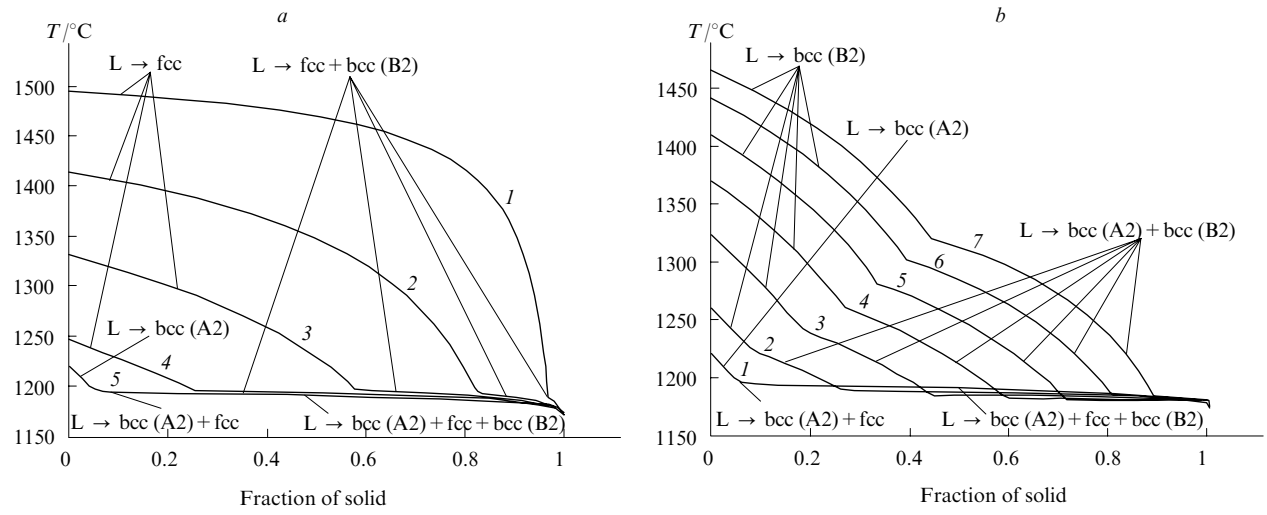


Figure 13. Solidification paths calculated using the Scheil model for the $Al_xCoCrFeNi$ alloy at different temperatures.[86] (*a*): $x = 0.1$ (*1*), 0.2 (*2*), 0.3 (*3*), 0.4 (*4*), 0.5 (*5*); (*b*): $x = 0.8$ (*1*), 1 (*2*), 1.2 (*3*), 1.4 (*4*), 1.6 (*5*), 1.8 (*6*), 2 (*7*).

study of the influence of the concentrations of other elements revealed the stabilizing effect of chromium atoms on the disordered bcc structure and their destabilizing effect on the ordered fcc structure; cobalt, iron and nickel atoms stabilize the fcc phase at relatively low aluminium concentration.

An analysis[190] of the structure and properties of the multicomponent alloys NbTiVZr, $NbTiV_2Zr$, CrNbTiZr and CrNbTiVZr using the Scheil model and calculations of the equilibrium phase diagrams showed that under non-equilibrium solidification conditions, the alloys NbTiVZr and $NbTiV_2Zr$ form single-phase disordered solid solutions with the bcc structure and a secondary phase content of $<1\%$. The secondary phase found in the Cr-containing alloys represents the Laves phases based on chromium and zirconium ($\sim 91\%$). The equilibrium phase calculations for all alloys predicted a single phase with disordered bcc structure below the corresponding melting points. At lower temperatures, the appearance of small amounts of secondary phases and the Laves phases is expected. A comparison of the phase diagrams and experimental data showed that the volume fractions and compositions of the bcc phases determined for these alloys at room temperature approximately correspond to those of the equilibrium phases at temperatures between ~ 600 and 750 °C.

The results of the CALPHAD calculations[90] of the equiatomic alloys CrCoCuNi and CrCuMnNi agree with experimental data. The authors of that study predicted the structures of the phases and estimated their volume fractions and compositions.

High-entropy alloys were also simulated by the molecular dynamics method.[91,92] In particular, the temperature dependent chemical order in the Mo–Nb–Ta–W system was studied by a hybrid approach 'Monte Carlo/molecular dynamics'.[91] The other study[92] involved a molecular dynamics simulation of the alloy NiAlCuCoTiVZnZr after quenching. It was found that the degree of disorder increases with the number of the constituent elements. A quantitative analysis of the radial distribution functions showed that the melt quenched multi-element alloy mainly forms an amorphous phase if it contains at most four elements and a fluid-like phase if the number of elements is at least five.

Ab initio calculations of the influence of intermetallics on the high-entropy alloys were reported.[93] The results of calculations of the lattice constants, enthalpy of formation, binding energies, density of electronic states and elastic constants were used for characterization of intermetallics formed in the high-entropy alloys of particular chemical compositions.

Atomistic simulation (mathematical description of atom–atom interactions) was used for quantitative description of transition to the high-entropy state.[94] It was shown that the lattice constants, binding energies and the bulk elastic modulus of the high-entropy alloy $(WNbMoTa)V_n$ are significantly influenced by the vanadium concentration.

An approach to prediction of stable single-phase structures in high-entropy alloys was developed using the *ab initio* molecular dynamics (AIMD) and CALPHAD methods.[95] The former method was used to study the nature of the atom–atom interactions, while the latter was utilized in the phase diagram calculations. The partial pair correlation functions of the high-entropy alloy $Al_{1.3}CoCrCuFeNi$ obtained from the AIMD calculations are shown in Fig. 14. The highest peaks of the pair correlation functions correspond to the short-range order for the Al–Ni, Co–Cr and Cr–Fe pairs of atoms in the liquid. As a consequence, solidification is accompanied by the formation of the NiAl (B2) (Ref. 58) and CrCoFe (Ref. 61) phases. A small peak of the Cu–Cu pair characterizes the formation of the copper-rich phase; this was confirmed experimentally.[5,58]

The partial pair correlation functions of the high-entropy alloy HfNbTaTiZr are distributed more uniformly; this suggests a random distribution of atoms over the lattice sites and, as a consequence, the possibility of formation of a single-phase solid solution with the bcc structure. Thus, the formation of a single-phase solid solution is more probable provided that there is no short-range order and segregation of the elements in the liquid.

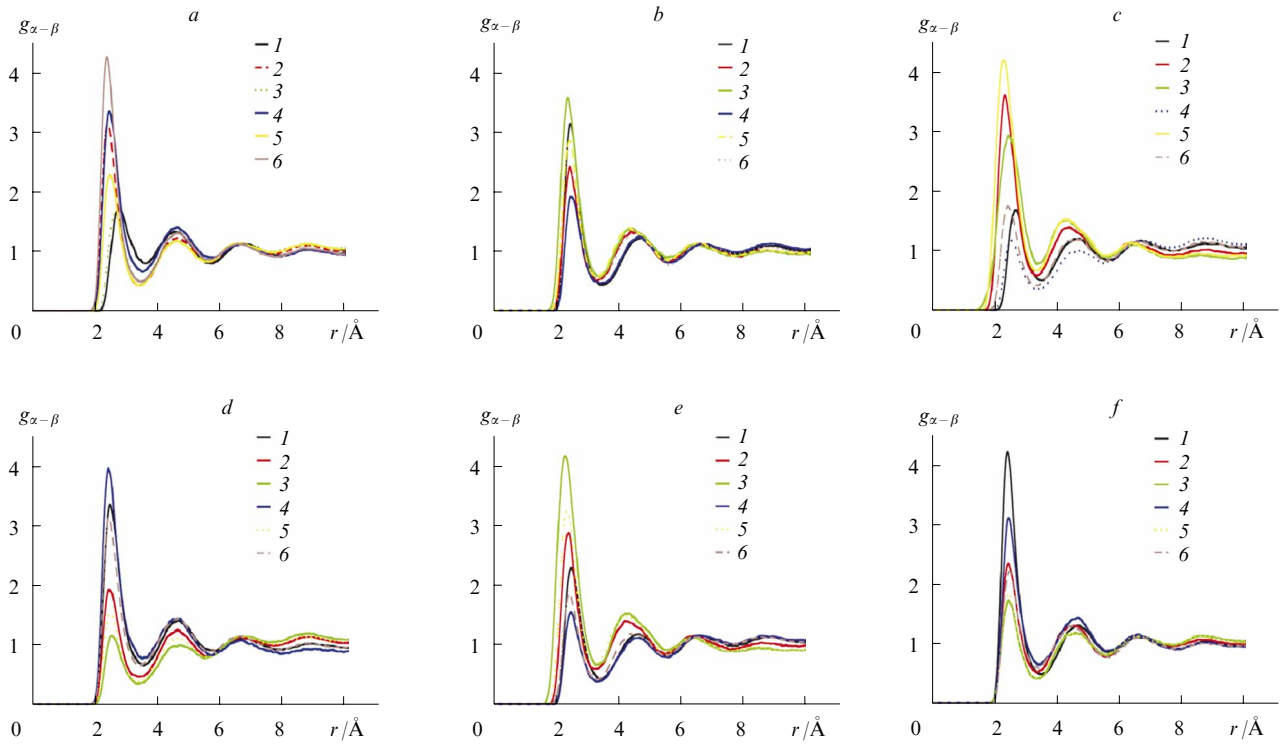


Figure 14. Partial pair correlation functions ($g_{\alpha-\beta}$, where $\alpha-\beta$ are pairs of atoms) obtained from AIMD calculations for high-entropy alloy $Al_{1.3}CoCrCuFeNi$ at 1873 K.[95]

Figure	Pairs of atoms $\alpha-\beta$					
	1	*2*	*3*	*4*	*5*	*6*
a	Al–Al	Al–Co	Al–Cr	Al–Cu	Al–Fe	Al–Ni
b	Co–Al	Co–Co	Co–Cr	Co–Cu	Co–Fe	Co–Ni
c	Cr–Al	Cr–Co	Cr–Cr	Cr–Cu	Cr–Fe	Cr–Ni
d	Cu–Al	Cu–Co	Cu–Cr	Cu–Cu	Cu–Fe	Cu–Ni
e	Fe–Al	Fe–Co	Fe–Cr	Fe–Cu	Fe–Fe	Fe–Ni
f	Ni–Al	Ni–Co	Ni–Cr	Ni–Cu	Ni–Fe	Ni–Ni

III. Methods of preparation of high-entropy alloys and coatings based on them

Often (see, *e.g.*, Refs 58, 67, 96–99), the emphasis is placed on the search for structure–propertiy relationships for high-entropy alloys prepared by different methods under different conditions. An analysis of experimental data revealed dependence of the desired properties on the elemental composition, methods of preparation, changes in the concentrations of the constituent elements and many other factors.

III.1. Methods of preparation of high-entropy alloys

There is a variety of methods for preparation of high-entropy alloys, *viz.*, casting,[36, 56, 58, 74, 96, 100–104] mechanical alloying,[70, 72, 99, 105–113] laser cladding,[114–116] *etc.*[117–119]

The most widely used methods include combinations of casting with melting — arc,[56, 57, 96] induction,[120] electric arc.[104] An analysis of published data shows that as-cast high-entropy alloys form simple solid solutions with typical dendritic structures with segregation regions that were found in both dendrites and interdendrites.

A study on the microstructure of the high-entropy alloy $Al_{0.5}CoCrCuFeNi$ revealed dendritic and interdendritic (copper-rich) regions.[100] It was assumed that copper segregation is due to a low degree of mixing of Cu with other constituent elements. Similar results were also obtained in the studies of $Al_x(TiVCrMnFeCoNiCu)_{100-x}$,[121] $Al_{0.5}CoCrCuFeNiTi_x$,[122] and $FeCoCuNiSn_x$.[123] It should be noted that changes in the titanium concentration in the interdendritic region of the alloy $Al_{0.5}CoCrCuFeNiTi_x$ are followed by the formation of needle-shaped precipitates (nanometre-sized needles). The alloy $FeCoCuNiSn_x$ has a typical dendritic crystal structure with mainly iron- and cobalt-rich dendrites and copper- and tin-rich interdendrites. An increase in the tin concentration leads to greater enrichment of the interdendritic region with tin. Above a critical value of $x \geqslant 0.07$ one deals with the formation of nanosized precipitates representing an intermetallic $Cu_{81}Sn_{22}$.

Negative enthalpy of mixing favours the formation of intermetallics; in other words, different ordered structures can form at negative enthalpy of mixing (or higher binding energy) and high concentrations of corresponding elements.

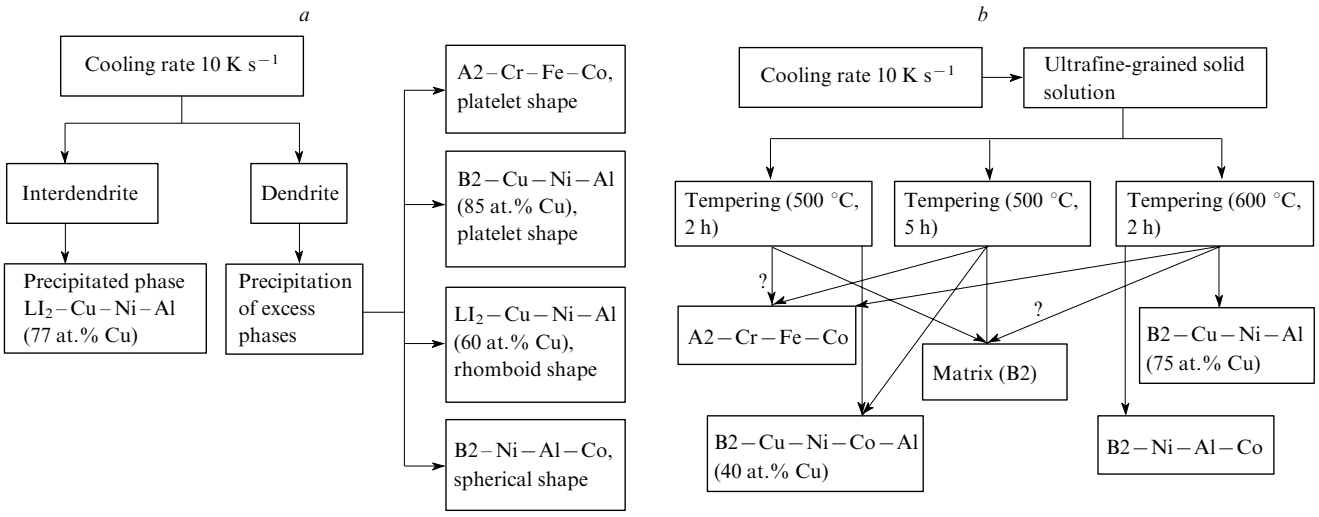


Figure 15. Schematic illustration of the decomposition of as-cast (*a*) and melt-quenched (*b*) alloy AlCrFeCoNiCu.[35]

For instance, the evolution of the microstructure of the high-entropy alloy $Al_{0.5}CoCrFeNi$ aged at different temperatures in the range from 350 to 950 °C involves the formation of the matrix (fcc + bcc), as well as the droplet-shaped, wall-shaped and needle-shaped phases.[101] The droplet-shaped phase was both Al- and Ni-rich, thus corresponding to the high chemical affinity between these elements (negative enthalpy of mixing). Raising the ageing temperature was followed by a decrease in the percentage of the droplet-shaped phase due to an increase in the diffusion coefficients. The formation of intermetallics upon an increase in titanium concentration in the high-entropy alloy $Al_{0.5}CoCrCuFeNiTi_x$ was reported.[122] At $x = 1.2$, CoCr and Ti_2Ni are formed in the dendritic phase.

Studies of the dependence of the structure of high-entropy alloys prepared by different methods on the crystallization rate are of particular interest and importance.

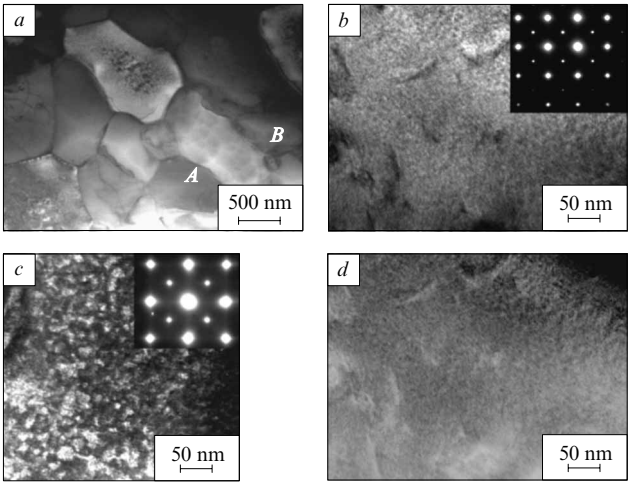


Figure 16. Typical bright-field (*a*, *b*) and dark-field (*c*, *d*) TEM images of the alloy AlCrFeCoNiCu after melt quenching.[35]
Area *A* in the 100_{B2} reflection (*c*) and area *B* in the 200_{B2} reflection (*d*). Insets: electron microdiffraction patterns corresponding to the zone axis of the reflection planes $[001]_{B2}$.

Examples of detailed studies are provided by Refs 35 and 61. High-entropy alloy AlCrFeCoNiCu was melted out in argon atmosphere. The ingot was made chemically homogeneous by fivefold re-melting and cooled at a rate of 10 K s^{-1}. Then, part of the ingot was melt quenched at a cooling rate of $10^6 - 10^7$ K s^{-1}. Examination showed that slow cooling is accompanied by the formation of dendritic (bcc) and interdendritic (fcc) phases, which undergo spinodal decomposition with precipitation of cubic phases of the A2, B2 and LI_2 types (Fig. 15 *a*) differing from one another in elemental composition and morphology.

Melt quenching followed by heat treatment leads to formation of an ultrafine-grained structure containing no dendrites (Fig. 16). Transmission electron microscopy (TEM) studies revealed a B2-type nanodomain superstructure. Further thermal annealing leads to formation of a small number of crystalline multicomponent cubic phases (both ordered and disordered) and to appearance of some other features of the structural and phase state.[35]

Bridgman directional solidification consists in crystallization of a material in a furnace with a longitudinal temperature gradient. Evolution of the microstructure of high-entropy alloys under Bridgman solidification conditions was studied.[30, 124, 125] Photomicrographs of the high-entropy alloy CoCrFeNiAl prepared by casting and by the Bridgman method clearly demonstrate the formation of a typical dendritic microstructure in the former and equiaxed grains in the latter case (see Fig. 17). Transition from dendritic microstructure to equiaxed grains was interpreted[124] as being due to (i) the growth and coarsening of the primary dendrites (taking into account a relatively low melting point of interdendrites); (ii) large value of the temperature-gradient-to-growth-rate ratio; and (iii) the residual thermal stress.[124]

Mechanical alloying represents yet another widely used method for preparation of high-entropy alloys with more homogeneous and stable nanocrystalline structures. The technique utilizes powdered components milled in a high-energy ball mill. Repetitive colisional breakdown of powder particles and cold welding in the mill make it possible to prepare homogeneous powders.[70, 72, 99, 109, 106 – 111]

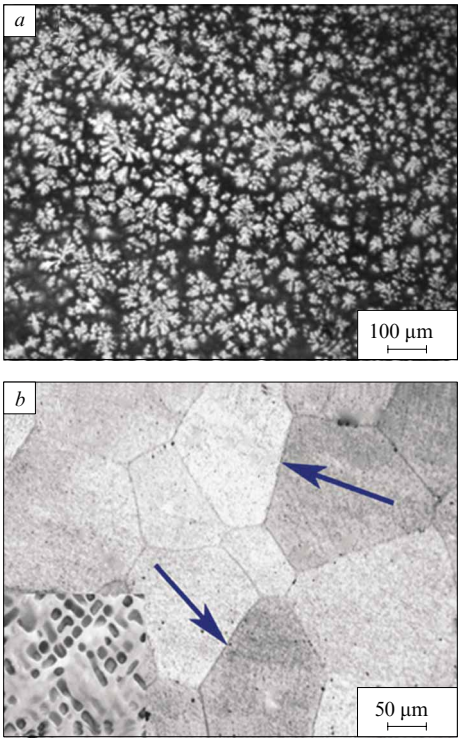


Figure 17. Photomicrographs of the high-entropy alloy CoCrFeNiAl prepared by casting (*a*) and by Bridgman method (*b*).[125]
Grain boundaries are shown by arrows. Inset in Fig. *b*: magnification of a grain fragment.

Transmission electron microscopy images of the high-entropy powder alloy CoCrFeNiTiAl prepared at different milling duration are shown in Fig. 18.[106] Breakdown of agglomerates into smaller particles with increasing milling duration is clearly seen. The average particle size after 30-h milling was <5 μm. It should be noted that milling over a period of 60 h reduced the surface roughness and led to formation of spherical particles.

An experimental study on the evolution of the microstructure of alloys based on Cu, Ni, Al, Co, Cr, Fe, Ti and Mo was reported.[105] The X-ray diffraction patterns of the powders of alloys prepared at different milling duration are presented in Fig. 19. Their examination revealed the preferred formation of the fcc structure. Doping with Cr, Fe, Ti and Mo, as well as an increase in milling duration lead to formation of amorphous phase. This was explained assum-

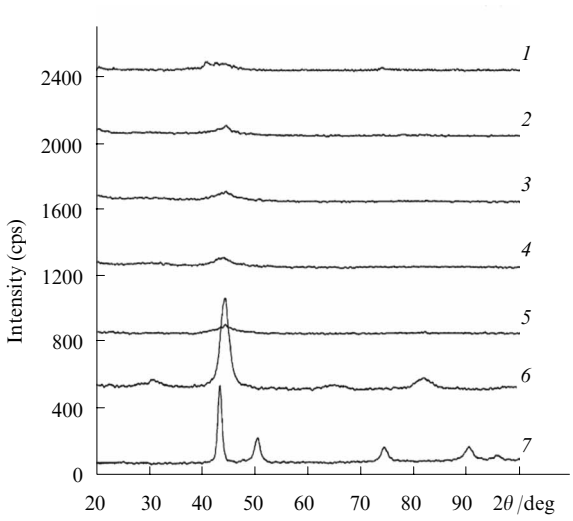


Figure 19. X-Ray diffraction patterns of alloy powders prepared with milling duration of 60 (*1*, *3*, *5*–*7*) and 36 h (*2*, *4*).[105]
$Cu_{0.5}NiAlCoCrFeTiMo$, Mo + amorphous phase (*1*); $Cu_{0.5}NiAlCoCrFeTi$, amorphous phase (*2*); $Cu_{0.5}NiAlCoCrFe$, amorphous phase (*3*); $Cu_{0.5}NiAlCoCr$, amorphous phase (*4*); $Cu_{0.5}NiAlCo$, amorphous phase (*5*); $Cu_{0.5}NiAl$, ordered bcc structure (*6*) and $Cu_{0.5}Ni$, fcc structure (*7*).

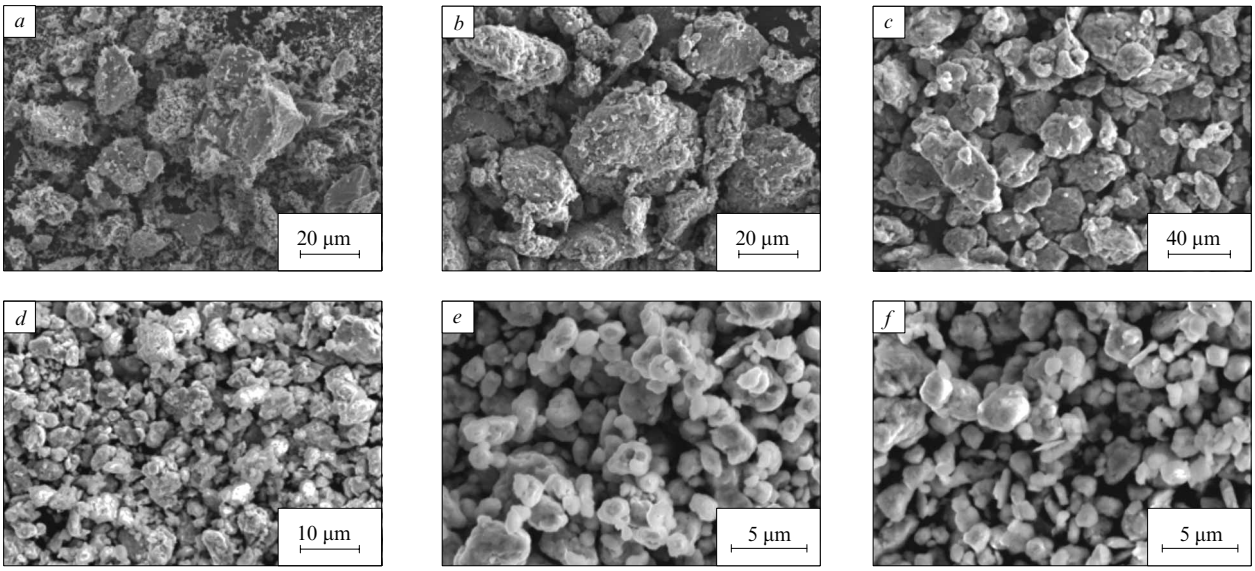


Figure 18. TEM images of the high-entropy powder alloy CoCrFeNiTiAl.[106]
Milling duration /h: 0 (*a*), 6 (*b*), 18 (*c*), 30 (*d*), 60 (*e*) and 60 + 2 h wet milling (*f*).

ing that the phase transition is related to complete solubility of the elements only upon long-term milling (36 h for Fe and 60 h for Cr). Thus, long-term milling of the alloys containing from 4 to 8 elements is followed by a phase transition from the fcc structure to amorphous state. This is the type-I process† leading to formation of amorphous state.[198]

The structures of the high-entropy alloys prepared by unusual methods, *e.g.*, laser cladding [$Al_2CrFeNiCoCuTi_x$ (Ref. 114), $Al_2CrFeCoCuTiNi_x$ (Ref. 115), AlCoCrCuFeNi (Ref. 116)], selective laser welding [ZrTiVCrFeNi (Ref. 118)] and thermal sputtering [$(Ni_xCo_{0.6}Fe_{0.2}Cr_ySi_zAlTi_{0.2}$ (Ref. 119)] were also studied. High-entropy alloys prepared by laser cladding are characterized by the formation of three zones, namely, the cladding zone, the bounding zone and the heat affected zone. The cladding zone is composed of thin white nanocrystals,[115] equiaxed grains and columnar crystals.[114] The alloys have a bcc or fcc structure [115] as well as contain the Laves phases.[114] The bounding zone is the junction between the cladding layer and the substrate. The heat affected zone is the zone where the substrate is near the bounding zone.

III.2. Methods for preparation of nitride coatings based on high-entropy alloys

Multi-element composition of high-entropy alloys makes it possible to prepare various nitride coatings based on them, with desired physical and chemical properties that are necessary for, *e.g.*, applications in specific conditions. Nitride coatings based on the multicomponent alloys represent solid solutions with the fcc structure. Using severe lattice distortion and solid solution hardening, one can prepare high-strength nitride coatings for extended range of applications.

Magnetron sputtering deposition is a key method for preparation of thin-film nitride coatings based on high-entropy alloys.[9, 19, 27, 126–132] The method allows one to control the size and orientation (texture) of grains as well as the entire nanostructure.

The advantages of magnetron sputtering over other methods are as follows:

— high sputtering rate at relatively low potentials (600–800 V) and a low gas pressure in the magnetron chamber (0.5–10 Pa);

— no substrate overheating;

— low contamination of films;

— possibility to prepare same-thickness films on relatively large-area substrates.[199]

A characteristic feature of this method for preparation of nitride high-entropy alloys consists in pre-melting of a mixture (often, equimolar) of necessary metals to obtain a target high-entropy alloy. The process is repeated at least five times to achieve a uniform distribution of the elements in the alloy. Then, the target is cut to disks and polish them. Nitride coatings are prepared in the magnetron chamber. Usually, the working gas represents an $Ar + N_2$ mixture. Magnetron sputtering of targets on pre-treated substrates can occur in different regimes by varying the pressure of the working gas in the chamber, the distance from the target to the substrate and the potential applied to the substrate. All these parameters influence the quality and properties of coatings.

Magnetron sputtering is also suitable for preparation of carbide films based on high-entropy alloy. The process is essentially the same as that described above except the composition of the mixture of reactive gases, namely, $Ar + CH_4$.

Consider structural features of nitride coatings in relation to the $(AlCrMnMoNiZrB_{0.1})N$ coating prepared by reactive d.c. magnetron sputtering.[133] Films were synthesized using a $AlCrMnMoNiZrB_{0.1}$ target. The N_2 : Ar flow rate ratio (R_N) was varied from 0 to 1.0. The influence of the partial pressure on the deposition rate is illustrated in Fig. 20.

At high partial pressure of argon, interparticle collisions occur more frequently and the particles lose energy which becomes too low and the substrate becomes inaccessible to the particles. The addition of nitrogen causes the partial pressure of argon to decrease and the deposition rate increases. Further increase in the parameter R_N leads to significant decrease in the deposition rate due to etching of the target. Also, the sputtering efficiency of nitrogen ions decreases compared to that of argon ions.

The diffraction patterns of the coating $(AlCrMnMoNiZrB_{0.1})N$ at different R_N values are shown in Fig. 21. At $R_N = 0–0.2$, one gets an amorphous film owing to (i) high entropy of mixing responsible for an increase in the mutual solubility of metals and (ii) long-range diffusion, which favours retention of the solid solution state). As R_N changes between 0.5 and 1, nitride coatings have a simple fcc structure of the NaCl type. Probably, this structure can be considered as a solid solution based on binary nitrides. Changes in the intensities of peaks corresponding to different orientations of crystallographic planes are clearly seen. As the parameter R_N increases, peaks of the (200) and (220) planes become more intense. It should be noted that the formation of the preferred crystallographic orientation is mainly influenced by the kinetic limitations (mobility of adatom, effects of cascade collisions, anisotropy of surface diffusion).[200–202]

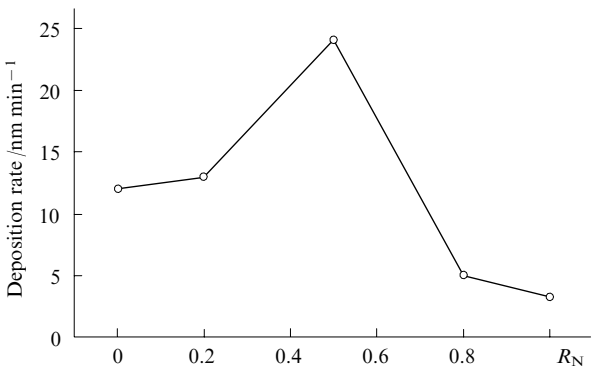


Figure 20. Deposition rate of $(AlCrMnMoNiZrB_{0.1})N$ films plotted *vs.* parameter R_N.[133]

† A study [198] on the structure of the alloy prepared by mechanical doping under different conditions revealed three types of processes leading to the amorphous state. These are a continuous decrease in the effective grain size (as a consequence, the diffraction peak is broadened and shifted); a decrease in the intensity of Bragg reflections and an increase in the intensity of the broader peak; and the formation of intermetallics followed by their transformation into a homogeneous amorphous alloy.

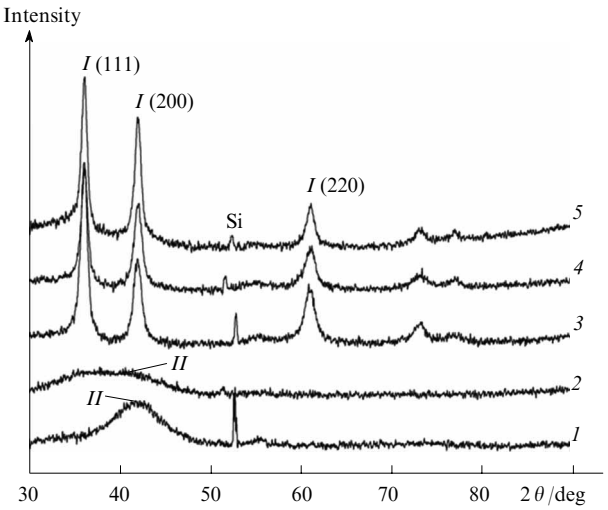


Figure 21. Diffraction patterns of $(AlCrMnMoNiZrB_{0.1})N$ films prepared at different R_N values.[133]
$R_N = 0$ (*1*), 0.2 (*2*), 0.5 (*3*), 0.8 (*4*), 1.0 (*5*); (*I*) fcc phase, (*II*) amorphous phase.

Thus, changes in the nitrogen content cause multiple changes in the film structure from amorphous to mixed and then to crystalline. Similar results were also obtained in studies of the nitride coatings $(AlCrTaTiZr)N_x$,[22] $(TiAlCrSiV)N_x$,[134] $(AlCrMoTaTiZr)N_x$[21] and $(AlCrMoTaTi)N_x$.[135]

Changes in the morphology of the silicon-deposited coatings $(AlCrMnMoNiZrB_{0.1})N$ prepared at different R_N values are illustrated in Fig. 22. As can be seen, the coating prepared at $R_N = 0$ is composed of numerous clusters 100 to 200 nm in size and has a columnar structure with microporous defects. As the partial pressure of nitrogen increases, the character of the surface morphology does not change, but the cluster size decreases. At $R_N = 1.0$, cluster are ~ 50 nm in size and the columnar structure becomes more dense. A smooth surface layer is clearly seen on the coating prepared at $R_N = 1.0$.

Application of high-frequency magnetron sputtering to preparation of nitride coatings based on multicomponent alloys can be exemplified by $(AlCrMoTaTiZr)N_x$.[21] The authors studied how variation of the parameter

$$R_N = \frac{N_2}{Ar + N_2}$$

influences the morphological and structural changes in the coating (Fig. 23).

With no nitrogen, the amorphous surface film AlCrMoTaTiZr is very smooth (roughness is 0.2 nm). An increase in the parameter R_N to 0.1 led to formation of nanosized faceted grains with a roughness of 7.8 nm. Further increase in the parameter R_N was accompanied by successive changes in the morphology from faceted grains to a structure composed of numerous clusters 80–150 nm in size and by a decrease in the surface roughness down to a minimum value of 0.9 nm. A more detailed analysis of the clusters by powder X-ray diffraction revealed nanograins 15–20 nm in size.

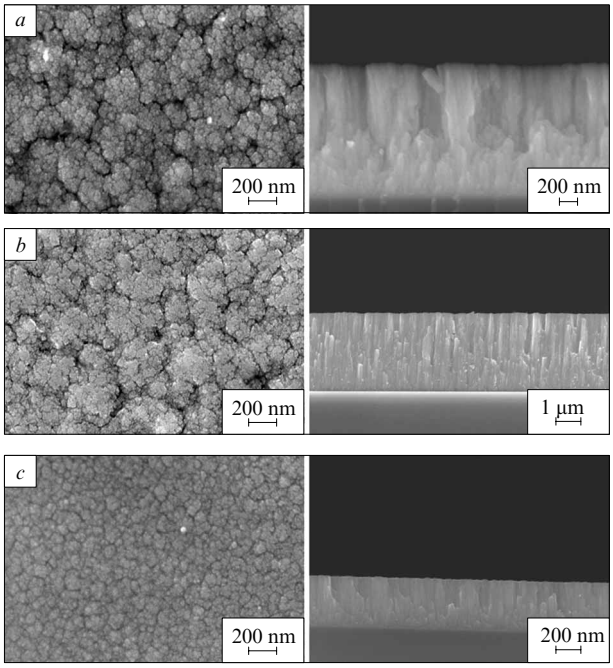


Figure 22. Photomicrographs of $(AlCrMnMoNiZrB_{0.1})N$ coatings deposited on silicon substrate at $R_N = 0$ (*a*), 0.5 (*b*), 1.0 (*c*) illustrating changes in the morphology (on the left) and the structure (on the right).[133]

A TEM image of the cross-section of the AlCrMoTaTiZr nitride coating deposited at $R_N = 0.5$ is shown in Fig. 24. The coating has a clear-cut columnar structure with 15–25 nm wide pillars. The subgrain size determined using the dark-field image is 10 to 20 nm. The selected diffraction area (see inset in Fig. 24) shows a set of diffraction rings corresponding to the (111), (200), (220) and (311) planes of the fcc structure. The high-intensity arcs with a span of 15° indicate the existence of a preferred orientation of subgrains.

Nitride coatings from the multicomponent alloy (TiAlCrZrNb)N were prepared by physical vapour deposition using an electric arc.[38] A distinctive feature of this method consists in higher energy of particles deposited compared to magnetron sputtering. Studies of the phase composition of the coatings revealed two phases based on ZrN and on TiN; other metals (Al, Cr and Nb) seem to dissolve in these two nitrides. The deposition conditions were changed, namely, the electric current at Zr/Nb cathode was increased to 120 A; this led to formation of a single-phase (TiN-based) coating.

The high-entropy alloy TiZrHfVNb was used to prepare nitride coatings by cathodic arc vacuum evaporation.[39] Single-phase non-textured coatings with the fcc lattice formed at the lowest pressure of nitrogen. Depending on the bias potentials, the crystallite size increased from 35 to 50 nm. A gradual increase in the nitrogen pressure led to formation of textured single-phase coatings, whereas an increase in the negative potential at the substrate caused an increase in the crystallite size.

The results of studies on the structure and phase composition of nitride coatings based on multicomponent alloys are presenteed in Table 2.

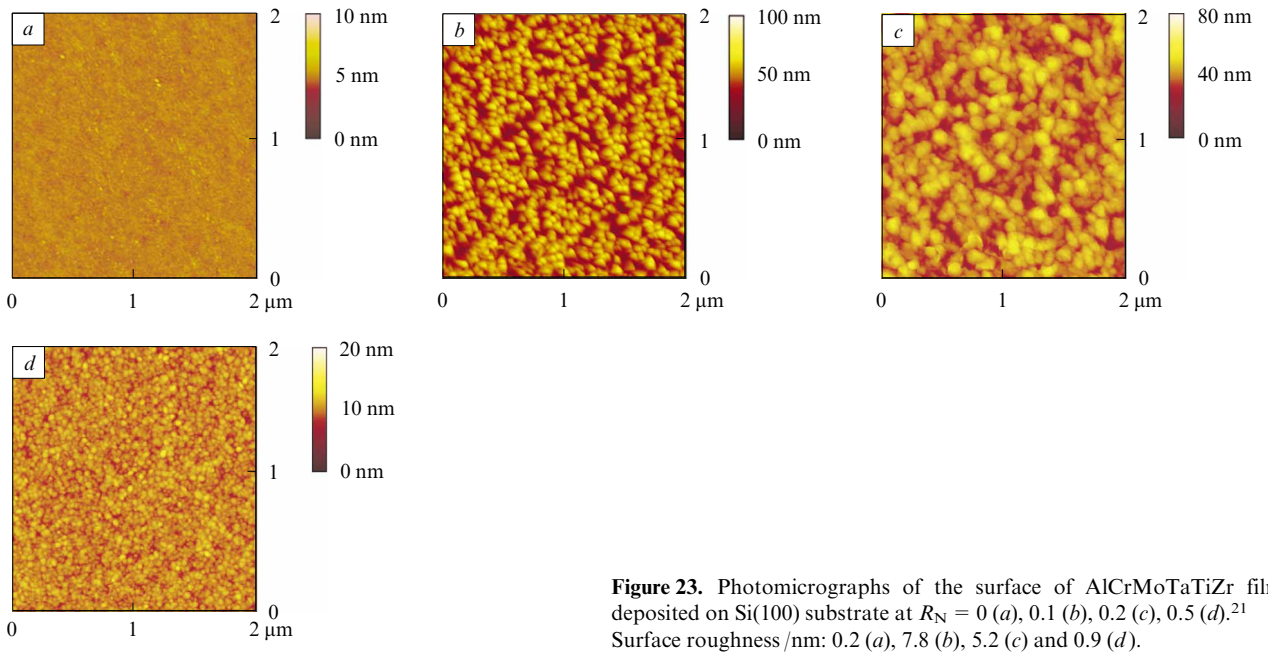


Figure 23. Photomicrographs of the surface of AlCrMoTaTiZr films deposited on Si(100) substrate at $R_N = 0$ (*a*), 0.1 (*b*), 0.2 (*c*), 0.5 (*d*).[21] Surface roughness /nm: 0.2 (*a*), 7.8 (*b*), 5.2 (*c*) and 0.9 (*d*).

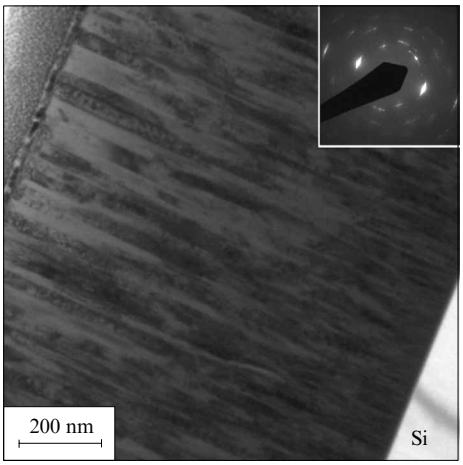


Figure 24. Cross-sectional TEM image of AlCrMoTaTiZr film prepared at $R_N = 0.5$.[21] Inset: selected diffraction zones.

Table 2. Structures of high-entropy nitride coatings.

Coating	State	Ref.
(AlCrMoSiTi)N	solid solution	27
(TiZrNbHfTa)N	crystalline (nanocrystals)/ solid solution	132, 133
(AlCrTaTiZr)N	solid solution	22, 137, 142 – 146
(AlCrNbSiTiV)N	the same	19, 134
(AlCrMoSiTi)N	amorphous/solid solution	136
(TiVCrZrHf)N	solid solution	138
$(AlCrSiTiZr)_{100-x}N_x$	amorphous/crystalline	147
(TiVCrZrTa)N	crystalline (polycrystals)	148
$(AlCrMoTaTiZr)N_x$	solid solution	21
$(AlCrMnMoNiZr)N_x$	the same	149
$(AlCrMnMoNiZrB_{0.1})N_x$	"	139
(TiVCrZrAl)N	crystalline	150

Note. All coatings in the crystalline state and in the solid-solution state have fcc lattices.

IV. Properties of high-entropy alloys

IV.1. Mechanical properties

The properties of high-entropy alloys are governed by their structure and elemental composition. For instance, most high-entropy alloys with the bcc lattice exhibit high strength and low plasticity, whereas materials with the fcc lattice are characterized by low strength and high plasticity. As an example, Fig. 25 presents the plot of the hardness of $Al_xCoCrFeNi$ *vs.* aluminium concentration. As can be seen, phases with the fcc structure show low hardness (120 HV). As x changes from 0.4 to 0.9, the hardness abruptly increases. The maximum hardness was determined for the single-phase alloy with $x = 0.9$ and the bcc structure. It is believed that an increase in the proportion of the bcc phase is the main reason for an increase in the hardness. An increase in the surface area of interfaces favours a decrease in the mean free path of disclocations in the mixed region. It was assumed that a minor decrease in the hardness of the

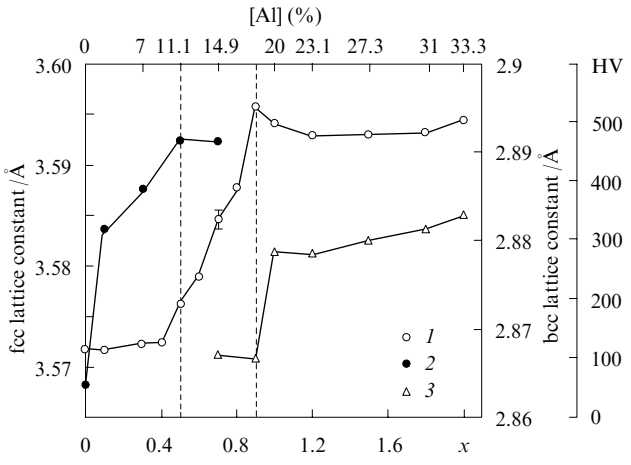


Figure 25. Hardness (*1*) and the bcc (*2*) and fcc (*3*) lattice constants of the alloy $Al_xCoCrFeNi$ plotted *vs.* aluminium content.[145]

alloys with $x = 1.0$ and subsequent increase in this property with increasing aluminium concentration are due to changes in the particle size in the spinodal structure formed. At $x = 1.8$ and 2, the alloy particles are smaller than other alloy particles; this is confirmed by a small increase in hardness. Nevertheless, the hardness of these alloys is relatively low (500 – 540 HV).

A high-entropy alloy $FeCoNiCrCuTiMoAlSiB_{0.5}$ exhibits high hardness and elastic modulus (11.3 and 187.1 GPa, respectively).[146] The hardness of the material decreased by only 12% after annealing at 900 °C.

Tensile properties of high-entropy alloys were studied.[37, 40, 147, 148] The mechanical properties of the high-entropy alloy AlCrCuNiFeCo improved after hot treatment (multiple forging) compared to those of the as-cast alloy at room temperature.[40] Typical stress – strain curves for this alloy obtained in the course of tensile tests at different temperatures are presented in Fig. 26. A brittle-to-ductile transition was observed in the temperature ranges from 700 to 800 °C for the as-cast alloy and from 600 to 700 °C for the forged sample. It should be noted that above the brittle-to-ductile transition temperature, deterioration of the tensile properties of the forged alloy is more pronounced than for the as-cast alloy. For instance, the yield stress decreases

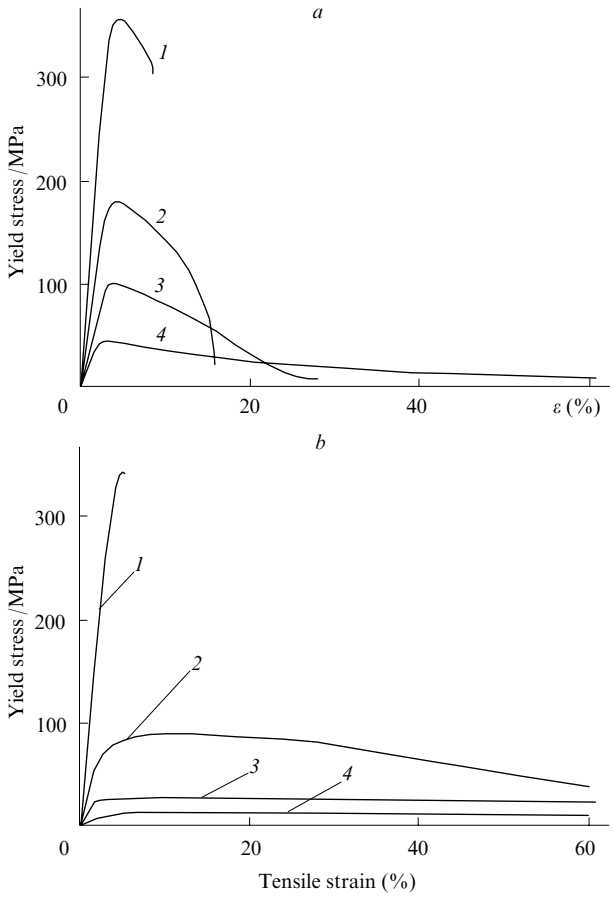


Figure 26. Typical stress – strain curves of the as-cast (*a*) and hot forged (*b*) samples of the high-entropy alloy AlCrCuNiFeCo deformed at different temperatures.[40]
(*a*) $T = 700$ (*1*), 800 (*2*), 900 (*3*), 1000 °C (*4*); (*b*) $T = 600$ (*1*), 700 (*2*), 800 (*3*), 900 °C (*4*); ε is the relative elongation.

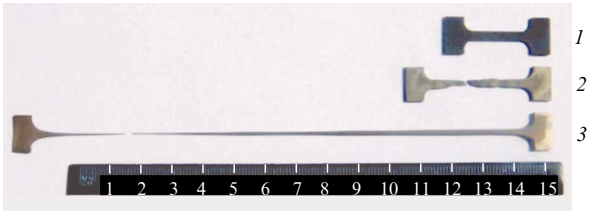


Figure 27. Photogaphs of tensile samples after deformation at 1000 °C.[40]
Non-deformed sample (*1*), as-cast sample ($\varepsilon = 77\%$) (*2*) and hot forged sample ($\varepsilon = 864\%$).

from 350 MPa at 700 °C to 180 MPa at 800 °C and to 44 MPa at 1000 °C. The strength of the forged alloy decreases more abruptly, namely, from 350 MPa at 600 °C to 91 MPa at 700 °C and 14 MPa at 1000 °C. It is noteworthy that for both states the brittle-to-ductile transition occurs at the same yield stress value (350 MPa).

The decrease in the yield stress of the alloy after high-temperature treatment is followed by transition to the superplastic state (Fig. 27). As can be seen, the as-cast alloy is characterized by a region of local deformation and fracture occurs at a small relative elongation. Deformation of the forged alloy occurs in a more smooth manner without formation of a bottleneck and at a larger relative elongation, which indicates its superplasticity.

Now we will consider the most interesting and curious, from out point of view, results of numerous studies on the mechanical properties of high-entropy alloys at different temperatures. Two alloys, CrMnFeCoNi and CrFeCoNi, were tensile tested in the temperature range from −196 to 1000 °C and exhibited high plasticity at room temperature.[147] Their plasticity and hardness increased as the temperature decreased, the yield strength being almost doubled and the relative elongation to fracture increased by a factor of 1.5% (up to 60%).

Improved room-temperature mechanical properties of the high-entropy alloy $AlCoCrFeNiTi_x$ were reported.[149] Taking into account a large atomic radius of titanium, this was explained by solid solution hardening. The best mechanical properties were exhibited by the alloy $AlCoCrFeNiTi_{0.5}$, *viz.*, a yield stress of 2.26 GPa, a fracture stress of 3.14 GPa and a plastic strain of 23.3% (Fig. 28).

Detailed low-temperature studies on the mechanical properties of high-entropy alloys are available.[45, 150] The alloy AlCoCrFeNi possesses excellent mechanical properties both at room temperature and at cryogenic temperatures.[150] The yield strength and the fracture strength increased by 29.7% and 19.9%, respectively, as the temperature decreased from 298 to 77 K. Improvement of these properties was explained by the single-phase bcc structure of the solid solution. In this case, each atom is considered as being 'dissolved' in the crystal lattice. Interaction between the 'dissolved' atoms causes distortion of the crystal lattice and formation of local elastic stress fields. The solid solution hardening is thus reduced to the interaction of the elastic stress fields of dislocations with corresponding fields of 'dissolved' atoms that impedes the motion of atoms and dislocations. The energy barrier thus produced can be overcome by raising the temperature even if external stress

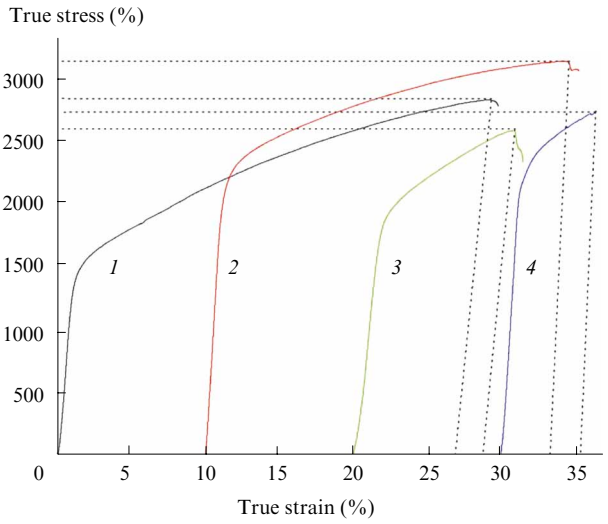


Figure 28. True stress–strain‡ curves for the high-entropy alloy $AlCoCrFeNiTi_x$.[149]
$x = 0$ (*1*), 0.5 (*2*), 1.0 (*3*), 1.5 (*4*).

is too low. The probability for dislocations to overcome the obstacles (P) is given by: [203]

$$P \propto \left(-\frac{Q - V\tau^*}{kT}\right)$$

where Q is the energy barrier, V is the activation volume and τ^* is the effective stress needed to be exerted to move the dislocations through the obstacle.

Clearly, as the temperature decreases to 77 K, the energy barrier increases, thus precluding the motion of dislocations. Therefore, the properties of the high-entropy alloy AlCoCrFeNi at ultralow temperatures are much better than at room temperature. However, we believe that further studies on the nature of these obstacles and their distribution in alloys of different elemental compositions are required.

Very high fatigue properties of the high-entropy alloy $Al_{0.5}CoCrCuFeNi$ (fatigue endurance limit varied from 540 to 945 MPa and the fatigue endurance limit to ultimate tensile strength ratio varied from 0.402 to 0.703) were compared with those of conventional alloys, *e.g.*, steel, alloys based on Ni, Cu, Mg and bulk metallic glasses.[151] The fatigue curves of the high-entropy alloy $Al_{0.5}CoCrCuFeNi$ and various conventional alloys, as well as the plots of the fatigue endurance limit and fatigue ratio *vs.* ultimate tensile strength are shown in Figs 29 and 30. As can be seen, the high-entropy alloys possess excellent fatigue properties. First of all, this seems to be due to their amazing tensile properties [*e.g.*, the fatigue endurance limit increases linearly as the ultimate tensile strength increases (see Fig. 30 *a*)]. Thus, high-entropy alloys can be treated as promising materials for fatigue-dependent applications. Clearly,

‡ The true stress is determined by the ratio of the load to the true cross-section surface area of the sample. The true strain is determined by the ratio of the force applied at any point of the test area to the surface area of the sample. These parameters are determined using the surface area of the sample at a given instant rather than at zero time.

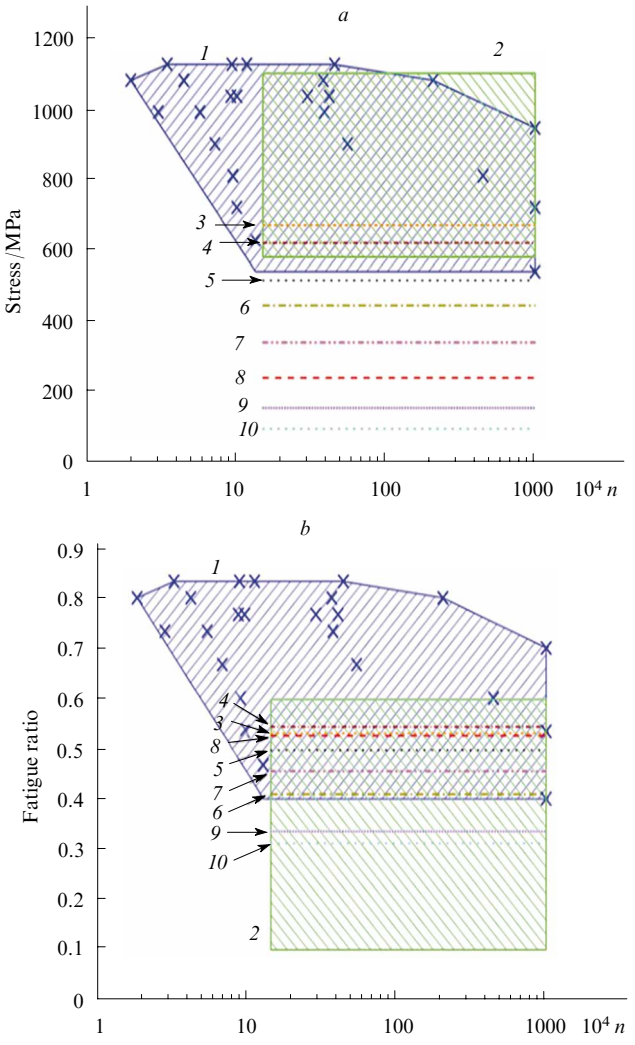


Figure 29. Fatigue curves of high-entropy alloy $Al_{0.5}CoCrCuFeNi$ and conventional alloys.[151]
(*a*) Endurance limit, (*b*) fatigue ratio; (*1*) high-entropy alloys, (*2*) bulk metallic glasses, (*3*) 4340 steel, (*4*) 15-5PH stainless steel, (*5*) Ti-6Al-4V, (*6*) Inconel 625, (*7*) 4340 steel annealed, (*8*) 1015 steel annealed, (*9*) zirconium alloy 702, (*10*) aluminium alloy 6061; n is the number of cycles to failure.

Figs 29 and 30 can be made more informative by further studying the high-entropy alloys of different elemental composition.

Mechanical properties of high-entropy alloys at elevated temperatures were studied.[46, 152] In particular, the properties of the alloy TaNbHfZrTi were studied in the temperature range from 296 to 1473 K.[46] Three temperature intervals with different deformation mechanisms were revealed:

— the range 296–873 K is characterized by temperature-independent strain hardening, deformation by twinning, appearance of a shear band (673–873 K), high yield strength (929 MPa) and strong strain hardening (3360 MPa);

— at 1073 K, tiny equiaxed grains are formed at the boundaries of deformed grains and no deformation by twinning occurs;

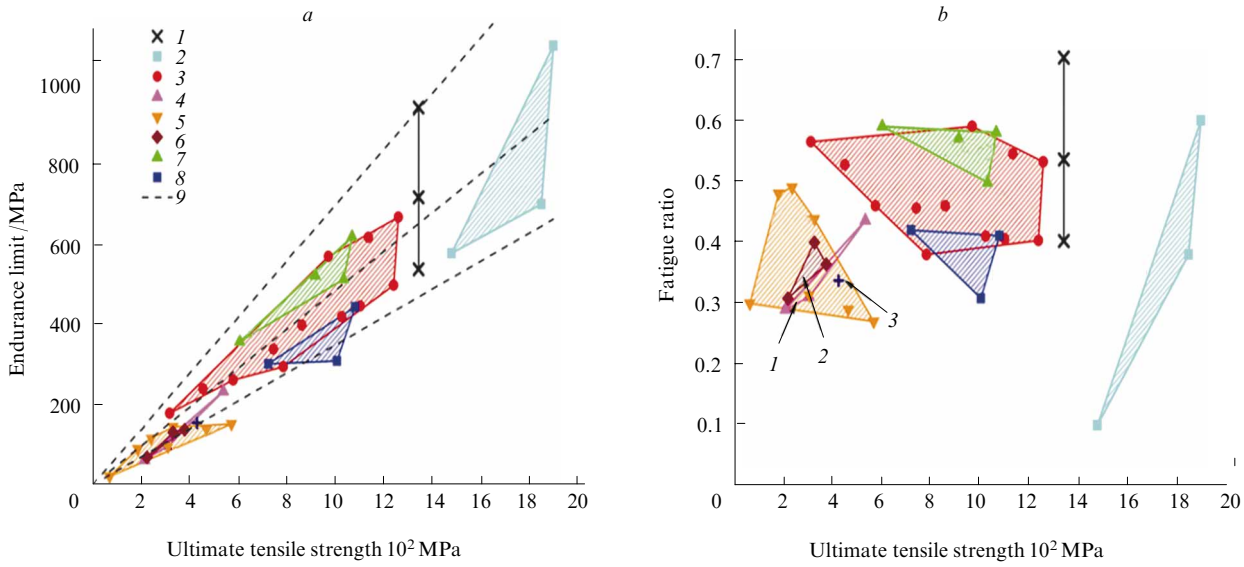


Figure 30. Endurance limit (*a*) and fatigue ratio (*b*) plotted *vs.* ultimate tensile strength for the high-entropy alloy $Al_{0.5}CoCrCuFeNi$ and various conventional alloys [151]:
(*a*) high-entropy alloys (*1*), Zr (*2*), steel (*3*), Cu (*4*), Al (*5*), Mg (*6*), Ti (*7*), Ni (*8*) and linear approximation (*9*).
(*b*) alloys based on Cu (*1*), Mg (*2*), Zr (*3*).

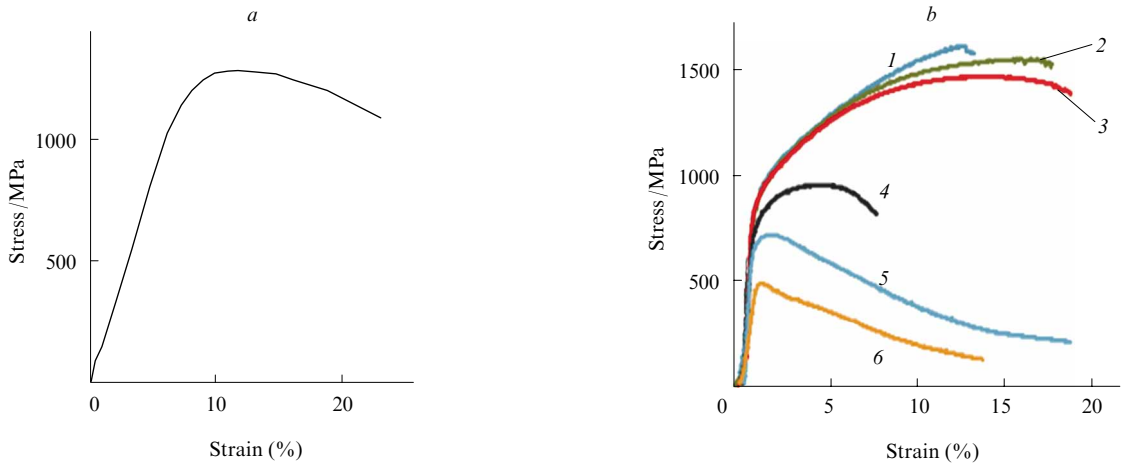


Figure 31. Stress–strain curves for the high-entropy alloy $V_{20}Nb_{20}Mo_{20}Ta_{20}W_{20}$ at different temperatures.[55]
(*a*) $T = 25$°C; (*b*) $T = 600$ (*1*), 800 (*2*), 1000 (*3*), 1200 (*4*), 1400 (*5*), 1600 °C (*6*).

— the range 1273–1473 K is characterized by abrupt decrease in the flow stress; no cracking is observed and deformation is accompanied by recrystallization.

High-entropy alloys based on high-melting elements deserved particular attention.[39, 46, 47, 55, 153]

An analysis of the stress–strain curves for the high-entropy alloy $V_{20}Nb_{20}Mo_{20}Ta_{20}W_{20}$ at different temperatures (Fig. 31) revealed a high room-temperature yield stress (1246 MPa) and a limited ductility (1.5%). In the temperature range from room temperature to 600 °C, the alloy undergoes a brittle-to-ductile transition accompanied by a decrease in the yield stress. As the temperature further increases, the yield stress decreases from 1246 to 477 MPa. In the temperature range 1400–1600 °C one deals with softening of the alloy. It is believed that high-temperature softening in the refractory high-entropy alloys is strongly impeded owing to slow diffusion of elements.

Summing up, studies of the mechanical properties of high-entropy alloys revealed a number of interesting effects, such as the brittle-to-ductile transition and superplasticity state, an increase in the tensile strength and yield stress at low temperatures, as well as high superplasticity, yield stress, ultimate tensile strength at room temperature, high specific strength at elevated temperatures and intriguing fatigue properties.

IV.2. Magnetic properties

Of particular interest are studies on the magnetic properties of high-entropy alloys.[30, 49, 60, 61, 65, 154] An investigation [65] of the dependence of the microstructure and magnetic

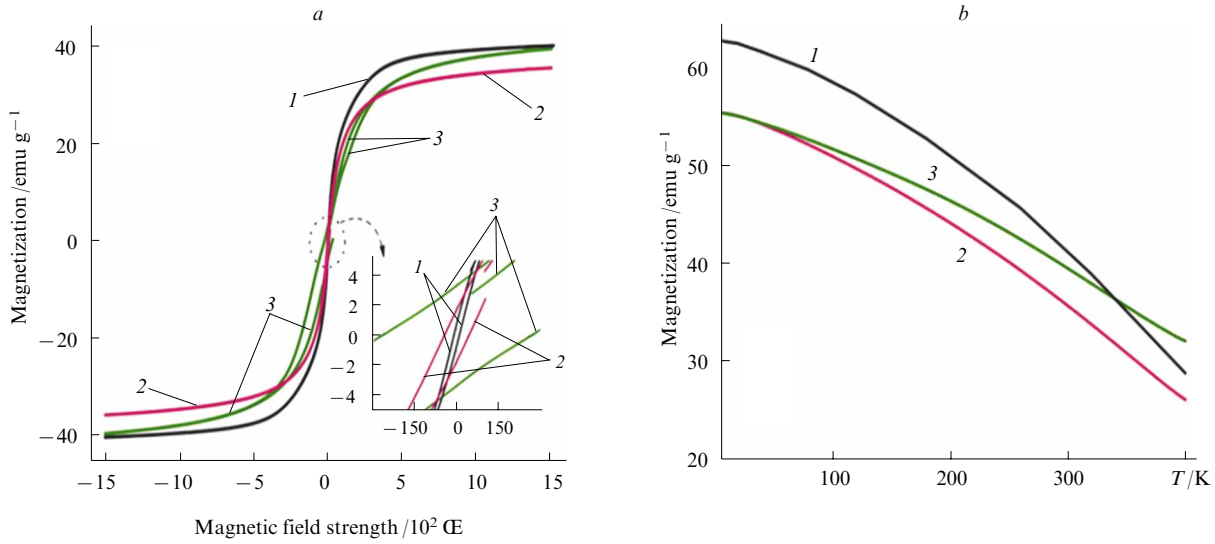


Figure 32. Magnetization of the high-entropy alloy AlCoCrCuFeNi plotted *vs*. magnetic field strength (*a*) and temperature (*b*).[61] (*1*) Quenched, (*2*) as-cast, (*3*) aged.

properties of the high-entropy alloys CoCrCuFeNiTi$_x$ on the titanium concentration showed that two alloys with the fcc structure, CoCrCuFeNi and CoCrCuFeNiTi$_{0.5}$, are typical paramagnets. As the titanium concentration increases, a transition to the superparamagnetic state occurs due to formation of amorphous phase containing nanoparticle inclusions.

The influence of the decomposition of phases formed on the magnetic properties of the high-entropy alloy AlCoCrCuFeNi was investigated.[61] The magnetic properties (magnetization) of the alloy after thermal ageing appeared to be better than those of the same as-cast alloy (Fig. 32). It should be emphasized that the samples exhibit the properties of ferromagnets. It is believed that thermal ageing causes improvement of magnetic properties due to the decomposition of the Cr–Fe domain into ferromagnetic (Fe–Co) and antiferromagnetic (Cr) subdomains. Cooling by sputtering was followed by the appearance of the magnetic properties typical of soft magnetic materials. At room temperature, the magnetization of the alloy was maximum and abruptly decreased with increasing temperature.

The saturation magnetization (M_s) of an alloy FeCoNi(AlSi)$_x$ first of all depends on the chemical composition of the alloy and monotonically decreases as x increases (Fig. 33).[60] The saturation magnetization of FeCoNi(AlSi)$_x$ is higher than that of the alloy Al$_x$CoCrFeNi (1.151 T *vs*. 0.106 T, respectively),[49] which makes the former alloy more promising for application as soft magnetic material. According to published data,[60] the low saturation magnetization of Al$_x$CoCrFeNi is due to the presence of chromium atoms whose magnetic moments are antiparallel to those of other elements and to the bcc type of the crystal lattice. High-entropy alloys with the fcc lattice are characterized by high M_s in contrast to the alloys with the bcc lattice. This feature originates from the higher density of atomic packing in the fcc lattice and from the high content of ferromagnetic elements (Fe, Co, Ni).

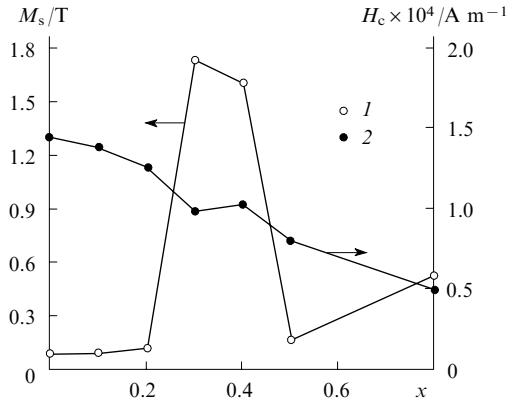


Figure 33. Saturation magnetization (*1*) and coercivity (*2*) of the high-temperature alloy FeCoNi(AlSi)$_x$ plotted *vs*. concentration.[60]

IV.3. Corrosion properties

The possibility of variation of the constituent elements and the ability to form amorphous phase are key advantages of high-entropy alloys that allow them to possess good mechanical and electrochemical properties. Clearly, high corrosion resistance of high-entropy alloys can be achieved by appropriately choosing the chemical composition.[62, 64, 155–161] The corrosion properties of the alloy Cu$_{0.5}$NiAlCoCrFeSi were thoroughly compared with those of 304 AISI stainless steel.[62, 161]

The electrochemical properties determined in different media are listed in Table 3. As can be seen, in NaCl and H_2SO_4 the room-temperature corrosion resistance of the alloy Cu$_{0.5}$NiAlCoCrFeSi is higher than that of stainless steel. This is first of all indicated by lower corrosion rate which is determined using the corrosion current density, ion valences, density of alloys, *etc*. It is clear that better corrosion properties can be achieved if the high-entropy alloy contains almost no grain boundaries and is in nearly-amorphous state. However, the alloy Cu$_{0.5}$NiAlCoCrFeSi

Table 3. Electrochemical properties of the high-entropy alloy $Cu_{0.5}NiAlCoCrFeSi$ and stainless steel in deaerated NaCl and H_2SO_4 solutions at room temperature.[62]

Parameter	High-entropy alloys		304 AISI stainless steel	
Deaerated NaCl solution				
Concentration /mol litre^{-1}	0.1	1	0.1	1
U_{cor} /V (see [a])	0.01	−0.53	−0.25	−0.59
U_d /V (see [a])	0.58	−0.25	0.46	0.17
ΔU_{pas} /V	0.45	0.16	0.71	0.62
i_{cor} /μA cm^{-2}	0.178	3.16	1.59	4.37
r_{cor} /mm year^{-1}	0.0013	0.0239	0.0165	0.0454
Deaerated H_2SO_4 solution				
Concentration /mol litre^{-1}	0.1	1	0.1	1
U_{cor} /V (see [a])	−0.06	−0.17	−0.05	−0.22
U_d /V (see [a])	0.11	0.09	1.12	1.06
ΔU_{pas} /V	0.12	–	1.13	0.90
i_{cor} /μA cm^{-2}	10.7	251	50.1	501
r_{cor} /mm year^{-1}	0.0810	1.8996	0.5209	5.2093

Note. Notations are as follows: U_{cor} is the corrosion potential, U_d is the degradation potential, ΔU_{pas} is the passivation potential, i_{cor} is the corrosion current density and r_{cor} is the corrosion rate.
[a] Measured *vs.* s.c.e.

exhibits a trend to degradation of certain surface regions and pitting due to a narrower potential range in the passive region and lower pitting-formation potential in the case of degradation of a passive film. A comparison of the degradation potentials (see Table 3) showed that dissolution of passive films is more pronounced for the high-entropy alloys in the acid medium.

Yet another study [161] was focused on the electrochemical behaviour of the alloy $Cu_{0.5}NiAlCoCrFeSi$ at elevated temperatures. It was shown that the corrosion resistance of the samples decreases with increasing temperature, the decrease being more pronounced in 1 M H_2SO_4 solution than in 1 M NaCl solution. It should be noted that the high-entropy alloy is characterized by higher corrosion resistance than the 304 AISI stainless steel in the acid medium in the whole temperature range, but the lack of the passive film leads to more intense corrosion. In 1 M NaCl solution, the high-entropy alloys are less corrosion resistant than the 304 AISI stainless steel at elevated temperatures owing to lower activation energy.

A study [160] on the dependence of the corrosion behaviour of the high-entropy alloy CuCrFeNiMn on the concentrations of constituent elements deserves particular attention. It was found that high corrosion resistance of this high-entropy alloy is mainly due to the copper concentration, degree of copper segregation and the structure of the alloy. The best corrosion properties of the alloy $CuCr_2Fe_2Ni_2Mn_2$ are due to the low concentration of copper. The poorest corrosion properties were determined for the alloy $Cu_2CrFe_2NiMn_2$. The negative influence of copper was explained by the tendency of this element to form the fcc structure which leads to a a decrease in the corrosion resistance.

IV.4. Thermal stability

Annealing significantly influences the microstructure and properties of high-entropy alloys.[41, 51, 100, 101, 162–171] A study on the evolution of the structure of the high-entropy alloy $Al_{0.5}CoCrCuFeNi$ after annealing at 700, 900 and 1100 °C over a period of 1.5 and 20 days, respectively, is available.[165]

As the duration of annealing at 700 °C increases, the microstructure gradually changes from extended dendrites to poly-grained structure (Fig. 34). The results of phase analysis suggested the possibility of formation of an intermetallic (σ-phase) that may correspond to the rod-like precipitates denoted by arrows in Fig. 34 *a–c*. A more detailed analysis showed that these precipitates may represent solid solutions based on CrFe and CoCr. As the temperature increases to 900 °C, the structure becomes fine-grained and no rod-like precipitates or elongated dendrites are observed. Annealing at 1100 °C led to formation of a phase composition similar to that of the as-cast samples; the annealed sample had the fine-grained structure only.

Phase diagrams belong to the most efficient tools for the determination of the phase stability of a state. Stability of the phases formed in the high-entropy alloy $Al_{0.5}CoCrCuFeNi$ after annealing was assessed [165] using the results of thermodynamic calculations (Table 4). It was assumed that at corresponding temperature, the phases formed after annealing are equilibrium ones. This assumption is based on the following facts: first, the existence of equilibrium phases in particular temperature ranges (this agrees with experimental results); second, annealing of high-entropy alloys is equivalent to quenching of conventional alloys. Owing to slow diffusion in the high-entropy alloys, cooling occurs rapidly, which prevents the phase transformation from being completed with the formation of new phases.

High softening resistance of the alloy $CoCrFeNiTiAl_x$ was demonstrated in a study on the influence of high-temperature annealing on its microstructure and properties.[164] The Vickers hardness of the annealed samples appeared to be higher than that of the as-cast samples. The hardness of the as-cast and annealed samples of the

Table 4. Phase compositions in the high-entropy alloy $Al_{0.5}CoCrCuFeNi$ observed in the experiments and obtained from thermodynamic calculations.[165]

T /°C	Experiment	Thermodynamic calculations
~1300–1400	Liquid	Liquid
1100–~1300	fcc + ordered fcc	fcc1 + fcc2 + ordered fcc
~800–1100	fcc + ordered fcc + ordered bcc	fcc1 + fcc2 + bcc + ordered bcc
300–~800	fcc + ordered fcc + ordered bcc + σ	fcc1 + fcc2 + bcc + ordered bcc + σ
0–300	fcc + ordered fcc + ordered bcc + bcc	fcc1 + fcc2 + ordered bcc + bcc

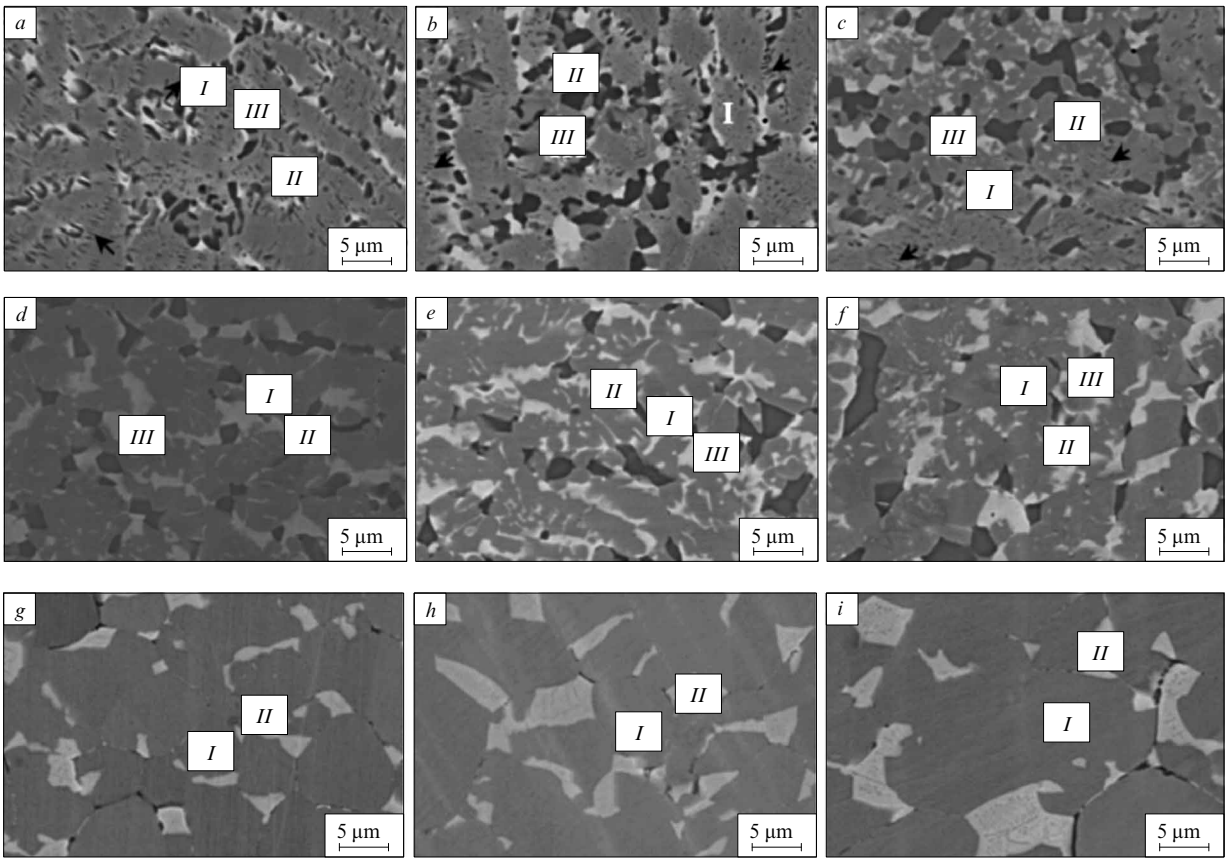


Figure 34. Photomicrographs of the high-entropy alloy $Al_{0.5}CoCrCuFeNi$ after thermal annealing.[165]
(*I* – *III*) Regions with the most pronounced chemical composition differences.
Annealing parameters:

Fig.	*a*	*b*	*c*	*d*	*e*	*f*	*g*	*h*	*i*
T/°C	700	700	700	900	900	900	1100	1100	1100
τ/days	1	5	20	1	5	20	1	5	20

alloy $CoCrFeNiTiAl_x$ are plotted *vs.* aluminium concentration in Fig. 35. As can be seen, the samples with $x = 1.0$ are characterized by a maximum hardness of 720 and 740 HV, respectively. The increase in hardness was explained by the formation of intermetallics with higher hardness than conventional alloys and by manifestation of the effect of solid-solution hardening.

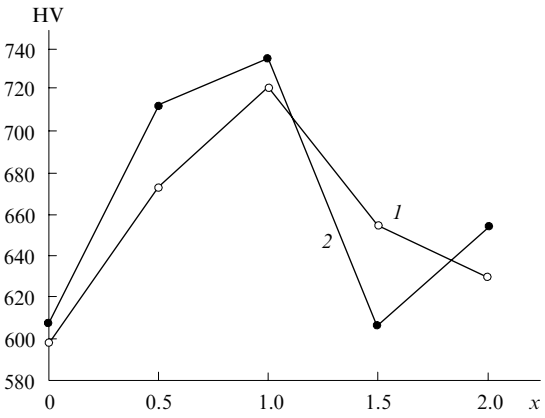


Figure 35. Vickers hardness of the as-cast (*1*) and annealed (*2*) samples of the high-entropy alloy $CoCrFeNiTiAl_x$ plotted *vs.* concentration of aluminium.[164]

The stress – strain curves exhibit very high room-temperature compressive stress values (2.6 GPa) for the annealed sample at $x = 0.5$ and superplasticity (13%). Further increase in the aluminium concentration leads to abrupt decrease in compressive stress (down to 1.5 GPa) and superplasticity, *i.e.*,. high aluminium concentration has an adverse effect on the strength properties.

V. Properties of nitride coatings based on high-entropy alloys

V.1. Mechanical properties

An analysis of published data showed that the hardness of the nitride coatings based on multicomponent alloys mainly depends on the number of nitride-forming elements on the deposition conditions. Low hardness obtained in studies[84,98] on the strength properties of the nitride coatings (FeCoNiCrCuAlMn)N, $(FeCoNiCrCuAl_2)N$ and (SiNiCrTiAl)N is probably due to the inclusion of elements that form no nitrides. The hardness values of the nitride coatings based on multicomponent alloys are listed in Table 5.

Table 5. Maximum hardness of the nitride coatings based on multicomponent alloys.

Nitride coating	Maximum hardness /GPa	Ref.
(FeCoNiCrCuAlMn)N	12	172
(FeCoNiCrCuAl$_{0.5}$)N	10	172
(SiNiCrTiAl)N	15	129
(AlCrNbSiTiV)N	41	128
(AlCrTaTiZr)N	35	18
(TiVCrZrHf)N	48	132
(AlCrMoSiTi)N	33	27
(AlMoNbSiTaTiVZr)N	37	20
(TiAlCrSiV)N	31	134
(TiVCrZrY)N	18	173
(TiAlCrZrNb)N	36	38

Mechanical properties of the coating (AlCrNbSiTiV)N composed of six nitride-forming elements were studied as function of nitrogen concentration in the mixture of inert gases.[128] The results obtained are shown in Fig. 36. As can be seen, the Young modulus and hardness of the metallic alloy (AlCrNbSiTiV)N_x ($x = 0$) deposited at $R_N = 0$ are 177 and 10.4 GPa, respectively. Hardness of these metallic films is due to the presence of amorphous phase which contains no disclocations for slip and to significant lattice distortion due to the presence of elements with different atomic radii. An increase in the nitrogen concentration leads to significant improvement of the strength properties of the coating, first of all, due to the formation of nitrides. As R_N further increases, the hardness increases from 35 to 41 GPa and the Young modulus increases from 300 to 360 GPa. It is believed that deterioration of the mechanical properties at $R_N = 40\%$ is due to too high ratios between nitrogen and metals [204] and to the possibility to obtain a high density of defects and even porous structure.

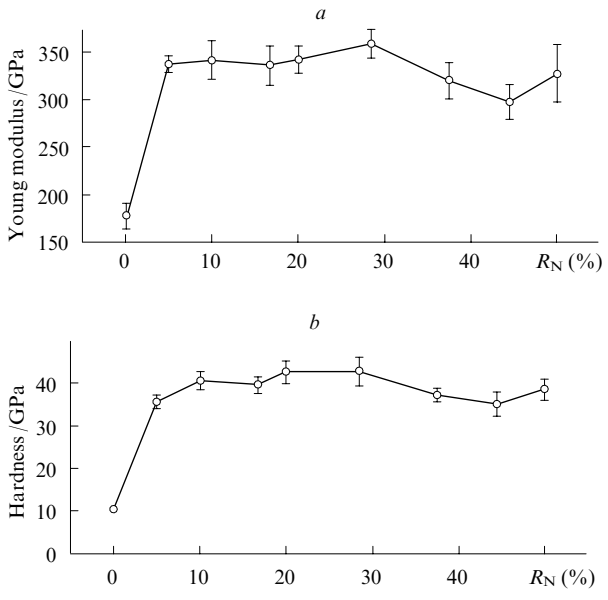


Figure 36. Young modulus (*a*) and hardness (*b*) of the nitride coatings (AlCrNbSiTiV)N_x deposited at different nitrogen flow rates plotted vs. R_N.[128]

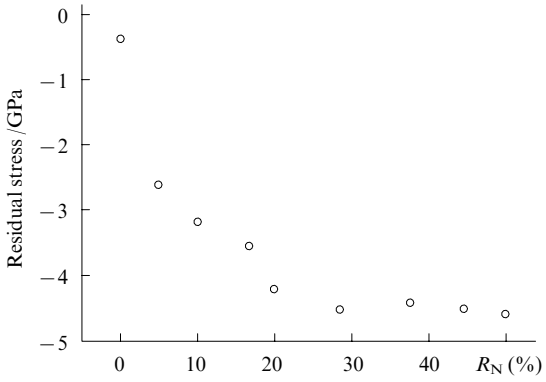


Figure 37. Residual stress of nitride coatings (AlCrNbSiTiV)N_x deposited at different nitrogen flow rates.[128]

Changes in the residual stress as function of parameter R_N are shown in Fig. 37. As the nitrogen concentration in the mixture of inert gases increases, compressive stress takes a constant value (4.5 GPa in absolute value). The appearance of compressive residual stress during thin-film deposition is due to internal stress produced as a result of lattice-constant mismatch between the substrate and coating and owing to ion bombardment. Since high residual stress favours separation of the coating from the substrate, we believe that optimum coatings are deposited at $R_N = 10\%$ and have a hardness of 40 GPa and a residual stress of 3.2 GPa.

Mechanical properties of nitride coatings based on multicomponent alloys prepared by physical vapour deposition using an electric arc were studied.[38, 42] The coatings (TiAlCrZrNb)N exhibited high hardness (H) which varied from 26.1 to 36.6 GPa as the negative substrate bias potential increased from −80 to −120 V. As the bias potential changed to −160 V, the hardness of the coatings decreased owing to relaxation of internal stress produced by increase in temperature caused by increase in energy of ions being deposited. These coatings were characterized by high wear resistance coefficients (up to 5.45). Parameters needed for estimating the plasticity index (H/E, where E is the Young modulus) and the plastic resistance (H^3/E^2) were calculated. It was shown that these parameters correlate with the wear resistance coefficient.

The influence of variation of the parameter R_N on the tribological properties of nitride coatings was studied taking the coating (AlCrMoTaTiZr)N_x as an example.[21] Changes in the friction coefficient of the coating deposited on cemented carbide substrates at $R_N = 40\%$ and 50% are illustrated in Fig. 38. After running-in period (sliding distance 3–5 m), the friction coefficient rapidly reaches a steady value equal to 0.74 ($R_N = 40\%$) or 0.80 ($R_N = 40\%$). Similar results were also obtained for the coating (AlCrTaTiZr)N.[174] After wear test at $R_N = 40\%$ and 50%, the wear rate of the coatings was 2.8×10^{-6} and 2.9×10^{-6} mm^3 N^{-1} m^{-1}, respectively. Taking into

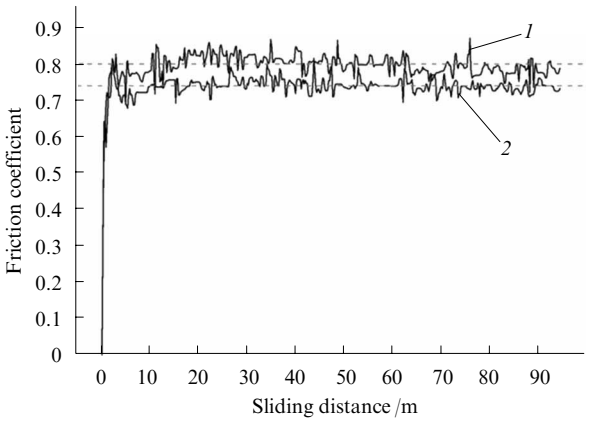


Figure 38. Friction coefficient of the (AlCrMoTaTiZr)N_x nitride coating deposited on cemented carbide substrates plotted *vs.* sliding distance at R_N = 40% (*1*) and 50% (*2*).[21]

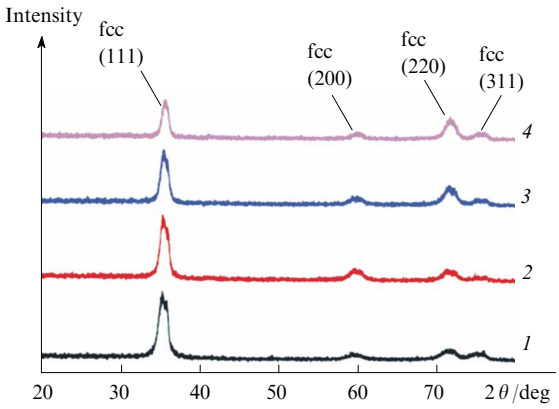


Figure 39. X-ray diffraction patterns of the (TiVCrZrHf)N coating after annealing *in vacuo* at different temperatures.[175]
As-deposited (*1*); T_{ann} = 973 (*2*), 1073 (*3*) and 1173 K (*4*).

account published data for other coatings[140] [wear rate in the range $(3.7-6.5)\times10^{-6}$ mm^3 N^{-1} m^{-1}], the coating (AlCrMoTaTiZr)N_x exhibits high wear resistance due to the presence of molybdenum which reduces the friction coefficient and the wear degree.

Unfortunately, no published data on the superhard properties of nitride high-entropy alloys, similar to those of, *e.g.*, $(Ti_{1-x}Al_x)N$ and TiN/Si_3N_4, are available at the moment. It should be noted that studies on the nitride coatings based on high-entropy alloys are limited to the search for new multicomponent systems and investigation of the influence of the preparation and treatment conditions on their properties. We believe it seems appropriate to use a traditional ion implantation technique as well as multilayer and combined coatings in order to modifiy the mechanical and tribological properties.[205, 206]

V.2. Influence of annealing on the microstructure and properties of nitride coatings based on multicomponent alloys

The resistance and thermal stability of the structure of materials during high-temperature annealing make it possible to predict their properties at high temperatures.

Publications[43, 175–178] are devoted to investigations of changes in the microstructure and physicomechanical properties of multi-element nitride coatings upon high-temperature annealing. In particular, the evolution of the structure and properties of the nitride coating (TiVCrZrHf)N prepared by r.f. magnetron sputtering upon annealing *in vacuo* and in air was studied.[175, 176] The X-ray diffraction patterns of the coating obtained under vacuum annealing at different temperatures are shown in Fig. 39. As can be seen, the coating has a fcc structure with randomly distributed Ti, V, Cr, Zr and Hf atoms. The formation of stable solid solution from all constituent nitrides is confirmed by the influence of the high entropy of mixing on the formation of the simple

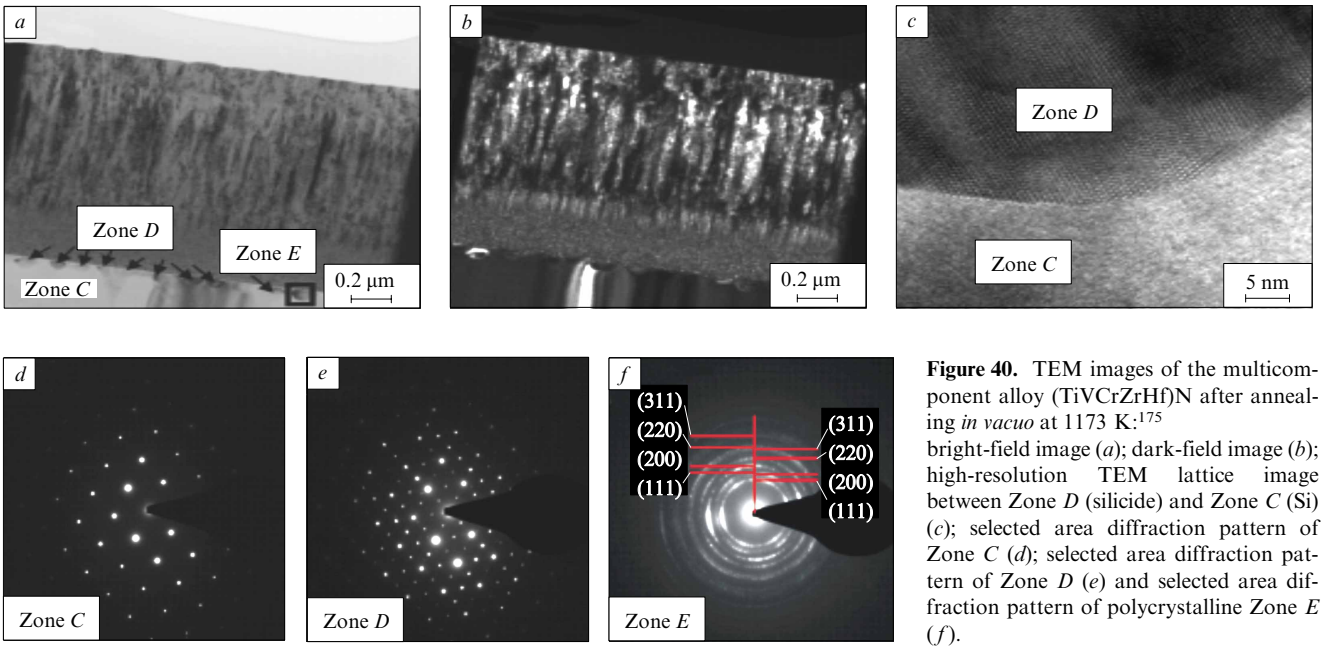


Figure 40. TEM images of the multicomponent alloy (TiVCrZrHf)N after annealing *in vacuo* at 1173 K:[175]
bright-field image (*a*); dark-field image (*b*); high-resolution TEM lattice image between Zone *D* (silicide) and Zone *C* (Si) (*c*); selected area diffraction pattern of Zone *C* (*d*); selected area diffraction pattern of Zone *D* (*e*) and selected area diffraction pattern of polycrystalline Zone *E* (*f*).

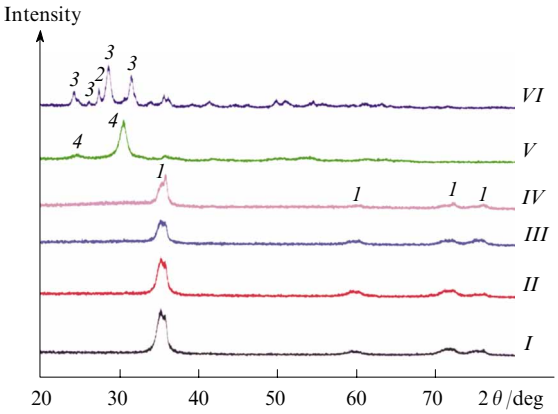


Figure 41. X-ray diffraction patterns of the (TiVCrZrHf)N coating annealed in air at different temperatures.[176]
(*1*) fcc structure, (*2*) TiO_2, (*3*) ZrO_2, (*4*) $ZrTiO_4$; (*I*) as-deposited; T_{ann} = 300 (*II*), 400 (*III*), 500 (*IV*), 600 (*V*) and 700 °C (*VI*).

crystal lattice. The solid solution with the fcc structure is thermodynamically stable and does not decompose even in the course of annealing at 1173 K for 2 h. A slight decrease in the lattice constant is probably due to removal of the point defects that appeared during sputtering. The size of the crystal increased from 7.4 to 12.8 nm.

The mechanism that precludes coarsening of grains on high-temperature annealing was described in detail elsewhere.[177] Mention was made that stability of the structure and grain size is due to low energy of grain boundaries (no grain coarsening occurs) and sluggish diffusion. Severe lattice distortion is accompanied by a considerable increase in the free energy, a decrease in the energy of grain boundaries and, therefore, the driving force of grain coarsening. High packing density causes the effective diffusion paths to shorten and thus the grain growth slows down. No visible changes in the microstructure were obseved in the course of annealing at 1073 K. However, raising the temperature to 1173 K was followed by precipitation of $CrSi_3$ with diamond-like structure. Interdiffusion of chromium and silicon atoms maintained the mechanical and electrical properties of the coating almost unchanged.

The TEM images of the multicomponent alloy (TiVCrZrHf)N after annealing at 1173 K *in vacuo* are shown in Fig. 40. At 1173 K, amorphous solid is transformed to a polycrystalline solid (Zone *E*). It should be noted that the diffraction Zone *E* corresponds to the presence of two fcc phases that can dissolve at much higher temperature. A wide variety of crystalline precipitates at the substrate/coating interface was also observed. According to energy-dispersive X-ray spectroscopy data, these precipitates contained chromium and silicon in a 3 : 1 ratio. The interfacial layer probably contained a metastable phase, the silicide $CrSi_3$. The formation of this layer is probably due to the difference between the enthalpies of formation of the nitrides and silicides of the constituent elements.

The X-ray diffraction patterns of the nitride coating (TiVCrZrHf)N obtained after annealing in air are presented in Fig. 41. No oxides were observed even on annealing at 500 °C. However, at 600 °C, the coatings undergo complete oxidation and peaks corresponding to the hexagonal $ZrTiO_4$ appear.§ Further heating to 700 °C led to decomposition of $ZrTiO_4$ to monoclinic zirconia and titania with rutile structure. The formation of these phases was associated with different tendencies of each element to form an

§ We believe that identification of the lattice type in Ref. 176 is incorrect, namely, the bcc structure should be instead of the fcc structure. Also, peaks appeared at 600 °C correspond to tetragonal rather than hexagonal phase of $ZrTiO_4$.

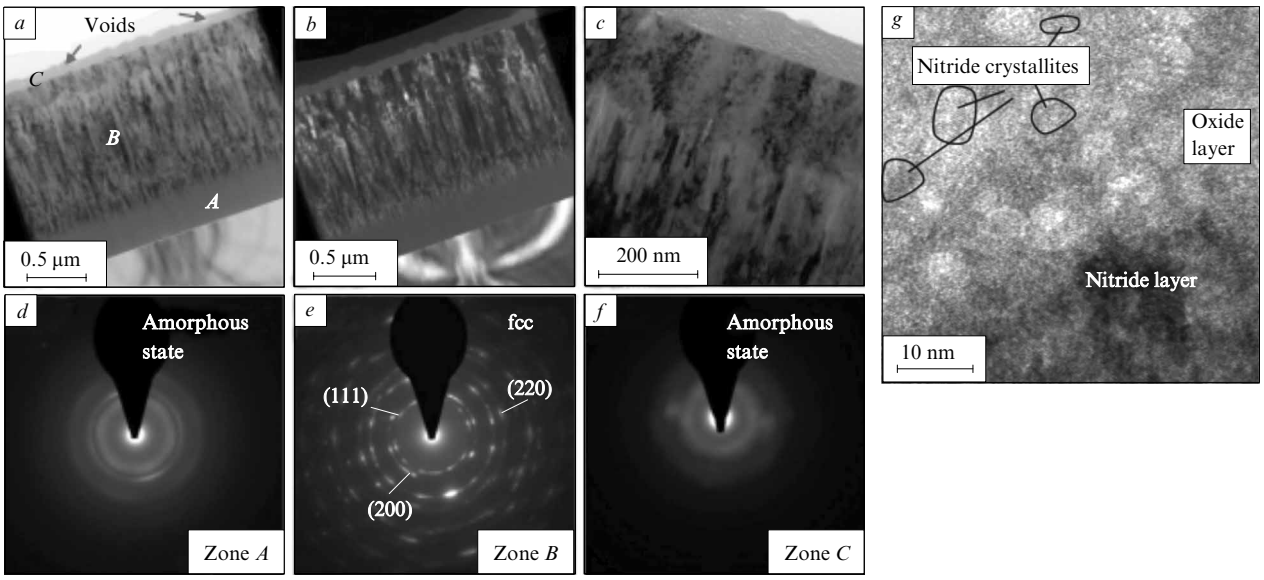


Figure 42. Cross-sectional TEM images of the (TiVCrZrHf)N coating annealed at 400 °C in air.[176]
Bright-field image (*a*), dark-field image (*b*), higher-magnification TEM image (*c*), selected-area electron diffraction pattern of Zone *A* (*d*), selected-area electron diffraction pattern of Zone *B* (*e*), selected-area electron diffraction pattern of Zone *C* (*f*) and high-resolution TEM image of the crystal lattice (*g*).

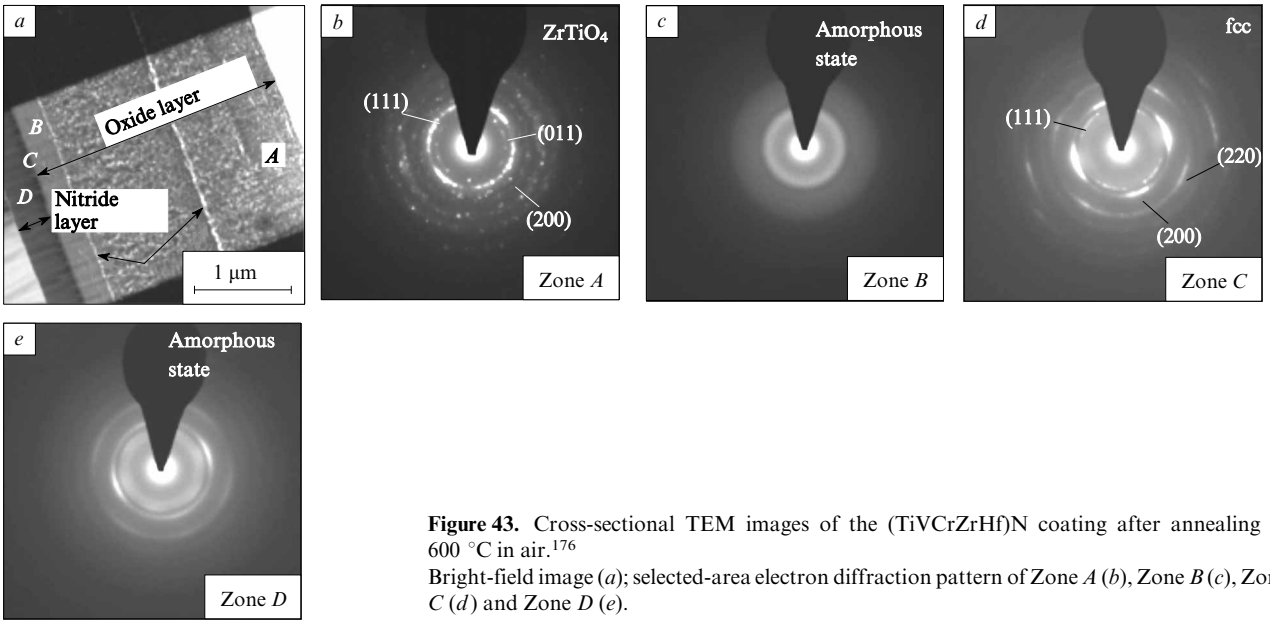


Figure 43. Cross-sectional TEM images of the (TiVCrZrHf)N coating after annealing at 600 °C in air.[176]
Bright-field image (*a*); selected-area electron diffraction pattern of Zone *A* (*b*), Zone *B* (*c*), Zone *C* (*d*) and Zone *D* (*e*).

oxide from nitride. Taking into account this fact, it is clear that TiN, ZrN and HfN exhibit a more pronounced tendency to oxidation.

The cross-sectional TEM images of the coating (TiVCrZrHf)N after annealing at 400 °C are shown in Fig. 42. The oxide layer nearly 95 nm thick with cavities and pores is formed on the surface of the coating. The results of X-ray diffraction analysis show that the oxide layer is an amorphous phase (see Fig. 42*f*). No other structural changes were observed. The formation of pores and voids in the oxide layer was explained by the 'release' of nitrogen and by large volume expansion in the course of oxidation. It is remarkable that the oxide layer adjacent to the nitride layer still contains some amount of nitride crystallites (see Fig. 42*g*). This was also observed for the coating (TiVCrZrHf)N after annealing at 500 °C (see Fig. 6*d* in Ref. 176), thus indicating that oxidation is diffusion controlled. Raising the annealing temperature causes the thickness and porosity of the oxide layer to increase due to not only volume expansion (see above), but also different thermal expansion coefficients of the oxide and nitride layers that are present near the substrate even after annealing at 600 °C (Fig. 43*a* and *d*).

X-Ray diffraction analysis of Zone *A* (Fig. 43*b*) revealed peaks from the (011), (111) and (200) planes, which indicate the formation of the oxide $ZrTiO_4$. This was confirmed by the results of an X-ray study of the crystal structure of the coating (see Fig. 41); however, the (111) plane remains the main growth direction of nitride crystallites.

Annealing at 700 °C leads to complete oxidation of the coating which becomes 3160 nm thick after annealing (see Fig. 3*f* in Ref. 176). The oxidative stability of (TiVCrZrHf)N decreases at an annealing temperature of 600 °C.

The hardness and Young modulus are plotted *vs.* annealing temperature in Fig. 44. At annealing temperatures below 300 °C, no changes in the mechanical properties of the samples were observed. At higher temperatures, the strength properties abruptly deteriorate. At 600 °C and above, the hardness reaches a minimum value of 2.5 GPa because of complete oxidation. Clearly, the adverse influence of oxidation is responsible for poorer mechanical properties of oxides compared to those of nitrides and for the presence of a thick oxide layer on the surface.

High thermal oxidative stability of the nitride coatings $(Al_{23.1}Cr_{30.8}Nb_{7.7}Si_{7.7}Ti_{30.7})_{50}N_{50}$ and $(Al_{29.1}Cr_{30.8}Nb_{11.2}Si_{7.7}Ti_{21.2})_{50}N_{50}$ annealed at 900 °C in air was reported.[178] The coatings were deposited at high bias potentials to make their structures more compact. The oxide films on the surface samples were 100 ± 12 and 80 ± 7 nm thick, respectively; this indicated high oxidative stability of the films. It is believed that high thermal oxidative stability is first of all due to the dense structure with no channels for oxygen transport.

The influence of the annealing temperature on the defect concentration profiles was studied taking the nitride coatings (TiZrHfVNb)N based on high-entropy alloys as examples.[43] The coatings prepared by vacuum arc deposition on a substrate at negative bias potentials ranging from -100 to -200 V and operating pressures of 0.7, 0.3, 0.1 and

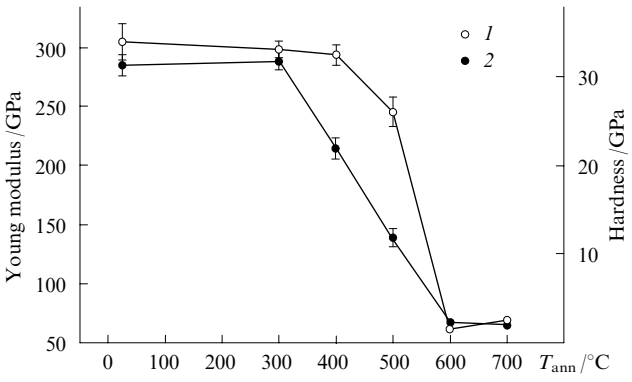


Figure 44. Hardness (*1*) and Young modulus (*2*) of the (TiVCrZrHf)N nitride coating after annealing at different temperatures in air.[176]

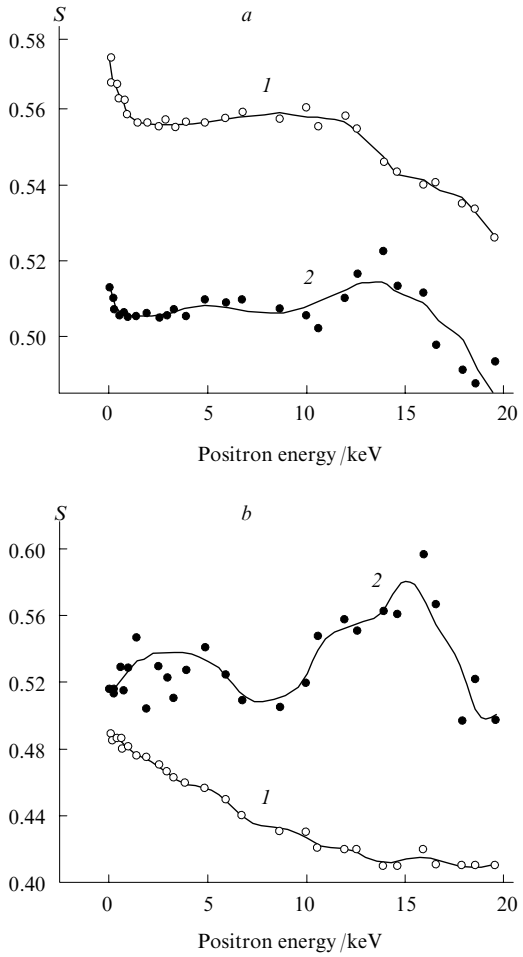


Figure 45. Profiles of the *S* parameter of Doppler broadening of the positron annihilation peak in depth of the (TiZrHfVNb)N coating upon deposition (*1*) and after annealing at 600 °C and 100 Pa (*2*).[43] (*a*) Bias potential is −200 V, operating pressure is 0.7 Pa; (*b*) bias potential is −100 V, operating pressure is 0.1 Pa.

4×10^{-2} Pa were annealed in a furnace at 600 °C and a pressure of the residual atmosphere of 100 Pa for 30 min. The results of the depth analysis of the elemental composition indicate (i) a decrease in the nitrogen concentration in the coating with decreasing gas pressure in the chamber and (ii) minor changes in the concentrations of the other elements.

Positron annihilation is the most efficient, sensitive and reliable method for studies of voids in nanocrystalline materials. Positron annihilation spectroscopy was used to determine the values of the parameter *S* characterizing the concentration of defects in the depth of the coating (Fig. 45). As can be seen the concentration profiles of defects depend strongly on the deposition conditions. For the first series of samples (no annealing, see Fig. 45 *a*), the parameter *S* mainly decreases, except minor oscillations at particular positron energy values. Another picture was observed for the second series of samples (see Fig. 45 *b*). Before annealing, the concentration of defects in the coating is minimum ($S \approx 0.49$). After annealing, the *S* value for the near-surface layer of the coating increases to 0.53 and even reaches a value of 0.59 as the depth of analysis increases. It is believed that the increase in the *S* value for the near-surface layer is related to formation of the oxide film, while the maximum *S* value is governed by spinodal segregation and formation of new phases at nanograin boundaries.

Note that grain growth in the course of annealing is the most evident mechanism of structural relaxation. Segregation of nitrogen at grain boundaries impedes the growth of nanocrystals. According to calculations,[43] the nanograin size for the first series of samples was 55–58 nm and was almost unchanged after annealing. Probably, a decrease in the parameter *S* value (see Fig. 45 *a*) can be related to annealing of vacancies.

Thus, we showed that migration of defects in the course of annealing impedes the growth nanocrystallites upon an increase in the annealing temperature and the possibility of changing the thermal stability by varying the deposition conditions.

VI. Influence of deposition conditions on the microstructure and properties of nitride coatings based on high-entropy alloys

VI.1. Changes in substrate temperature upon deposition

The formation of a coating is a multistep process which first of all depends on the energy of ions deposited from the vapour phase. Clearly, the substrate temperature should influence the ion mobility and the interaction between deposited ions which in turn govern the microstructure, stoichiometry and eventually the properties of the coating.

The results of a study on the influence of substrate temperature on the structure and mechanical properties of the nitride coating (TiVCrZrHf)N were reported.[132] The deposition was performed using the temperature varied in the range from 23 to 450 °C as monitoring parameter. It was shown that at 450 °C, the nitrogen concentration decreases to 40 at.%, probably due to acceleration of nitrogen desorption from the film surface. Taking into account higher mobility of atoms as the substrate temperature increases, grains should grow under these conditions. However, in that study the grain size abruptly decreased above 250 °C, probably, as a result of nitrogen desorption. Nitrogen deficiency in the system may lead to the appearance of defects and to lattice distortion, which in turn can impede grain growth. As the temperature further increased, the grain size also increased.

Studies on thermally induced changes in the microstructure first of all deal with diffusion. Clearly, intensification of these changes favours pore filling and, as a consequence, formation of a more smooth surface and densitication of the structure. A study of the mechanical properties revealed an extremely high hardness of the coating (48 GPa). So high value is due to the formation of a dense structure, namely, an increase in the volume fraction of interfaces (grain boundaries, triple junctions) where the motion of disclocations is impeded. Similar results were also obtained in studies of the nitride coatings (AlCrMoSiTi)N and (AlCrTaTiZr)N.[18, 27]

VI.2. Changes in substrate bias potential during deposition

The substrate bias potential is a parameter affecting the chemical composition, microstructure and properties of coatings.[207] For instance, changes in the structure and properties of the nitride coating (AlCrTaTiZr)N at different substrate bias potentials were studied.[174] Minor variations

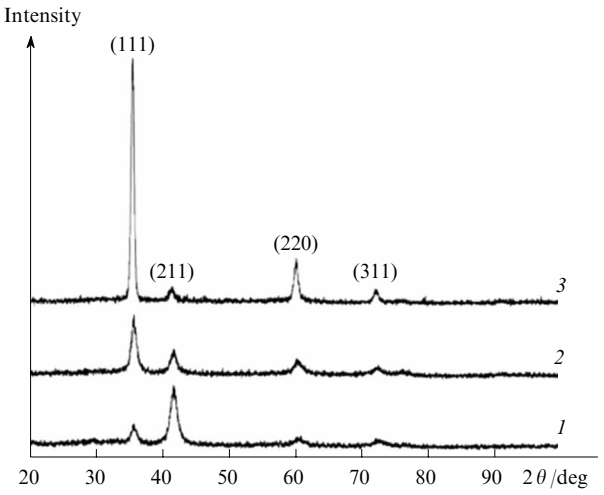


Figure 46. X-Ray diffraction patterns of the (AlCrTaTiZr)N coatings at substrate bias potentials of 0 (*1*), −50 (*2*) and −150 V (*3*).[174]

of the chemical composition with increasing the bias potential were explained by re-sputtering of lighter atoms (*e.g.*, nitrogen and aluminium).

The X-ray diffraction patterns of the coating at different bias potentials are presented in Fig. 46. All peaks correspond to the fcc lattice (NaCl structural type). The diffraction peaks undergo a shift towards smaller angles as the substrate bias potential increases in absolute value. The increase in the lattice constant is associated with replacement of aluminium atoms by elements having larger atomic radius. The X-ray diffracrions patterns clearly demonstrate the changes in the orientations of crystallographic planes [see the strong peak corresponding to the (111) plane] at the maximum bias potential. This orientation is realized through the lower surface and strain energies in the (111) plane. Using different substrate bias potentials, one can fill microscopic voids and form a dense columnar microstructure.

A study[27] on the mechanical properties of the nitride coating (AlCrMoSiTi)N showed that the maximum hardness of the material is achieved at a bias potential of −100 V (see Fig. 47 *a*). Although the coatings deposited at low bias potentials are characterized by lower compressive strain compared to the coatings prepared at high bias potentials, both groups of coatings exhibit the same hardness. This was explained by low compressive strain in large grains. Based on the values of the superplasticity index, these coatings seem to be candidates for operation under wear conditions.[208]

The influence of the substrate bias potential on corrosion of the nitride coating (AlCrSiTiZr)N was studied.[141] Table 6 lists the values of the main electrochemical parameters. At a bias potential of −100 V, the corrosion current density decreases to 3.0 μA cm^{-2} for aluminium alloy 6061 and to 3.1 μA cm^{-2} for mild steel. Therefore, the bias potential shows a beneficial action on the corrosion resistance of the alloy and mild steel compared to the that of the coatings deposited at 0 V and 304 AISI stainless steel. The changes in the electrochemical parameters were explained by densification of the structure under the action of the bias potential (radiation-induced densification).

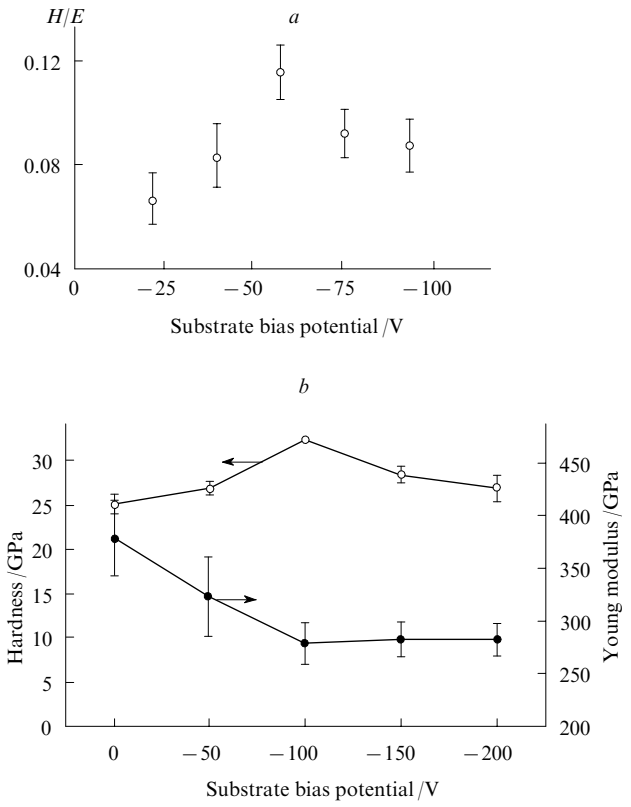


Figure 47. *H*/*E* ratio (*a*), hardness and Young modulus (*b*) of the (AlCrMoSiTi)N coating plotted *vs.* substrate bias potential.[27]

VII. Applications of high-entropy alloys and nitride coatings based on them

Unique properties of high-entropy alloys attract the attention from both fundamental research and practical point of view and there is considerable literature on the subject. In particular, high-entropy alloys can be used in nuclear power engineering because they have high radiation resistance,[179] as refractory materials (owing to high strength at elevated temperature and oxidative stability), as soft magnetic materials (possess superparamagnetic or ferromagnetic proper-

Table 6. Electrochemical parameters of the (AlCrSiTiZr)N coating deposited on different substrates at different bias potentials in 0.1 M H_2SO_4 solution.[141]

	Aluminium alloy 6061			Mild steel			304 stainless steel
	no coating	0 V	−100 V	no coating	0 V	−100 V	
i_{cor} /μA cm^{-2}	29.1	17.3	3.0	90.4	7.7	3.1	19.1
U_{cor} /mV	−424	−353	−336	−279	−367	−292	−116

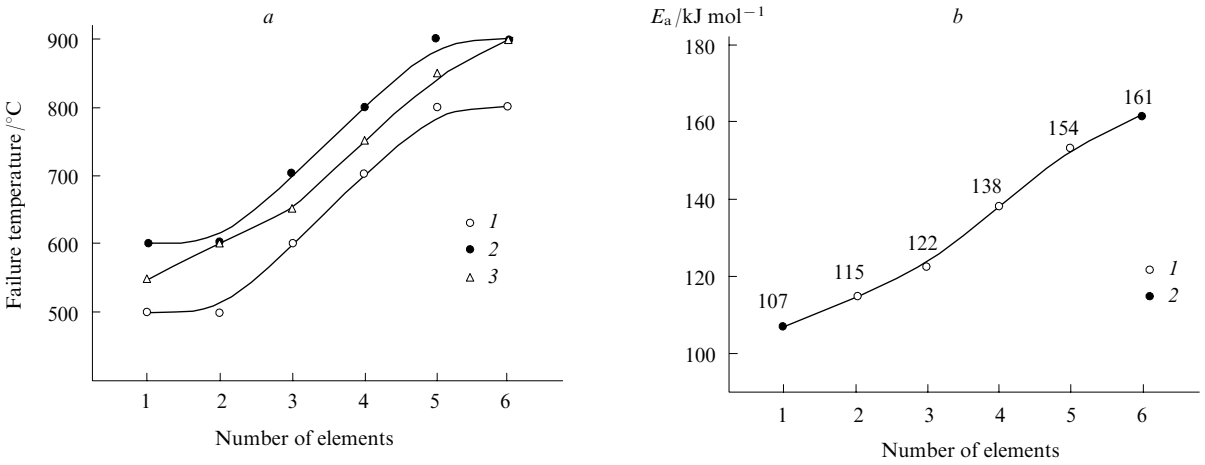


Figure 48. Failure temperature of diffusion barriers (*a*) and activation energy of copper diffusion in Si/diffusion barrier/Cu stacks (*b*) for nitrides plotted *vs*. number of metallic elements.[183]
(*a*) Barrier regions: (*1*) endurance, (*2*) complete failure, (*3*) failure; (*b*) interpolation (*1*), experiment (*2*); data for nitrides were interpolated between the endurance and complete failure temperatures.

ties), as materials for tool-making industry (have low friction coefficients, are wear resistant and possess optimum combination of the strength properties and superplasticity), as corrosion-resistant surface layers, fatigue-resistant materials, in aerospace industry (low density) and as materials for hydrogen storage.[118, 180]

Nitride coatings based on multicomponent alloys can also be used as diffusion barriers for metallization.[23, 131, 136, 137, 181 – 183] Of particular interest is a study [183] on the diffusion stability of multicomponent nitrides including TiN (1N), (TiTa)N (2N), (TiTaCr)N (3N), (TiTaCrZr)N (4N), (TiTaCrZrAl)N (5N) and (TiTaCrZrAlRu)N (6N) (figures in parentheses denote the number of metallic elements in the nitrides). The diffusion-resistant abilities of the materials at elevated temperatures were analyzed *vs*. number of constituent elements. All six nitride diffusion barriers were solid solutions with the same lattice type (fcc).

The failure temperatures of diffusion barriers and the activation energies of copper diffusion in the nitrides under study are plotted *vs*. number of metallic elements in Fig. 48. As can be seen, the six-element nitride (TiTaCrZrAlRu)N characterized by a failure temperature of 900 °C is the most stable, whereas conventional single-, two- or three-element nitrides have failure temperature in the range ~ 550 – 650 °C. These results were also confirmed by the values of the activation energies of copper diffusion, namely, the higher the activation energy the higher the diffusion-resistant ability. Improvement of the diffusion-resistant ability was explained by severe lattice distortion and dense microstructure, which is characteristic of the nitride coatings based on high-entropy alloys of any elemental composition.

Yet another promising field of application of nitride coatings based on high-entropy alloys is biomedicine. Protective coatings for biomedical applications should have a low elastic modulus, high chemical stability, wear resistance and corrosion resistance in physiological media, low friction coefficient, biocompatibility and excellent adhesion to surfaces onto which these coatings are deposited.

This is just the case for transition-metal nitrides and carbides which thus become of interest for biomedical applications. In particular, the structure and properties of the coatings (TiZrNbHfTa)N and (TiZrNbHfTa)C for biomedical applications were studied.[127] Corrosion resistance tests performed in simulated body fluid (SBF) solutions at room temperature made it possible to obtain the potentiodynamic polarization curves of the coatings and substrates and thus evaluate the corrosion resistance and porosity of the coatings and the efficiency of protection. Here, the corrosion resistance is understood in terms of the penetration rate of the solution into the coating. It was found that the corrosion resistance of the nitride coatings is much higher than that of carbide coatings, being doubled compared to that of the substrate. This is due to the fact that nitrides form more dense structures owing to strong chemical bonds and have lower porosity than carbides.

Biocompatibility tests of the coatings (see Fig. 8 in Ref. 127) showed that they do not induce any cytotoxic response by osteoblasts (24 and 72 h) and good morphology of the attached cells was observed. Cell viability analysis showed a very high ratio of living cells to dead cells, for all the investigated groups. This indicates biocompatibility of the nitride and carbide coatings based on high-entropy alloys.

VIII. Conclusion

In this review, we analyzed the mechanisms of structure formation and the physicomechanical properties of high-entropy alloys that in most cases represent single-phase solid solutions with bcc or fcc lattices. Dominant factors that govern the formation of nanocomposite or amorphous structures were considered. Unique physicochemical properties of high-entropy alloys (corrosion resistance, high thermal stability, wear resistance, high strength, *etc*.) extend the filed of applications of these systems.

Nitrogen-containing coatings based on high-entropy alloys are characterized by solid-solution hardening and lattice distortion, which improves the strength properties of the nitride coatings. We analyzed how the deposition

parameters influence the physicomechanical properties of the nitride coatings and outlined the regularities of structure formation at different temperatures and substrate bias potentials.

By varying the deposition parameters one can achieve extremely high strength values and form more densified structures of the nitride coatings based on high-entropy alloys, which will be corrosion resistant and biocompatible. It should be noted that the number of publications in this rapidly progressing field continuously increases; also, many new methods for the synthesis of high-entropy alloys and methods of investigations of these systems were developed (in particular, computer simulation and numerical calculations are used to predict new chemical compositions and properties of high-entropy alloys and nitrides based on them). Therefore, there are grounds to believe that research on high-entropy alloys will progress and novel alloys possessing good physicomechanical properties will be obtained.

Promising methods for preparation of high-entropy alloys include, *e.g.*, melting under exposure to low-energy electron beam [209] or high-current ion beam [210] powder coating, as well as surface modification using a heavy-current pulsed electron beam.[211 – 214] This method makes it possible to obtain a more uniform depth distribution of the elements, amorphous or nanocrystalline structure and is characterized by much higher efficiency (up to 50%) compared to laser cladding. Also, we believe that analysis of the structure and properties of the carbide [126] and oxide coatings [215] based on high-entropy alloys may appear to be of considerable interest. Pioneering studies in this investigation line are available, but systematic analysis of published data is a matter for the future.

Of particular importance is the concept of the evolution of nitride coatings based on high-entropy alloys in the form of coatings composed of disclocation-free nanocrystals separated by a layer of amorphous phase. As shown earlier,[216 – 222] a nanocomposite composed of amorphous nitride matrix with nanocrystalline inclusions possesses superhardness. Also, it seems appropriate to investigate high-entropy alloys for applicability in multilayer coatings based on alternating transition-metal nitride layers [216] or corresponding nitrides.[222 – 229] A feature of this class of materials consists in the possibility of controlling their properties by varying the layer thickness and the number of layers.

This review has been written within the framework of the Scientific and Engineering Programmes of the Ministry of Education and Science of Ukraine (Project No. 946) in collaboration with Institut P', University of Poitiers Chasseneuil- Futuroscope, France), National Institute for Material Science (Tsukuba, Japan), and the Complex State Budget Programmes 'Development of Foundations of Formation of Ultrahard Nanostructural Multicomponent Coatings with High Physicomechanical Properties' (Project No. 01124001382) and 'Physical Principles of Plasma Technology for Complex Treatment of Multicomponent Materials and Coatings' (Project No. 0113400137c).

The authors express their gratitude to Professor O V Sobolev (National Technical University Kharkiv Polytechnic Institute, Ukraine) for providing printed copies of articles on high-entropy alloys and nitrides based on them.

References

1. J W Yeh, Y L Chen, S J Lin, S K Chen *Mater. Sci. Forum* **560** 1 (2007)
2. Y Zhang, Y J Zhou *Mater. Sci. Forum* **561 – 565** 1337 (2007)
3. J W Yeh, S K Chen, S J Lin, J Y Gan, T S Chin, T T Shun, C H Tsai, S YChang *Adv. Eng. Mater.* **6** 299 (2004)
4. F R De Boer, in *Cohesion in Metals: Transition Metal Alloys* (Eds F R de Boer, D G Pettifor) (New York: Elsevier, 1988) p. 758
5. C J Tong, S K Chen, J W Yeh, T T Shun, C H Tsau, S J Lin, S Y Chang *Metall. Mater. Trans. A* **36** 881 (2005)
6. R Hauert, J Patscheider *Adv. Eng. Mater.* **2** 247 (2000)
7. S PalDey, S C Deevi *Mater. Sci. Eng., A* **342** 58 (2003)
8. S Zhang, D Sun, Y Q Fu, H J Du *Surf. Coat. Technol.* **167** 113 (2003)
9. *Nanostructured Coatings* (Eds A Cavaleiro, J T M de Hosson) (New York: Springer, 2006)
10. O V Sobol, A D Pogrebnjak, V M Beresnev *Phys. Met. Metallogr.* **112** 188 (2011) [*Fiz. Met. Metalloved.* **112** 199 (2011)]
11. A D Pogrebnjak, M M Danilenok, A A Drobyshevskaya, V M Beresnev, N K Erdybaeva, G V Kirik, S N Dub, V S Rusakov, V V Uglov, A P Shipilenko, Yu Zh Tuleushev *Russ. Phys. J.* **52** 1317 (2009) [*Izv. Vyssh. Uchebn. Zaved., Fiz.* **12** 61 (2008)]
12. A D Pogrebnjak, O V Sobol', V M Beresnev, P V Turbin, S N Dub, G V Kirik, A E Dmitrenko *Techn. Phys. Lett.* **35** 925 (2009) [*Pis'ma Zh. Techn. Fiz.* **35** 103 (2009)]
13. V Ivashchenko, S Veprek, A Pogrebnjak, B Postolnyi *Sci. Technol. Adv. Mater.* **15** 025007 (2014)
14. H O Pierson *Handbook of Refractory Carbides and Nitrides* (Noyes, NJ: Noyes Publ., 1969) p. 340
15. T Zhou, P Nie, X Cai, P K Chu *Vacuum* **83** 1057 (2009)
16. M Uchida, N Nihira, A Mitsuo, K Toyoda, K Kubota, T Aizawa *Surf. Coat. Technol.* **177 – 178** 627 (2004)
17. S M Kim, B S Kim, G S Kim, S Y Lee, B Y Lee *Surf. Coat. Technol.* **202** 5521 (2008)
18. C H Lai, M H Tsai, S J Lin, J W Yeh *Surf. Coat. Technol.* **201** 6993 (2007)
19. P K Huang, J W Yeh *Thin Solid Films* **518** 180 (2009)
20. M H Tsai, C H Lai, J W Yeh, J Y Gan *J. Phys. D: Appl. Phys.* **41** 1 (2008)
21. K H Cheng, C H Lai, S J Lin, J W Yeh *Thin Solid Films* **519** 3185 (2011)
22. C H Lai, S J Lin, J W Yeh, S Y Chang *Surf. Coat. Technol.* **201** 3275 (2006)
23. S Y Chang, M K Chen, D S Chen *J. Electrochem. Soc.* **156** G37 (2009)
24. Y S Huang, L Chen, H W Lui, M H Cai, J W Yeh *Mater. Sci. Eng. A* **457** 77 (2007)
25. C C Tung, J W Yeh, T T Shun, S K Chen, Y S Huang, H C Chen *Mater. Lett.* **61** 1 (2007)
26. Y J Zhou, Y Zhang, T N Kim, G L Chen *Mater. Lett.* **62** 2673 (2008)
27. H W Chang, P K Huang, J W Yeh, A Davison, C H Tsau, C C Yang *Surf. Coat. Technol.* **202** 3360 (2008)
28. P K Huang, J W Yeh, T T Shun, S K Chen *Adv. Eng. Mater.* **6** 74 (2004)
29. C Y Hsu, J W Yeh, S K Chen, T T Shun *Metall. Mater. Trans. A* **35** 1465 (2004)
30. Y Zhang, X Yang, P K Liaw *JOM* **64** 830 (2012)
31. J W Yeh *JOM* **65** 1759 (2012)

32. J W Yeh *Ann. Chim. Sci. Mater.* **31** 633 (2006)
33. L S Zhang, G L Ma, L C Fu, J Y Tian *Adv. Mater. Res.* **631 – 632** 227 (2013)
34. Y Zhang, T T Zuo, Z Tang, M C Gao, K A Dahmen, P K Liaw, Z P Lu *Prog. Mater. Sci.* **61** 1 (2014)
35. M V Ivchenko, V G Pushin, N Wanderka *Zh. Tech. Fiz.* **84** 57 (2014) [a]
36. G A Salishchev, M A Tikhonovsky, D G Shaisultanov, N D Stepanov, A V Kuznetsov, I V Kolodiy, A S Tortika, O N Senkov *J. Alloys Compd.* **591** 11 (2014)
37. A V Kuznetsov, G A Salishchev, O N Sen'kov, N D Stepanov, D G Shaisultanov *Nauch. Vedom., Ser. Mat., Fiz.* **11** 191 (2012)
38. I V Blinkov, A O Volkhonskii, V N Anikin, M I Petrzhik, D E Derevtsova *Fiz. Khim. Obrab. Mater.* **4** 37 (2010)
39. O V Sobol', A A Andreev, V F Gorban', N A Krapivka, V A Stolbovoi, I V Serdyuk, V E Fil'chikov *Pis'ma Zh. Tech. Fiz.* **38** 41 (2012) [a]
40. A V Kuznetsov, D G Shaysultanov, N D Stepanov, G A Salishchev, O N Senkov *Mater. Sci. Eng. A* **533** 107 (2012)
41. S A Firstov, V F Gorban', N A Krapivka, E P Pechkovskii, N I Danilenko, M V Karpets *Sovr. Probl. Fiz. Materialov.* **18** 140 (2009)
42. A O Volkhonskii, I V Blinkov, A V Elyutin, O B Podstyazhonok *Metallurg* (6) 55 (2010) [b]
43. A D Pogrebnjak, V M Beresnev, D A Kolesnikov, M V Kaverin, A P Shypylenko, K Oyoshi, Y Takeda, R Krause-Rehberg, A G Ponomarev *Techn. Phys. Lett.* **39** 280 (2013)
44. A D Pogrebnjak *J. Nanomater.* **2013** 1 (2013)
45. M A Laktionova, E D Tabachnikova, Z Tang, P K Liau *Fiz. Nizk. Temp.* **39** 814 (2013) [c]
46. O N Senkov, J M Scott, S V Senkova, F Meisenkothen, D B Miracle, C F Woodward *J. Mater. Sci.* **47** 4062 (2012)
47. O N Senkov, S V Senkova, D B Miracle, C Woodward *Mater. Sci. Eng. A* **565** 51 (2013)
48. Y Zhang, Y J Zhou, J P Lin, G L Chen, P K Liaw *Adv. Eng. Mater.* **6** 534 (2008)
49. Y F Kao, S K Chen, T J Chen *J. Alloys Compd.* **509** 1607 (2011)
50. J W Yeh, S Y Chang, Y D Hong, S K Chen, S J Lin *Mater. Chem. Phys.* **103** 41 (2007)
51. K Y Tsai, M H Tsai, J W Yeh *Acta Mater.* **61** 4887 (2013)
52. A D Pogrebnjak, I V Yakushchenko, A A Bagdasaryan, O V Bondar, R Krause-Rehberg, G Abadias, P Chartier, K Oyoshi, Y Takeda, V M Beresnev, O V Sobol *Mater. Chem. Phys.* **147** 1079 (2014)
53. W H Liu, Y Wu, J Y He, T G Nieh, Z P Lu *Scr. Mater.* **68** 526 (2013)
54. C Y Hsu, C C Juan, W R Wang, T S Sheu, J W Yeh, S K Chen *Mater. Sci. Eng. A* **528** 3581 (2011)
55. O N Senkov, G B Wilks, J M Scott, D B Miracle *Intermetallics* **19** 698 (2011)
56. T T Shun, C H Hung, C F Lee *J. Alloys Compd.* **493** 105 (2010)
57. M H Tsai, H Yuan, G Cheng, W Xu, K Y Tsai, C W Tsai, W W Jian, C C Juan, W J Shen, M H Chuang, J W Yeh, Y T Zhu *Intermetallics* **32** 329 (2013)
58. S Singh, N Wanderka, B S Murty, U Glatzel, J Banhart *Acta Mater.* **59** 182 (2011)
59. Z Tang, M C Gao, H Diao, T F Yang, J P Liu, T T Zuo, Y Shang, Z P Lu, Y Q Cheng, Y W Zhang, K A Dahmen, P K Liaw, T Egami *JOM* **65** 1848 (2013)
60. Y Zhang, T T Zuo, Y Q Cheng, P K Liaw *Sci. Rep.* **3** 1455 (2013)
61. S Singh, N Wanderka, K Kiefer, K Siemensmeyer, J Banhart *Ultramicroscopy* **111** 619 (2011)
62. Y Y Chen, T Duval, U D Hung, J W Yeh, H C Shih *Corros. Sci.* **47** 2257 (2005)
63. S-K Chen *Corrosion Resistance* (Ed. H Shih) (InTech, 2012) Ch. 6; DOI: 10.5772/33892
64. X W Qiu, Y P Zhang, L He, C G Liu *J. Alloys Compd.* **549** 195 (2013)
65. X F Wang, Y Zhang, Y Qiao, G L Chen *Intermetallics* **15** 357 (2007)
66. Z Hu, Y Zhan, G Zhang, J She, C Li *J. Mater. Des.* **31** 1599 (2010)
67. O N Senkov, G B Wilks, D B Miracle, C P Chuang, P K Liaw *Intermetallics* **18** 1758 (2010)
68. M S Lucas, G B Wilks, L Mauger, J A Munoz, O N Senkov, E Michel, J Horwath, S L Semiatin, M B Stone, D L Abernathy, E Karapetrova *Appl. Phys. Lett.* **100** 251907 (2012)
69. G Sheng, C T Liu *Prog. Nat. Sci.: Mater. Int.* **21** 433 (2011)
70. S Praveen, B S Murty, R S Kottada *Mater. Sci. Eng. A* **534** 83 (2012)
71. Y P Wang, B S Li, H Z Fu *Adv. Eng. Mater.* **11** 641 (2008)
72. K G Pradeep, N Wanderka, P Choi, J Banhart, B S Murty, D Raabe *Acta Mater.* **61** 4696 (2013)
73. F Otto, Y Yang, H Bei, E P George *Acta Mater.* **61** 2628 (2013)
74. B Cantor, I T H Chang, P Knight, A J B Vincent *Mater. Sci. Eng. A* **375 – 377** 213 (2004)
75. A K Singh, A Subramaniam *J. Alloys Compd.* **587** 113 (2014)
76. J Y Yang, Y J Zhou, Y Zhang *Chin. Mater. Sci. Techn. Equip.* **5** 61 (2007)
77. X Yang, Y Zhang *Mater. Chem. Phys.* **132** 233 (2012)
78. Y Zhang *Mater. Sci. Forum* **654 – 656** 1058 (2010)
79. S Guo, C Ng, J Lu, C T Liu *J. Appl. Phys.* **109** 103505 (2011)
80. Y L Chen, C W Tsai, C C Juan, M H Chuang, J W Yeh, T S Chin, S K Chen *J. Alloys Compd.* **506** 210 (2010)
81. R Raghavan, K C Hari Kumar, B S Murty *J. Alloys Compd.* **544** 152 (2012)
82. P Jinhong, P Ye *Rare Met. Mater. Eng.* **42** 232 (2013)
83. S Guo, Q Hu, C Ng, C T Liu *Intermetallics* **41** 96 (2013)
84. L Xie, P Brault, A L Thomann, J M Bauchire *Appl. Surf. Sci., B* **285** 810 (2013)
85. F Zhang, C Zhang, S L Chen, J Zhu, W S Cao, U R Kattner *Calphad* **45** 1 (2014)
86. C Zhang, F Zhang, S Chen, W Cao *JOM* **64** 839 (2012)
87. G Y Ke, S K Chen, T Hsu, J W Yeh *Ann. Chim. Sci. Mater.* **31** 669 (2006)
88. Y P Wang, B S Li, M X Ren, C Yang, H Z Fu *Mater. Sci. Eng. A* **491** 154 (2008)
89. H P Chou, Y S Chang, S K Chen, J W Yeh *Mater. Sci. Eng. B* **163** 184 (2009)
90. A Durga, K C Hari Kumar, B S Murty *Trans. Indian Inst. Met.* **65** 375 (2012)
91. M Widom, W P Huhn, S Maiti, W Steurer *Metall. Mater. Trans. A* **45** 196 (2014)
92. S W Kao, J W Yeh, T S Chin *J. Phys.: Condens. Matter.* **20** 145214 (2008)
93. Z S Nong, J C Zhu, H L Yu, Z H Lai *Trans. Nonferrous Met. Soc. China* **22** 1437 (2012)
94. M F del Grosso, G Bozzolo, H O Mosca *Physica B* **407** 3285 (2012)
95. M C Gao, D E Alman *Entropy* **15** 4504 (2013)
96. C Li, J C Li, M Zhao, Q Jiang *J. Alloys Compd.* **475** 752 (2009)

97. M H Chuang, M H Tsai, W R Wang, S J Lin, J W Yeh *Acta Mater*. **59** 6308 (2011)
98. X W Qiu *J. Alloys Compd*. **555** 246 (2013)
99. N H Tariq, M Naeem, B A Hasan, J I Akhter, M Siddique *J. Alloys Compd*. **556** 79 (2013)
100. C W Tsai, Y L Chen, M H Tsai, J W Yeh, T T Shun, S K Chen *J. Alloys Compd*. **486** 427 (2009)
101. C M Lin, H L Tsai *Intermetallics* **19** 288 (2011)
102. A Munitz, M J Kaufman, J P Chandler, H Kalaantari, R Abbaschian *Mater. Sci. Eng. A* **560** 633 (2013)
103. Y F Kao, T J Chen, S K Chen, J W Yeh *J. Alloys Compd*. **488** 57 (2009)
104. C M Liu, H M Wang, S Q Zhang, H B Tang, A L Zhang *J. Alloys Compd*. **583** 162 (2014)
105. Y L Chen, Y H Hu, C W Tsai, C A Hsieh, S W Kao, J W Yeh, T S Chin, S K Chen *J. Alloys Compd*. **477** 696 (2009)
106. K B Zhang, Z Y Fu, J Y Zhang, W M Wang, S W Lee, K Niihara *J. Alloys Compd*. **495** 33 (2010)
107. Y L Chen, Y H Hu, C A Hsieh, J W Yeh, S K Chen *J. Alloys Compd*. **481** 768 (2009)
108. Z Fu, W Chen, H Xiao, L Zhou, D Zhu, S Yang *Mater. Des*. **44** 535 (2013)
109. S Varalakshmi, G Appa Rao, M Kamaraj, B S Murty *J. Mater. Sci*. **45** 5158 (2010)
110. S Fang, W Chen, Z Fu *Mater. Des*. **54** 973 (2014)
111. C D Gumez-Esparza, R A Ochoa-Gamboa, I Estrada-Guel, J G Cabanas-Moreno, J I Barajas-Villarruel, A Arizmendi-Morquecho, J M Herrera-Ramnrez, R Martínez-Sínchez *J. Alloys Compd*. **509S** S279 (2011)
112. Y L Chen, Y H Hu, C W Tsai, J W Yeh, S K Chen, S Y Chang *Mater. Chem. Phys*. **118** 354 (2009)
113. S Varalakshmi, M Kamaraj, B S Murty *J. Alloys Compd*. **460** 253 (2008)
114. X W Qiu, Y P Zhang, C G Liu *J. Alloys Compd*. **585** 282 (2014)
115. X W Qiu, C G Liu *J. Alloys Compd*. **553** 216 (2013)
116. T M Yue, H Xie, X Lin, H O Yang, G H Meng *J. Alloys Compd*. **587** 588 (2014)
117. B A Welk, R E A Williams, G B Viswanathan, M A Gibson, P K Liaw, H L Fraser *Ultramicroscopy* **134** 193 (2013)
118. I Kunce, M Polanski, J Bystrzycki *J. Hydrogen. Energy* **38** 12180 (2013)
119. L M Wang, C C Chen, J W Yeh, S T Ke *Mater. Chem. Phys*. **126** 880 (2011)
120. H H Yang, W T Tsai, J C Kuo, C C Yang *J. Alloys Compd*. **509** 8176 (2011)
121. Y J Zhou, Y Zhang, Y L Wang, G L Chen *Mater. Sci. Eng. A* **454** – **455** 260 (2007)
122. M R Chen, S J Lin, J W Yeh, S K Chen, Y S Huang, C P Tu *Mater. Trans*. **47** 1395 (2006)
123. L Liu, J B Zhu, C Zhang, J C Li, Q Jiang *Mater. Sci. Eng. A* **548** 64 (2012)
124. S G Ma, S F Zhang, M C Gao, P K Liaw, Y Zhang *JOM* **65** 1751 (2013)
125. Y Zhang, S G Ma, J W Qiao *Metal. Mater. Trans*. **43** 2625 (2012)
126. V Braic, A Vladescu, M Balaceanu, C R Luculescu, M Braic *Surf. Coat. Technol*. **211** 117 (2011)
127. V Braic, M Balaceanu, M Braic, A Vladescu, S Panseri, A Russo *J. Mechan. Behav. Biomed. Mater*. **10** 197 (2012)
128. P K Huang, J W Yeh *Surf. Coat. Technol*. **203** 1891 (2009)
129. T K Chen, M S Wong, T T Shun, J W Yeh *Surf. Coat. Technol*. **200** 1361 (2005)
130. H W Chang, P K Huang, A Davison, J W Yeh, C H Tsau, C C Yang *Thin Solid Films* **516** 6402 (2008)
131. S Y Chang, D S Chen *Mater. Chem. Phys*. **125** 5 (2011)
132. S C Liang, Z C Chang , D C Tsai, Y C Lin, H S Sung, M J Deng, F S Shieu *Appl. Surf. Sci*. **257** 7709 (2011)
133. B Ren, Z X Liu, L Shi, B Cai, M X Wang *Appl. Surf. Sci*. **257** 7172 (2011)
134. C H Lin, J G Duh, J W Yeh *Surf. Coat. Technol*. **201** 6304 (2007)
135. D C Tsai, Z C Chang, B H Kuo, M H Shiao, S Y Chang, F S Shieu, *Appl. Surf. Sci*. **282** 789 (2013)
136. S Y Chang, D S Chen *Appl. Phys. Lett*. **94** 231909 (2009)
137. S Y Chang, M K Chen *Thin Solid Films* **517** 4961 (2009)
138. S Y Chang, S Y Lin, Y C Huang, C L Wu *Surf. Coat. Technol*. **204** 3307 (2010)
139. S Y Chang, S Y Lin, Y C Huang *Thin Solid Films* **519** 4865 (2011)
140. K H Cheng, C H Weng, C H Lai, S J Lin *Thin Solid Films* **517** 4989 (2009)
141. H T Hsueh, W J Shen, M H Tsai, J W Yeh *Surf. Coat. Technol*. **206** 4106 (2012)
142. C T Lee, W H Cho, M H Shiao, C N Hsiao, K S Tang, C C Jaing *Proc. Eng*. **36** 316 (2012)
143. B Ren, Z Shen, Z Liu *J. Alloys Compd*. **560** 171 (2013)
144. Z C Chang, S C Liang, S Han *Nucl. Instrum. Methods Phys. Res., Sect. B* **269** 1973 (2011)
145. W R Wang, W L Wang, S C Wang, Y C Tsai, C H Lai, J W Yeh *Intermetallics* **26** 44 (2012)
146. H Zhang, Y He, Y Pan *Scr. Mater*. **69** 342 (2013)
147. A Gali, E P George *Intermetallics* **39** 74 (2013)
148. C Ng, S Guo, J Luan, Q Wang, J Lu, S Shi, C T Liu *J. Alloys Compd*. **584** 530 (2014)
149. Y J Zhou, Y Zhang, Y L Wang, G L Chen *Appl. Phys. Lett*. **90** 181904 (2007)
150. J W Qiao, S G Ma, E W Huang, C P Chuang, P K Liaw, Y Zhang *Mater. Sci. Forum* **688** 419 (2011)
151. M A Hemphill, T Yuan, G Y Wang, J W Yeh, C W Tsai, A Chuang, P K Liaw *Acta Mater*. **60** 5723 (2012)
152. W R Wang, W L Wang, J W Yeh *J. Alloys Compd*. **589** 143 (2014)
153. X Yang, Y Zhang, P K Liaw *Proc. Eng*. **36** 292 (2012)
154. M S Lucas, L Mauger, J A Musoz, Y Xiao, A O Sheets, S L Semiatin, J Horwath, Z Turgut *J. Appl. Phys*. **109** 07E307 (2011)
155. Y L Chou, J W Yeh, H C Shih *Corros. Sci*. **52** 2571 (2010)
156. H Cui, Y Wang, J Wang, X Guo, H Fu *Res. Dev*. **8** 259 (2011)
157. C P Lee, C C Chang, Y Y Chen, J W Yeh, H C Shih *Corros. Sci*. **50** 2053 (2008)
158. C P Lee, Y Y Chen, C Y Hsu, J W Yeh, H C Shih *J. Electrochem. Soc*. **154** C424 (2007)
159. O N Doran, B C Nielsen J A Hawk *Oxid. Met*. **80** 177 (2013)
160. B Ren, Z X Liu, D M Li, L Shi, B Cai, M X Wang *Mater. Corros*. **63** 828 (2012)
161. Y Y Chen, U T Hong, H C Shih, J W Yeh, T Duval *Corros. Sci*. **47** 2679 (2005)
162. C W Tsai, M H Tsai, J W Yeh, C CYang *J. Alloys Compd*. **490** 160 (2010)
163. Y X Zhuang, H D Xue, Z Y Chen, Z Y Hu, J C He *Mater. Sci. Eng. A* **572** 30 (2013)
164. K B Zhang, Z Y Fu, J Y Zhang, W M Wang, S W Lee, K Niihara *Mater. Sci. Eng*. **20** 012009 (2011)

165. C Ng, S Guo, J Luan, S Shi, C T Liu *Intermetallics* **31** 165 (2012)
166. L Jiang, Y Lu, Y Dong, T Wang, Z Cao, T Li *Intermetallics* **44** 37 (2014)
167. C M Lin, H L Tsai *Mater. Chem. Phys.* **128** 50 (2011)
168. K Zhang, Z Fu *Intermetallics* **22** 24 (2012)
169. P P Bhattacharjee, G D Sathiaraj, M Zaid, J R Gatti, C Lee, C W Tsai, J W Yeh *J. Alloys Compd.* **587** 544 (2014)
170. C Huang, Y Zhang, J Shen, R Vilar *Surf. Coat. Techol.* **206** 1389 (2011)
171. V Dolique, A-L Thomann, P Brault, Y Tessier, P Gillon *Surf. Coat. Techol.* **204** 1989 (2010)
172. T K Chen, T T Shun, J W Yeh, M S Wong *Surf. Coat. Technol.* **188** – **189** 193 (2004)
173. D C Tsai, Y L Huang, S R Lin, S C Liang, F S Shieu *Appl. Surf. Sci.* **257** 1361 (2010)
174. C H Lai, K H Cheng, S J Lin, J W Yeh *Surf. Coat. Technol.* **202** 3732 (2008)
175. D-C Tsai, Z-C Chang, B-H Kuo, T-N Lin, M-H Shiao, F-S Shieu *Surf. Coat. Techol.* **240** 160 (2014)
176. D C Tsai, Z C Chang, L Y Kuo, T J Lin, T N Lin, M H Shiao, F S Shieu *Thin Solid Films* **544** 580 (2013)
177. P K Huang, J W Yeh *Scr. Mater.* **62** 105 (2010)
178. M H Hsieh, M H Tsai, W J Shen, J W Yeh *Surf. Coat. Technol.* **221** 118 (2013)
179. T Egami, W Guo, P D Rack, T Nagase *Metall. Mater. Trans. A* **45** 180 (2014)
180. Y F Kao, S K Chen, J H Sheu, J T Lin, W E Lin, J W Yeh, S J Lin, T H Liou, C W Wang *J. Hydrogen, Energy* **35** 9046 (2010)
181. M H Tsai, C W Wang, C H Lai, J W Yeh, J Y Gan *Appl. Phys. Lett.* **92** 052109 (2008)
182. S C Liang, D C Tsai, Z C Chang, T N Lin, M H Shiao, F S Shieu *ESL* **15** H5 (2012)
183. S Y Chang, Y C Huang, C E Li, H F Hsu, J W Yeh, S J Lin *JOM* **65** 1790 (2013)
184. O N Senkov, S V Senkova, C Woodward, D B Miracle *Acta Mater.* **61** 1545 (2013)
185. B D Cullity *Elements of X-Ray Diffraction* (Ed. M Cohen) (Reading, MA: Addison-Wesley, 1978) p. 391
186. W B Pearson *A Handbook of Lattice Spacing and Structures of Metals and Alloys* (New York: Pergamon Press, 1967) p. 1446
187. K Lonsdale, N F M Henry, in *International Tables for X-Ray Crystallography* (Ed. G D Rieck) (Birmingham: Kynoch Press, 1968) p. 14
188. G Grimvall *Thermophysical Properties of Materials* (Amsterdam: Elsevier, 1999)
189. B Fultz *Prog. Mater. Sci.* **55** 247 (2010)
190. A R Miedema, P F de Chatel, F R de Boer *Physica B* **100** 1 (1980)
191. A Takeuchi, A Inoue *Mater. Sci. Eng. A* **304** – **306** 446 (2001)
192. R W Cahn, P Hassen *Physical Metallurgy* (Amsterdam: Elisevier, 1996) p. 669
193. C T Liu *Int. Met. Rev.* **29** 168 (1984)
194. J H Zhu, P K Liaw, C T Liu *Mater. Sci. Eng. A* **239** – **240** 260 (1997)
195. G A Mansoori, N F Carnahan, K E Starling, T W Leland Jr *J. Chem. Phys.* **54** 1523 (1971)
196. L Kaufman *Computer Calculation of Phase Diagrams* (New York: Academic Press, 1970) p. 334
197. N Saunders, A P Miodownik *CALPHAD: A Comprehensive Guide (Pergamon Mater. Ser.)* (Ed. R W Cahn) (Oxford: Elisevier, 1998) p. 478
198. A W Weeber, H Bakker *Physica B* **153** 93 (1988)
199. A D Pogrebnjak, V M Beresnev *Nanocoatings, Nanosystems, Nanotechnologies-Books* (New York: Bentham Sci. Publ., 2012) p. 147
200. I Petrov, L Hultman, J E Sundgen, J E Green *J. Vac. Sci. Technol., A* **10** 265 (1992)
201. W Ensinger *Surf. Coat. Technol.* **65** 90 (1994)
202. G Abadias, Y Y Tse, Ph Guérin, V Pelosin *J. Appl. Phys.* **99** 113519 (2006)
203. J Rosler, H Harders, M Baker, in *Mechanical Behavior of Engineering Materials* (Berlin, Heidelberg, New York: Springer, 2007) p. 205
204. J E Sundgen *Thin Solid Films* **128** 21 (1995)
205. A D Pogrebnjak, Yu N Tyurin *Phys.-Usp.* **48** 487 (2005)
206. I Yamada, J Matsuo, N Toyoda, A Kirkpatrick *Mater. Sci. Eng. R* **34** 231 (2001)
207. K Yamamoto, T Sato, K Takahara, K Hanaguri *Surf. Coat. Technol.* **174** – **175** 620 (2003)
208. A Leyland, A Matthews *Wear* **246** 1 (2000)
209. A D Pogrebnjak, S Bratushka, V I Boyko, I V Shamanin, Yu V Tsvintarnaya *Nucl. Instrum. Methods* **145** 373 (1998)
210. V Boiko, A N Valyaev, A D Pogrebnjak *Phys.-Usp.* **42** 1139 (1999)
211. J Zou, T Grosdidier, K Zhang, C Dong *Acta Mater.* **54** 5409 (2006)
212. A D Pogrebnjak, A D Mikhaliov, N A Pogrebnjak Jr, Yu V Tsvintarnaya, V I Lavrentiev, M Iljashenko, A N Valyaev, S Bratushka, A Zecca, R Sandrik *Phys. Lett. A* **241** 357 (1998)
213. A D Pogrebnjak, A G Ponomarev, A P Shpak, Yu A Kunitskii *Phys.-Usp.* **55** 270 (2012)
214. A D Pogrebnjak, S N Bratushka, V M Beresnev, N Levintant-Zayonts *Russ. Chem. Rev.* **82** 1135 (2013)]
215. C H Tsai, Y C Yang, C C Lee, L Y Wu, H J Huang *Proc. Eng.* **36** 246 (2012)
216. A D Pogrebnjak, V M Beresnev, O V Bondar, G Abadias, P Chartier, B A Postol'nyi, A A Andreev, O V Sobol' *Techn. Phys. Lett.* **40** 215 (2014)
217. A D Pogrebnjak, A V Pshyk,V M Beresnev, B R Zhollybekov *J. Friction Wear* **35** 55 (2014)
218. A D Pogrebnjak, V M Beresnev, D A Kolesnikov, O V Bondar, Y Takeda, K Oyoshi, M V Kaverin, O V Sobol, R Krause-Rehberg, C Karwat *Acta Phys. Pol., A* **123** 816 (2013)
219. A D Pogrebnjak, M S Prozorova, M G Kovalyova, O V Kolisnichenko,V M Beresnev, K Oyoshi, Y Takeda, A S Kaverina, A P Shypylenko, J Partyka *Acta Phys. Pol., A* **123** 813 (2013)
220. A D Pogrebnjak, A S Kaverina, M K Kylyshkanov *Prot. Met. Phys. Chem. Surf.* **50** 72 (2014)
221. A D Pogrebnjak, G Abadias, O V Bondar *Acta Phys. Pol., A* **125** 1284 (2014)
222. A D Pogrebnjak, G Abadias, P Chartier *Acta Phys. Pol., A* **125** 1296 (2014)
223. M H Tsai, J W Yen *Mater. Res. Lett.* http://dx.doi.org/10.1080/21663831.2014.912690 1-17 (2014)
224. A D Pogrebnjak, V N Borisyuk, A A Bagdasaryan *Condens. Matter. Phys.* **16** Art. No. 33803 (2013)
225. T N Koltunowisz, P Zhukowski, A K Fedorov, A V Larkin, A Patryn, B Andryevskyy, A Saad, J A Fedotova, V V Fedotova *Electron. Elecrotechn.* **9** 37 (2013)
226. I A Lyashenko, A V Khomenko, L S Metlov *Techn. Phys.* **55** 1193 (2010)

227. A D Pogrebnjak, Yu A Kravchenko, S B Kislitsyn, S M Ruzimov, F Noli, P Misaelides, A Hatzidimitriou *Surf. Coat. Technol.* **201** 2621 (2006)
228. S P Zhkowski, C Karwat, F F Komarov *Phys. Status Solidi Appl. Res.* **157** 373 (1996)
229. A V Khomenko, N V Prodanov *Condens. Matter Phys.* **11** 615 (2008)

[a] — *Tech. Phys. (Engl. Transl.)*
[b] — *Metallurgist (Engl. Transl.)*
[c] — *Low Temp. Phys. (Engl. Transl.)*